Three-Dimensional Rankine Panel Simulation of Lifting Flows Under a Free Surface

by

Christopher J. Emerson

BA in American Literature
Middlebury College, May 1992

Submitted to the Department of Ocean Engineering in Partial Fulfillment of the requirements for the degree of

Master of Science in Ocean Engineering

at the

MASSACHUSETTS INSTITUTE OF TECHNOLOGY

FEBRUARY 2001

Author.....
Department of Ocean Engineering
February 8, 2001

Certified by.....
Paul D. Sclavounos
Professor of Naval Architecture
Thesis Supervisor

Accepted by.....
Nicholas Patrikalakis
Kawasaki Professor of Engineering
Chairman, Departmental
Committee on Graduate Students

Three-Dimensional Rankine Panel Simulation of Lifting Flows Under a Free Surface

by

Christopher J. Emerson

Submitted to the Department of Ocean Engineering on February 8, 2001 in partial fulfillment of the requirements for the degree of

Master of Science in Ocean Engineering

ABSTRACT

A study was done of the applicability of the SWAN Rankine panel based potential flow solver to fully submerged lifting and non-lifting surfaces. Validation was performed on simple forms such as a sphere and spheroid, as well as cambered and uncambered foils. Following successful validation, simulation was attempted of a composite form utilizing a collection of the aforementioned bodies.

The results of the simulation closely matched potential flow theory in all of the simple cases. The composite form also produced qualitatively accurate results, showing that SWAN is indeed a viable tool for the evaluation of these types of bodies.

Thesis Supervisor: Paul Sclavounos
Title: Professor of Naval Architecture

INTRODUCTION

The introduction of modern computing technology to the field of naval architecture has brought with it a range of new tools used to analyze the hydrodynamic effects on a translating body in contact with a fluid medium. Chief among these are panel methods. Here, the body and free surface are broken up into smaller subdomains over which an approximation to the solution of the governing equations can then be produced. With increasing panel density over the surface in question comes a commensurate increase in the solution accuracy. The challenge to the panel method user then is to show this convergence and show that the converged solution agrees with theory. Once this has been done for simple forms, confidence can be gained in the method used, and more complex geometries can then be examined.

That is the purpose of this study. The three-dimensional Rankine panel method analysis routine SWAN will be tested for accuracy. While SWAN has been thoroughly validated on a number of surface piercing bodies, to date there has been little to no work done with SWAN on fully submerged, lifting surfaces. This study will undertake that work, validating SWAN on a range of simple objects including a sphere, a spheroid, a symmetric foil, and an asymmetric, cambered foil. Following this, composite forms will be constructed of these previously studied base forms. The final goal is to produce meaningful results from a complex form which approximates a typical IACC keel. As such, it incorporates a skeg foil, and a spheroidal bulb.

PANEL METHODS, A SIMPLIFIED INTRODUCTION

The primary assertion of panel methods is that "the velocity potential of any irrotational flow can be represented as a distribution of sources and doublets over its bounding surfaces"[6]. The trail towards proof of this begins with the divergence theorem, which states that for any vector $\vec{U}$ with finite derivatives over an arbitrary volume V with surfaces S and outward directed normal $\vec{n}$,

$$\int_V \nabla \cdot \vec{U} dV = -\int_S \vec{n} \cdot \vec{U} dS . \qquad (1)$$

The geometry of the situation in question is pictured below

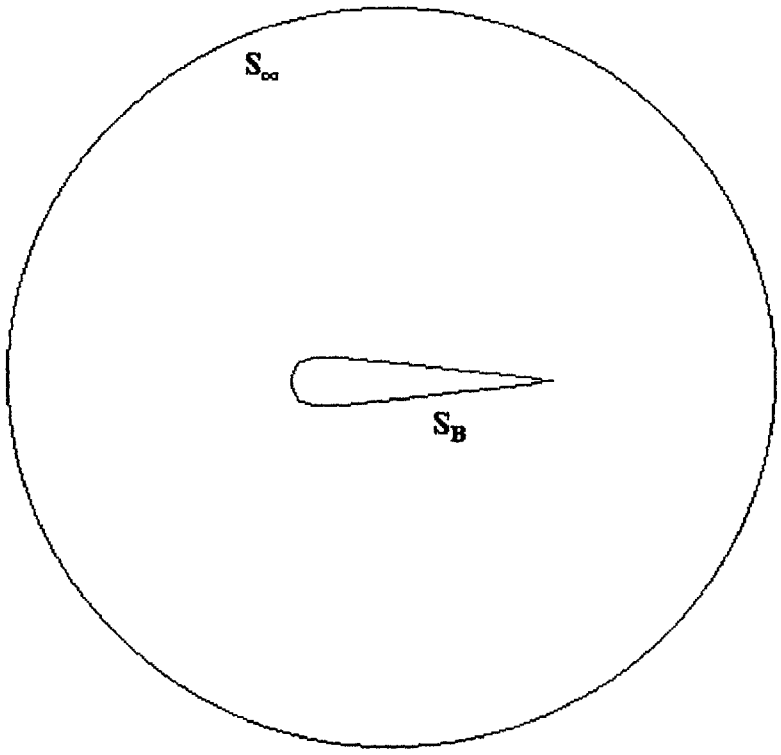

Figure 1

We will take as our vector $\vec{U}$,

$$\vec{U} = \phi \nabla \phi_s - \phi_s \nabla \phi \qquad (2)$$

where ϕ is the velocity potential in the volume V and ϕ_s is the velocity potential of a unit source located at point P within the volume. Note now that in order for $\vec{U}$ to have finite derivatives, we are required to construct our volume V in a certain manner. First, we note that the derivatives of ϕ_s and therefore those of $\vec{U}$ blow up at P, so we construct a small circle of radius ε around our source. Secondly, we know that the vortex sheet trailing our body must have a potential jump across it in order to develop lift and so we have to insert a cut in the volume at the wake in order to keep $\vec{U}$ continuous. So, our final geometry is as below.

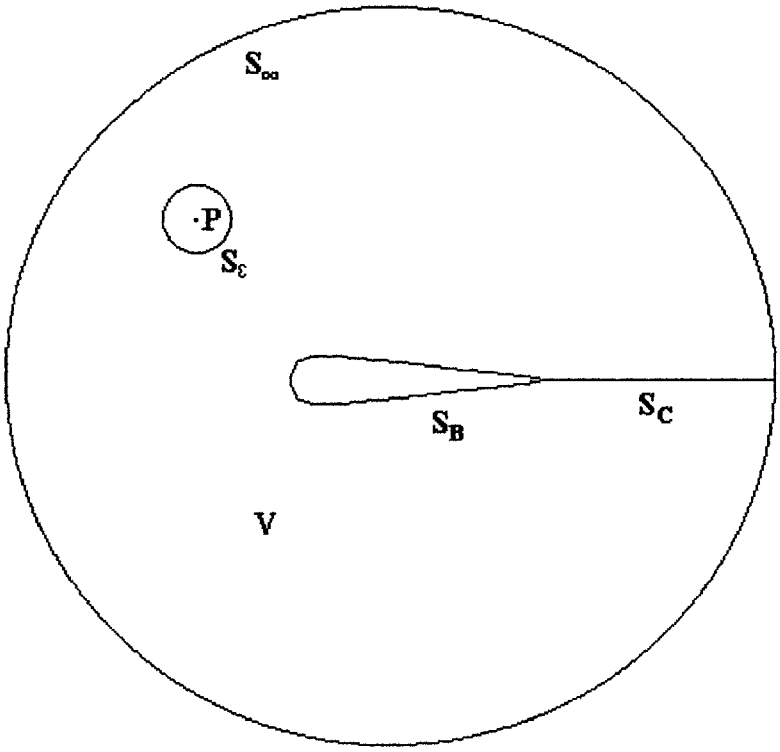

Figure 2

Now, substituting (2) into the left-hand side of (1) and carrying out the divergence we see

$$\iint \nabla \cdot \vec{U} dV = \iint \nabla \cdot (\phi \nabla \phi_S - \phi_S \nabla \phi) dV$$

$$= \iint \nabla \phi \cdot \nabla \phi_S + \phi \nabla \cdot \nabla \phi_S - \nabla \phi_S \cdot \nabla \phi - \phi_S \nabla \cdot \nabla dV \phi$$

$$= \int_V \phi \nabla^2 \phi_S - \phi_S \nabla^2 \phi dV$$

$$= 0 \text{ in Volume } V$$

due to the fact that for any potential function ϕ,

$$\nabla^2 \phi = 0 .$$

Substituting this result into the left-hand side of (1) and then substituting (2) into the right-hand side of (1) we get

$$- \int_{S+S\varepsilon} \vec{n} \cdot (\phi \nabla \phi_S - \phi_S \nabla \phi) dS = 0 . \qquad (3)$$

If we then separate this integral into its tow surfaces, (3) becomes

$$- \int_S \vec{n} \cdot (\phi \nabla \phi_S - \phi_S \nabla \phi) dS = \int_{S\varepsilon} \vec{n} \cdot (\phi \nabla \phi_S - \phi_S \nabla \phi) dS \qquad (4)$$

If we then let the radius of the circle around the point P go to zero, the right-hand side of (4) becomes

$$\int_{S\varepsilon} \vec{n} \cdot (\phi \nabla \phi_S - \phi_S \nabla \phi) dS \approx \phi_P \int_{S\varepsilon} \vec{n} \nabla \phi_S dS - V_P \cdot \int_{S\varepsilon} \vec{n} \phi_S dS \qquad (5)$$

where ϕ_P and V_P are the limiting values of ϕ and $\nabla \phi$ respectively. Now all we need to do is note that the first integral on the right-hand side of (5) is simply the flux through surface S_ε which we know from our problem definition to be 1. In addition, we note that ϕ_s is constant over the surface S_ε and therefore can be moved outside of the integral, leaving the integral of the normal vector over the surface which we know by symmetry to be zero. So, finally, we substitute these results into equation (4) to get

$$- \int_S \vec{n} \cdot (\phi \nabla \phi_S - \phi_S \nabla \phi) dS = \phi_P \qquad (6)$$

known as Green's Identity. This equation can now give us the value of ϕ at any point P within our domain based only on the values of the potential functions calculated at the boundaries.

Taking the two halves of the integral in (6) separately, we will look at the left side first,

$$\int_S (\vec{n} \cdot \nabla \phi) \phi_S dS . \qquad (7)$$

While ϕ_s was previously defined as the potential of a unit source at P evaluated on S, it could alternately be interpreted as a unit source at dS evaluated at P. From this perspective, (7) becomes the potential of a source distribution on S with strength per unit length of $\vec{n} \cdot \nabla \phi$.

Looking at the second half of the integral in (6) we see

$$\int_S \phi \vec{n} \cdot \nabla \phi_S dS .$$

First, we consider $\vec{n} \cdot \nabla \phi_S$ to be the rate of change of the potential function ϕ_s in a direction normal to the surface at dS. Moran represents this as follows:

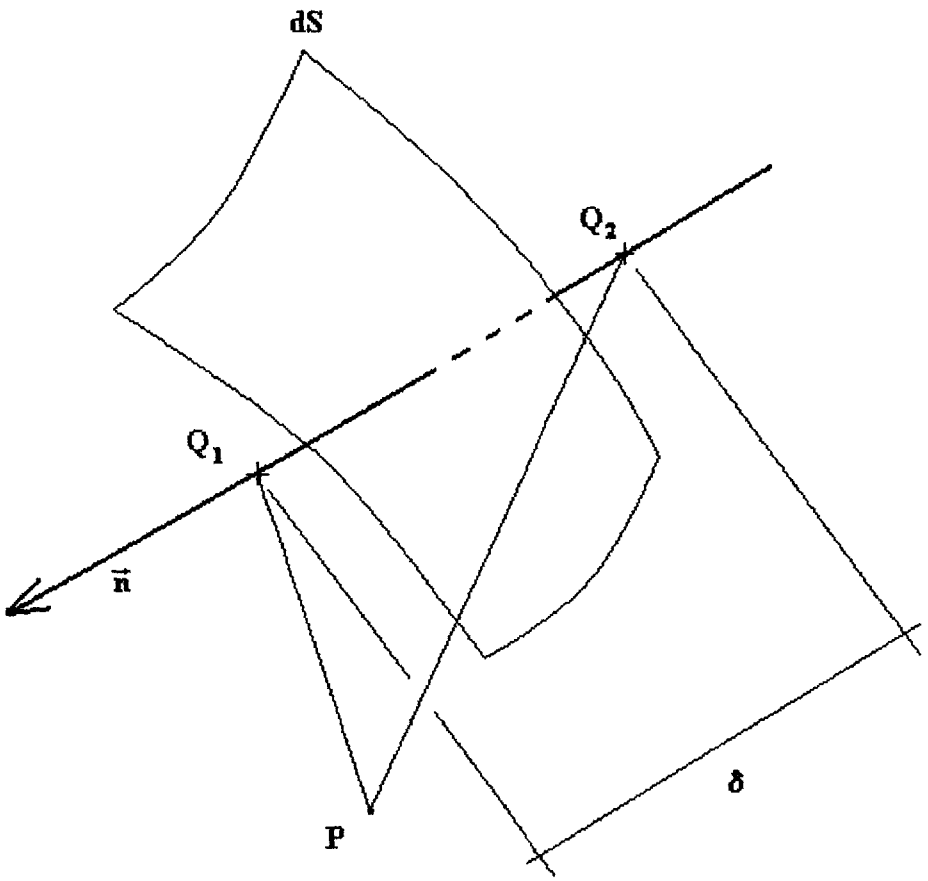

Figure 3

Letting Q_1 and Q_2 be points on either side of the surface, and distance δ apart, Then letting ϕ_1 and ϕ_2 be the potential at points Q_1 and Q_2 respectively due to a unit source at P, we see

$$\vec{n} \cdot \nabla \phi_S = \lim_{\delta \to 0} \frac{\phi_1 - \phi_2}{\delta}$$

Reversing the sense of the potentials again, and now saying ϕ_1 and ϕ_2 are the potential at P due to two sources of strength $1/\delta$ at Q_1 and Q_2, we can now see that as δ goes to zero, we are left with a dipole.

Thus, we have shown what Moran predicted, that we can indeed represent the velocity potential of an irrotational flow using sources and dipoles distributed over the volume boundaries.

From this point, the jump to pressure and forces is quite simple. With a known potential function ϕ, we can express the hydrodynamic pressure using the Bernoulli equation,

$$P = -\rho(\frac{d}{dt}\phi + \frac{1}{2}\nabla\phi \cdot \nabla\phi).$$

Finally, in order to get forces and moments, we merely integrate pressure as follows

$$F_i = \int_S P\vec{n}_i dS \qquad \text{for } i = 1,2,3$$

and

$$M_i = \int_S P\left(\vec{x} \times \vec{n}_i\right) dS \qquad \text{for } i = 1,2,3$$

This completes our greatly simplified discussion on the background theory of panel methods. It only remains to be said that while SWAN does indeed employ the broad strokes described above, the details that make SWAN a successful and accurate program are highly complex and beyond the scope of the current study.

VALIDATION:

Having gained a basic understanding of the theory behind panel methods, our next step is to test SWAN's performance on several known bodies. Towards this end, the motion of a series of submerged bodies with known hydrodynamic characteristics was simulated in order to ascertain the level of accuracy of the resulting output. Among these were a sphere, a spheroid, a symmetric foil, and an asymmetric, cambered foil.

SPHERE:

The problem of a sphere undergoing steady translation through an infinite ideal fluid is an excellent one for the validation of a potential flow program such as SWAN. The reason for this is that there exists a known, closed-form analytical solution and that solution is simply

$$\vec{F} = \vec{M} = 0 .$$

Further, calculation of the added mass can also be used to validate unsteady motion simulation by comparing it to the theoretical value,

$$M_a = \frac{1}{2}\rho\nabla = \frac{2}{3}\rho\pi a^3 ,$$

where a is the sphere radius and ρ is the water density.

PROOF:

To illustrate the zero force and moment solution, we will take a sphere of radius **a** centered on the x-axis and moving forward with velocity U in the x-direction as illustrated below.

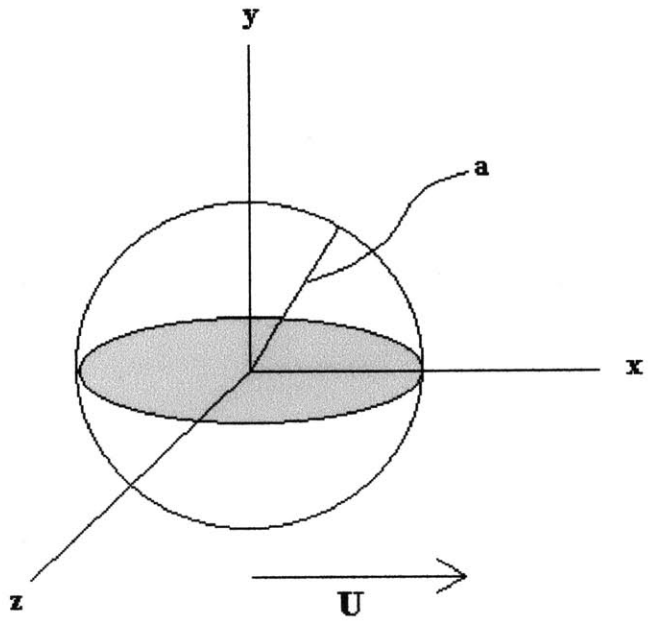

Figure 4

By inspection, we know that the boundary condition on the body is

$$\frac{\partial \phi}{\partial r} = U\cos(\theta) \qquad (8)$$

which states that there is no flux through the surface of the sphere. We can also assume that the effects of the body motion go to zero as the distance from the sphere increases to infinity.

$$\lim_{r\to\infty}(\phi) = 0 \qquad (9)$$

Finally, as always with incompressible potential flow problems, we have the Laplace equation,

$$\nabla^2\phi = 0 \qquad (10)$$

which states that mass is conserved.

Using these boundary conditions, we are able to solve (10) and arrive at the potential function

$$\phi = -\left(\frac{1}{2}U\frac{a^3}{r^2}\right)\cos(\theta), \qquad (11)$$

which describes the flow in question.

Next, having determined the potential function, we follow the derivation of Newman(1977) to determine the total force and moment on the sphere. Initially, we integrate the effects of hydrodynamic pressure over the entire surface.

$$\vec{F} = \iint_S pndS \qquad \vec{M} = \iint_S p(r \times n)dS \qquad (12,13)$$

where ***p*** represents the dynamic pressure. Substituting Bernoulli's equation for dynamic pressure into (12) and (13) above, we arrive at

$$\vec{F} = \iint_S \left(\frac{\partial \phi}{\partial t} + \frac{1}{2}\nabla\phi \cdot \nabla\phi\right) ndS, \qquad (14) \quad \text{and}$$

$$\vec{M} = \iint_S \left(\frac{\partial \phi}{\partial t} + \frac{1}{2}\nabla\phi \cdot \nabla\phi\right)(r \times n)dS. \quad (15)$$

Using Gauss,

$$\iiint_V \nabla x dV = \iint_S xndS$$

and the transport theorem,

$$\frac{dI}{dt} = \iiint_V \frac{\partial f}{\partial t}dV + \iint_S fU_n dS \qquad \text{where} \qquad U_n = U \cdot n$$

we can derive

$$\vec{F} = -\rho\frac{d}{dt}\iint_S \phi n dS - \rho \iint_{S\infty} \left[\frac{\partial \phi}{\partial n}\nabla\phi - n\frac{1}{2}\nabla\phi \cdot \nabla\phi\right] dS$$

and

$$\vec{M} = -\rho \frac{d}{dt} \iint_S \phi (r \times n) dS - \rho \iint_{S\infty} r \times \left[\frac{\partial \phi}{\partial n} \nabla \phi - \frac{1}{2} \nabla \phi \cdot \nabla \phi n \right] dS$$

where S_∞ denotes an imaginary control surface at infinity.

However, observing boundary condition (9) we can see that in both the force and moment equations the integral over the imaginary control surface S_∞ go to zero due to its infinite distance from the sphere.

This leaves

$$\vec{F} = -\rho \frac{d}{dt} \iint_S \phi n dS \qquad (16)$$

$$\vec{M} = -\rho \frac{d}{dt} \iint_S (r \times n) \phi dS$$

Now, we are able to invoke the steady nature of our problem to note first that

$$\vec{F} = 0$$

which is D'Alembert's paradox, stating that there are no resultant forces on any body undergoing steady translation through an infinite ideal fluid.

Secondly, contrary to intuition, it is still possible for a moment to exist under these steady translation conditions (the Munk moment, for example). In the special case of the sphere however, where the directions of the ***r*** and ***n*** vectors are identical, and therefore,

$$\vec{r} = c \vec{n}$$

where c is some scalar quantity, we see

$$\vec{r} \times \vec{n} = 0$$

and as a result,

$$\vec{M} = 0$$

as well, without even invoking the steady nature of the motion.

To conclude, a sphere undergoing steady translation in an infinite ideal fluid experiences no forces or moments.

SWAN RESULTS:

For the SWAN simulation of a sphere undergoing steady translation, a radius of 0.2 meters was used. The center point of the sphere was submerged a distance of 2 meters below the free surface to nearly eliminate free surface effects and more closely approximate an infinite medium.

Several panelization schemes were investigated. All involve lines of latitude parallel with the y-z plane, utilizing a cosine panel distribution from the forward end (x=0.2) to the aft end (x=-0.2). This concentrates panels fore and aft in an effort to increase panel density in areas of greater pressure gradients as well as maintains reasonably shaped panels.

In addition, lines of longitude were used that radiated out from the x-axis. In all cases, an equal number of latitude and longitude lines were used in order to produce nearly square panels. The sphere was divided into two panel sheets meeting at the x-y plane. A typical geometry, employing 30 panels in each dimension is shown in Figure 5 below. Simulations were done using 10, 15, 20, 25, and 30 panels in each dimension to test for convergence.

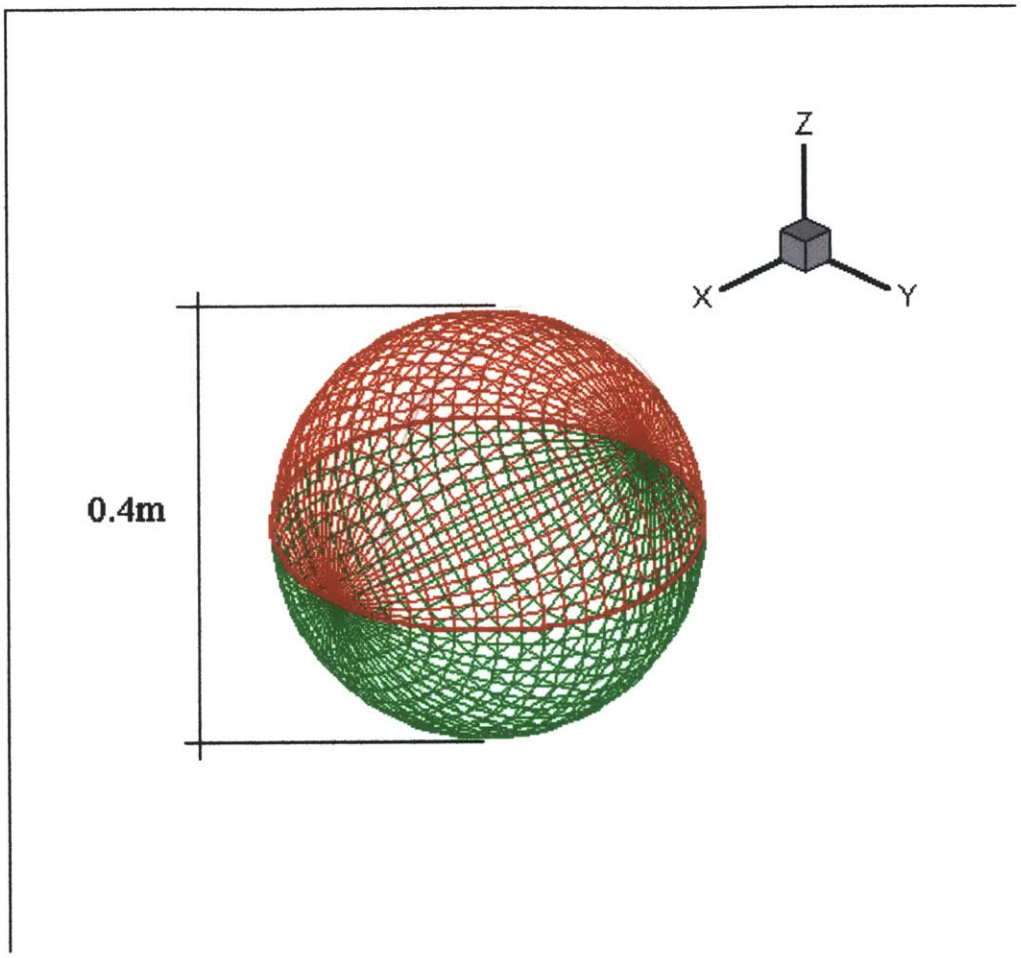

Figure 5

FORCES and MOMENTS:

For the force and moment investigation, the sphere velocity was set at 0.5 m/s in the x-direction which results in a Froude number of

$$Fr = \frac{U}{\sqrt{gL}} = 0.25$$

which is well within the demonstrated capabilities of SWAN.

The following chart and plot summarize the results.

Panels	Fx	Fy	Fz	Mx	My	Mz
10	-3.73E-05	2.92E-06	-3.88E-05	1.90E-07	6.00E-07	-1.34E-08
15	-4.17E-05	-4.88E-06	-3.53E-05	-1.34E-06	1.00E-07	-5.37E-09
20	-3.91E-05	2.69E-06	-3.41E-05	1.73E-06	3.00E-07	-8.59E-10

25	-4.20E-05	1.20E-05	-1.65E-05	-1.20E-06	-4.00E-07	-1.11E-09
30	-5.25E-05	-3.38E-06	1.15E-05	2.00E-08	-3.65E-07	-1.67E-09

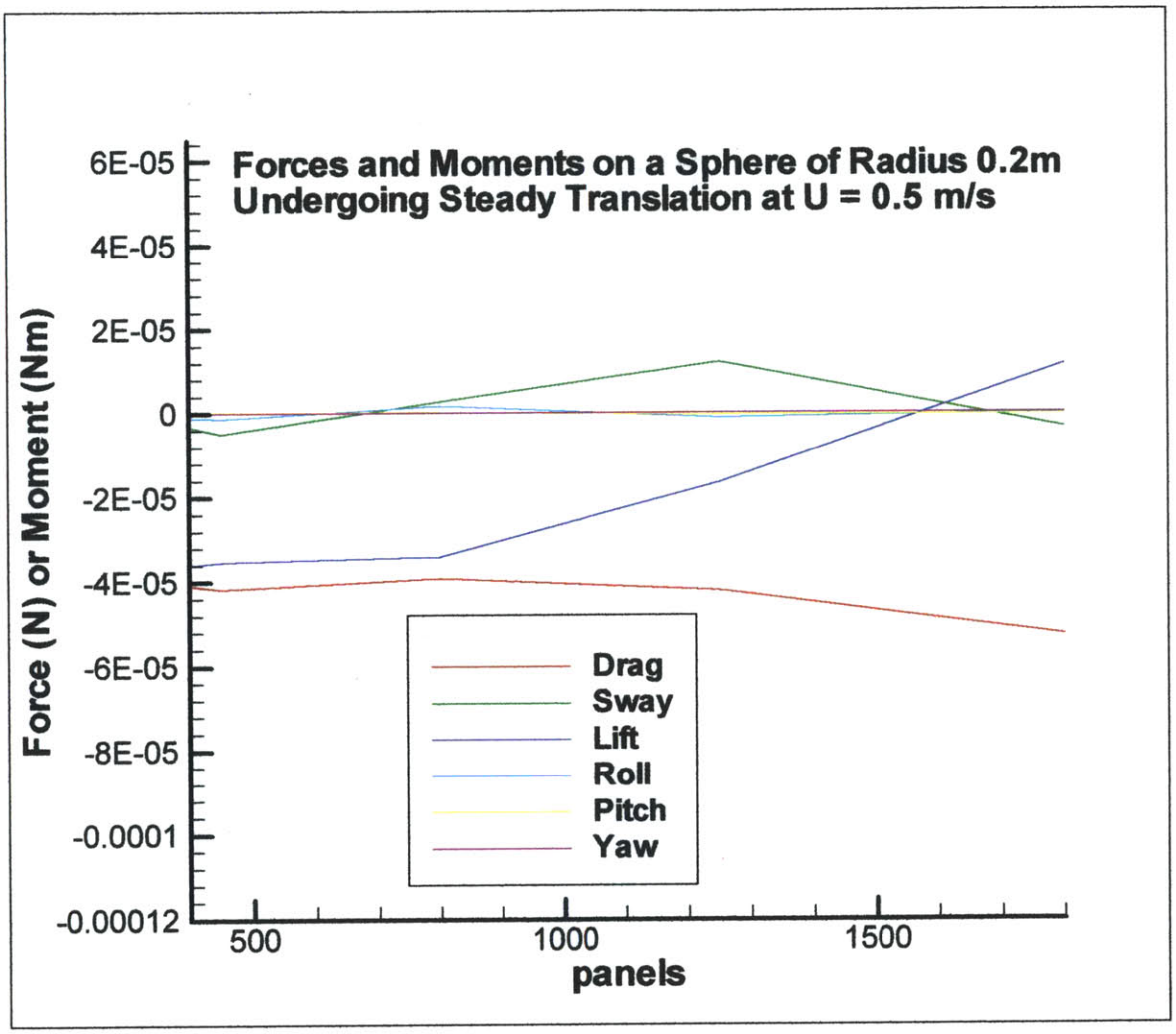

Figure 6

If we take as a reference force the stagnation pressure multiplied by the frontal area of the sphere, we get

$$F_{ref} = \frac{1}{2}\rho U^2(\pi a^2) = 16.1N \qquad (17)$$

An examination of the data reveals that while there is no clear trend towards the expected zero values, it should be noted that the forces produced are inconsequential when compared to the reference force calculated above in (17). Taking the maximum force

magnitude, the drag force at 30 panels, we see that the SWAN calculated forces are a factor of 10^{-6} less than the reference force F_{ref} and can therefore be disregarded.

The same calculation can be done for the SWAN calculated moments. If we take as our reference moment

$$M_{ref} = F_{ref} \times radius = \frac{1}{2}\rho U^2(\pi a^3) = 3.22Nm \qquad (18)$$

we see that the maximum moment, the moment about the x-axis at 20 panels, is a factor of 10^{-6} less than the reference moment M_{ref} and can therefore be disregarded.

ADDED MASS:

The added mass analysis for the sphere was done by observing the force time record for a prescribed harmonic motion. Accordingly, the sphere's location as a function of time is defined as

$$x = A\sin(\omega t). \qquad (19)$$

For the current problem, an amplitude of 1m and a period of 10 seconds were used. Note that the direction of the motion was in sway, maintaining a constant distance from the surface and eliminating the possibility that variable free surface effects could effect our solution. Differentiating the position function twice we derive a function for the acceleration of the sphere,

$$a = -A\omega^2 \sin(\omega t). \qquad (20)$$

In solving for the maximum acceleration we set

$$\sin(\omega t) = -1$$

Therefore,

$$a_{max} = A\omega^2$$

Finally, we can use Newton's second law F=ma to give

$$F_{max} = M_a a_{max} = M_a A\omega^2$$

Note that SWAN outputs only the hydrodynamic forces and therefore, the D'Alembert force, or force due to the acceleration of the body mass itself can be disregarded. As a result, the SWAN output force is due only to the added mass which can then be obtained directly. Solving for the added mass gives

$$M_a = \frac{F_{\max}}{A\omega^2}$$

which, with the values given above gives

$$M_a = F_{\max}\left(\frac{25}{\pi^2}\right). \qquad (21)$$

All that remains is to get the maximum force values from SWAN, calculate the indicated added mass and compare with the theoretical predictions. The same panelization schemes were used as with the preceding force and moment analysis. Figure 7 below shows a typical force record produced by SWAN.

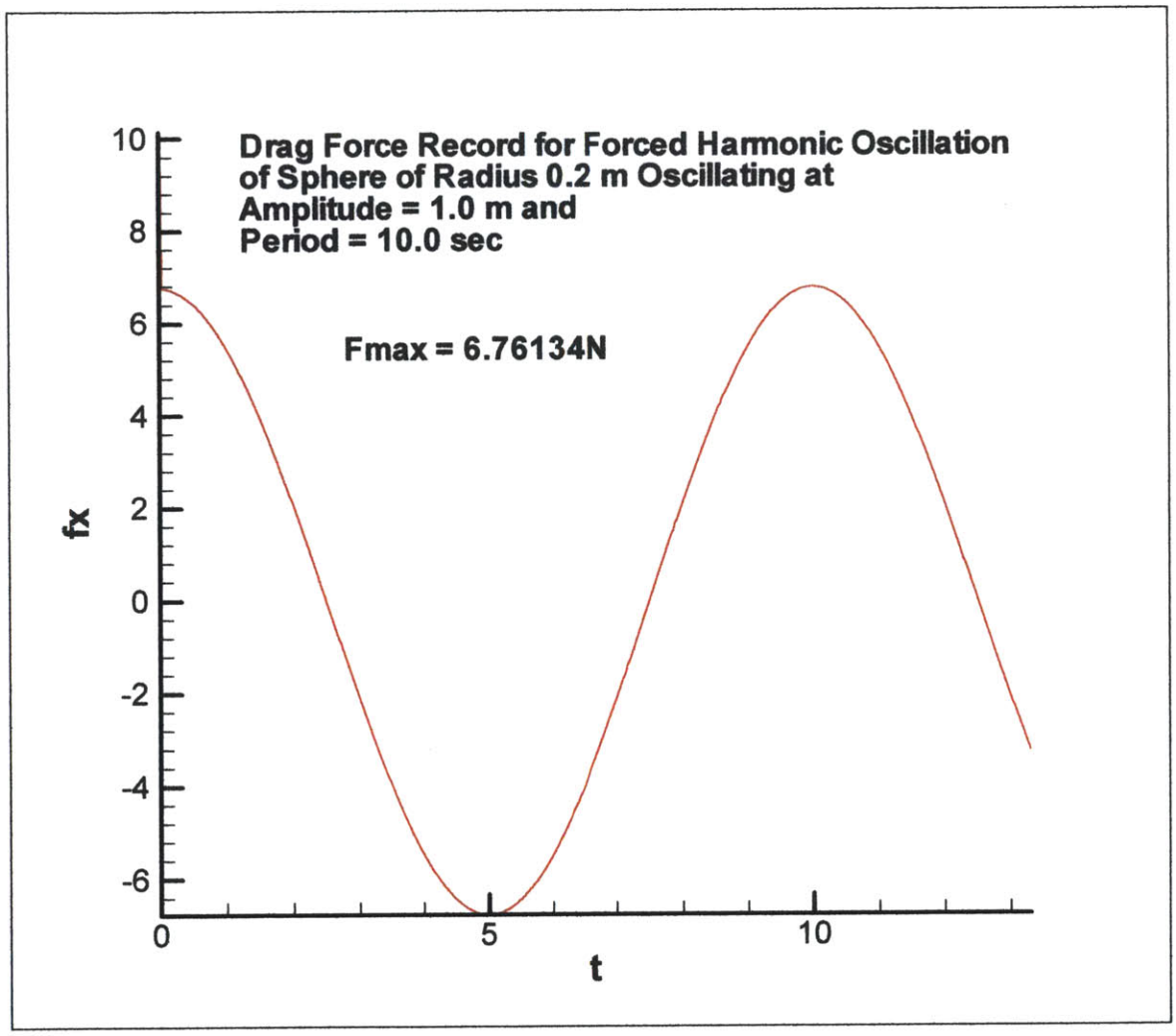

Figure 7

For the theoretical result, we get

$$M_a = \frac{1}{2}\rho\nabla = \frac{2}{3}\rho\pi a^3 = 17.174kg$$

The complete results from the SWAN simulations, with added mass derived using equation(20) are reproduced below in table and graphical forms.

Panels	Fmax	Ma
10	6.61726	16.7617
15	6.70609	16.9867
20	6.73829	17.0683
25	6.75324	17.1062
30	6.76134	17.1268

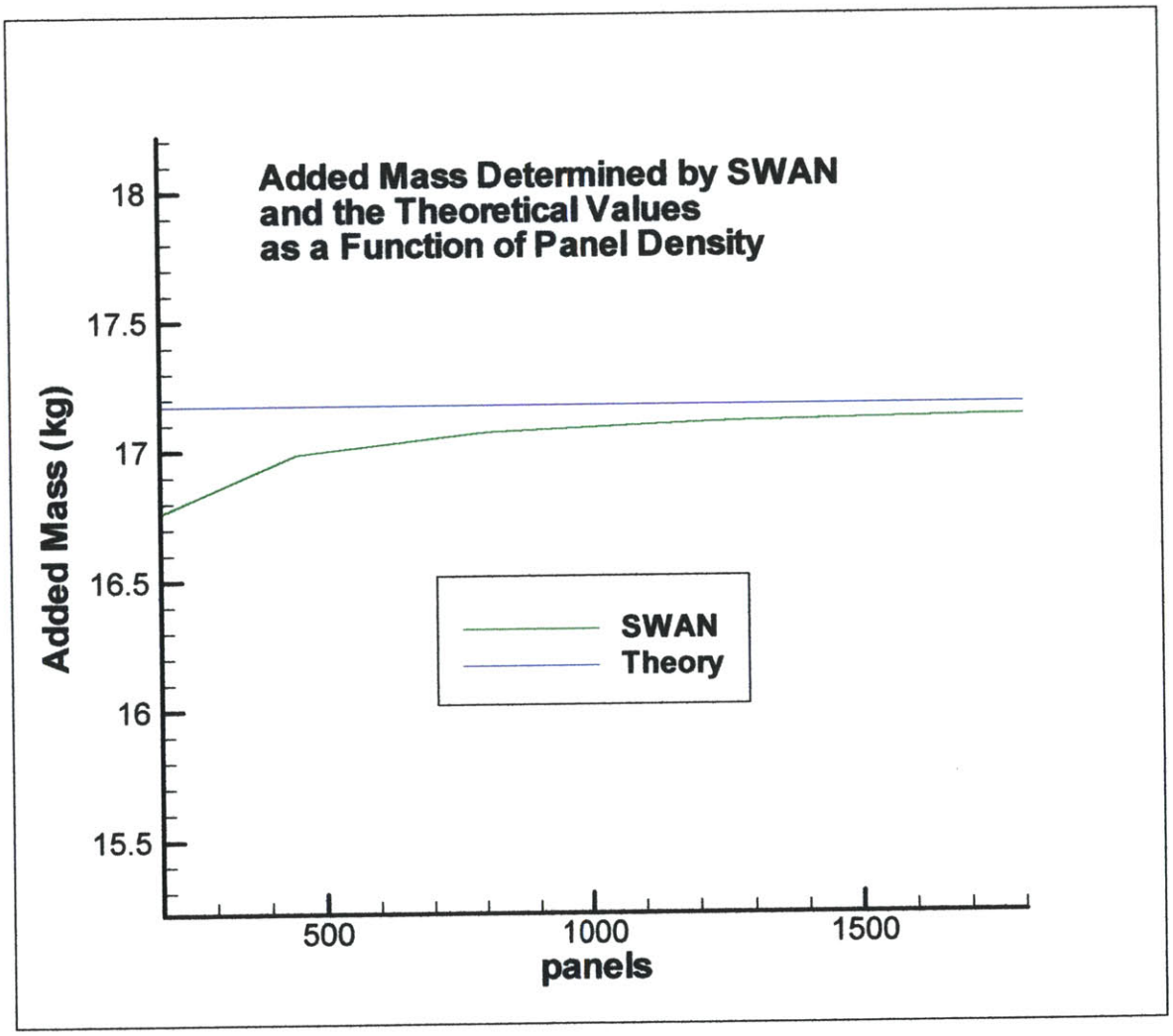

Figure 8

Note that here we do see the type of convergence to the predicted value that we expect with increasing panel density. At a panel density of 10, we get error of approximately 2.5% while at a panel density of 30, we get an error of only 0.28%. Note the suggested inverse quadratic relationship between panel density and percent error. A threefold increase in the panel density results in a percent error that is approximately 1/9 the previous value.

To conclude, the results generated by SWAN in the evaluation of a sphere are very accurate. Deviation from the expected zero values for both force and moment is minimal and we see good convergence to expected added mass values with increasing panel density.

ELLIPSOIDAL BULBS, Theory:

Analysis of an ellipsoidal bulb adds new complications to the SWAN simulation. Under steady translation, we still expect to see zero forces due once again to D'Alembert's Paradox and equation (16), but now we will get a moment, namely the Munk moment discussed briefly above. The Munk moment will occur in our case when the ellipsoidal bulb moves with an angle of attack.

Derived in Newman(1977), we now turn to the indicial forms of the force and moment equations.

$$F_j = -\dot{U}_i m_{ji} - \varepsilon_{jkl} U_i \Omega_k m_{li} \qquad (22)$$

$$M_j = -\dot{U}_i m_{j+3,i} - \varepsilon_{jkl} U_i \Omega_k m_{l+3,i} - \varepsilon_{jkl} U_i U_k m_{li} \qquad (23)$$

where

U_i = body velocity in direction i

Ω_i = body rotational velocity about axis i

$\dot{U}_i$ = body acceleration in direction i

m_{ij} = added mass in direction i due to motion/rotation in direction j

ε_{ijk} = alternating tensor

= 1 for ijk = 123, 231, 312

= -1 for ijk = 321, 213, 132

= 0 if i = j or i = k or j=k

For the steady translation problem, we can see that

$$\dot{U}_i = \Omega_i = 0$$

and therefore, no forces will result,

$$F_j = 0.$$

Additionally, equation (22) reduces to

$$M_j = -\varepsilon_{jkl} U_i U_k m_{li}$$

For the present analysis, we first note that steady translation along any of the ellipsoid's axes of symmetry will result in zero moment. Take, for example, nonzero velocity in the x direction (i=1) only. The only nonzero moments allowed by the alternating tensor in (22) are

$$M_2 = U_1^2 m_{13} \text{ and } \qquad M_3 = -U_1^2 m_{12}$$

However, due to the symmetry of the geometry in question we know

$$m_{12} = m_{13} = 0$$

and therefore, there will be no resulting moment.

The simulation we are interested in, however, involves a bulb at an angle of attack. Using the geometry in Figure 9, one can see that introducing an angle of attack effectively causes a velocity in two directions.

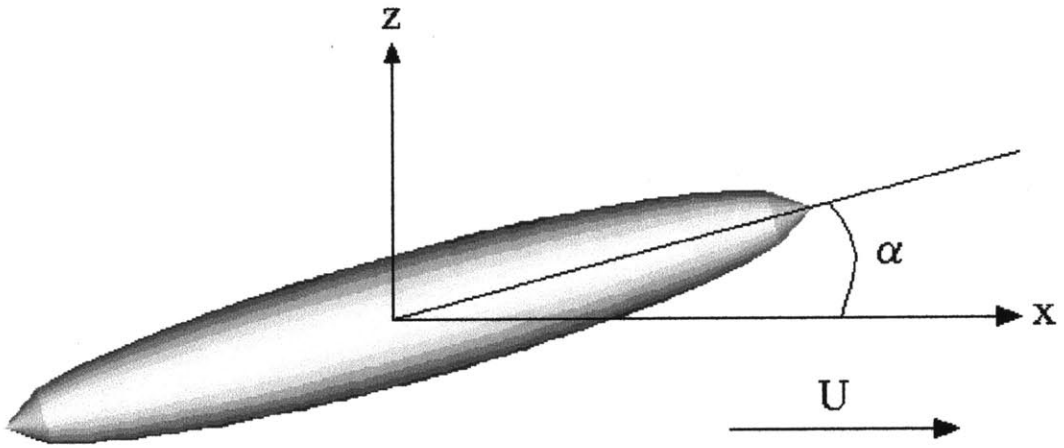

Figure 9

$$U_1 = U\cos(\alpha)$$

$$U_3 = -U\sin(\alpha)$$

With these two nonzero velocities, the formula for the Munk moment, derived from equation (22) above is

$$M_2 = -U\cos(\alpha)U\sin(\alpha)(m_{33} - m_{11})$$

which can be approximated using small angle approximations as

$$M_2 = -U^2(m_{33} - m_{11})\alpha\,.$$

This still leaves the question of the exact theoretical values of the surge and heave added masses. For this we got to Kochin et al (1964).

Using the following geometry,

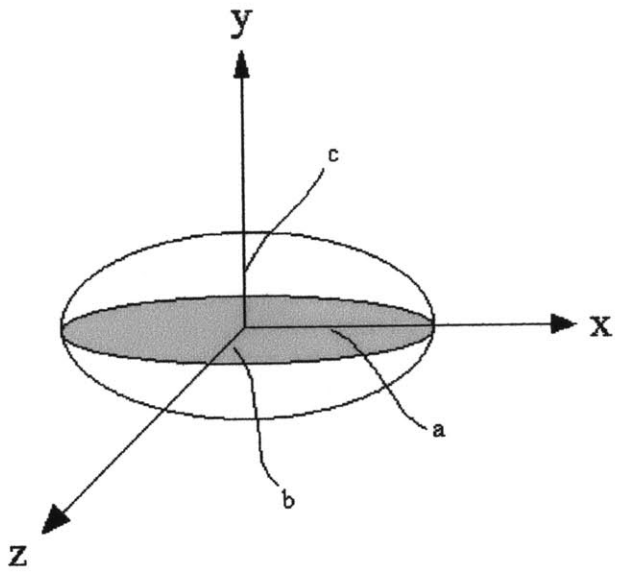

Figure 10

Kochin gives values for surge and heave added mass as

$$m_{11} = \frac{4}{3}\pi\rho abc\frac{A_\circ}{2 - A_\circ} \qquad (23)$$

and

$$m_{33} = \frac{4}{3}\pi\rho abc\frac{B_\circ}{2 - B_\circ} \qquad (24)$$

where

$$B_\circ = abc\int_0^\infty \frac{1}{(b^2 + x)\sqrt{(a^2 + x)(b^2 + x)(c^2 + x)}}dx \qquad (25)$$

and

$$A_\circ = abc\int_0^\infty \frac{1}{(a^2 + x)\sqrt{(a^2 + x)(b^2 + x)(c^2 + x)}}dx \qquad (26)$$

From equations (23) through (26) above, one can easily derive the added mass coefficients in question for any spheroidal geometry.

SWAN ADDED MASS RESULTS:

The same bulb geometry is used in all of the following SWAN simulations. The uninclined major axis was collinear with the x-axis. The two uninclined minor axes, equal in length, were collinear with the y and z-axes. The bulb is assumed to be a component of a typical IACC yacht keel and is accordingly nondimensionalized with the hull length. As a result,

Major axis a = 0.135
Minor axis b = 0.021
Minor axis c = 0.021

With these values in mind, we can look to the Kochin formulas ((23) through (26) above) and derive the following values:

$A_0 \cong 0.0408082$
$B_0 \cong 0.235890$

Therefore, our theoretical exact values for comparison to SWAN output are

$m_{11} \cong 0.010412$
$m_{33} = m_{22} \cong 0.23589$

Simulations were run at a velocity of 0.5 m/s, resulting in a formula for the Munk moment as follows:

$M_2 = -0.05637\alpha$

Saving analysis of the Munk moment for later we first concentrate on SWAN's ability to determine the added mass coefficients.

Two panelization schemes were employed in the analysis. First, a scheme with sinusoidal panel distribution over the length of the major axis seen at the top in Figure 11 below, and second, a scheme with an even panel distribution over the major axis seen at the bottom in Figure 11 below. Both use an even panel distribution radially.

In our examination of the heave added mass, it was decided that using heave oscillations in which the bulb's distance from the free surface varied might cause minor sources of error. Due to the symmetry of the geometry, however, we can see that the heave and sway added masses should be equal. As oscillation in the sway direction maintains constant distance from the free surface, an opportunity was seen to attain better accuracy by determining the added mass in sway instead of heave.

Sinusoidal Panel Distribution

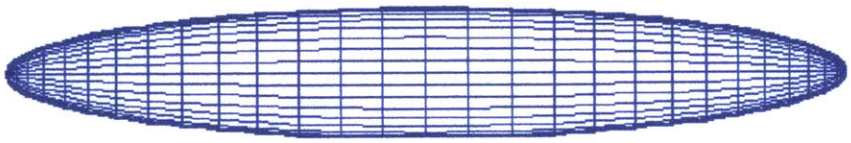

Even Panel Distribution

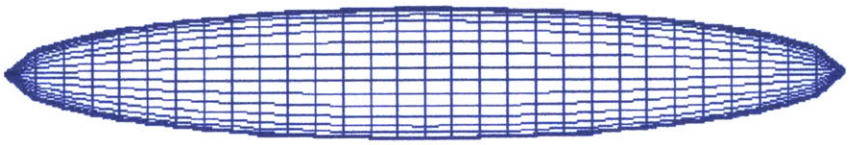

Figure 11

Similar to the added mass analysis of the sphere, the bulb undergoes forced harmonic motion in surge and sway with amplitude 1m and period 10 sec. Following the same derivation used in the sphere analysis above, we arrive at the equation

$$M_a = F_{\max}\left(\frac{25}{\pi^2}\right).$$

Results of the SWAN simulations for surge added mass are reproduced below. First, a typical force time history:

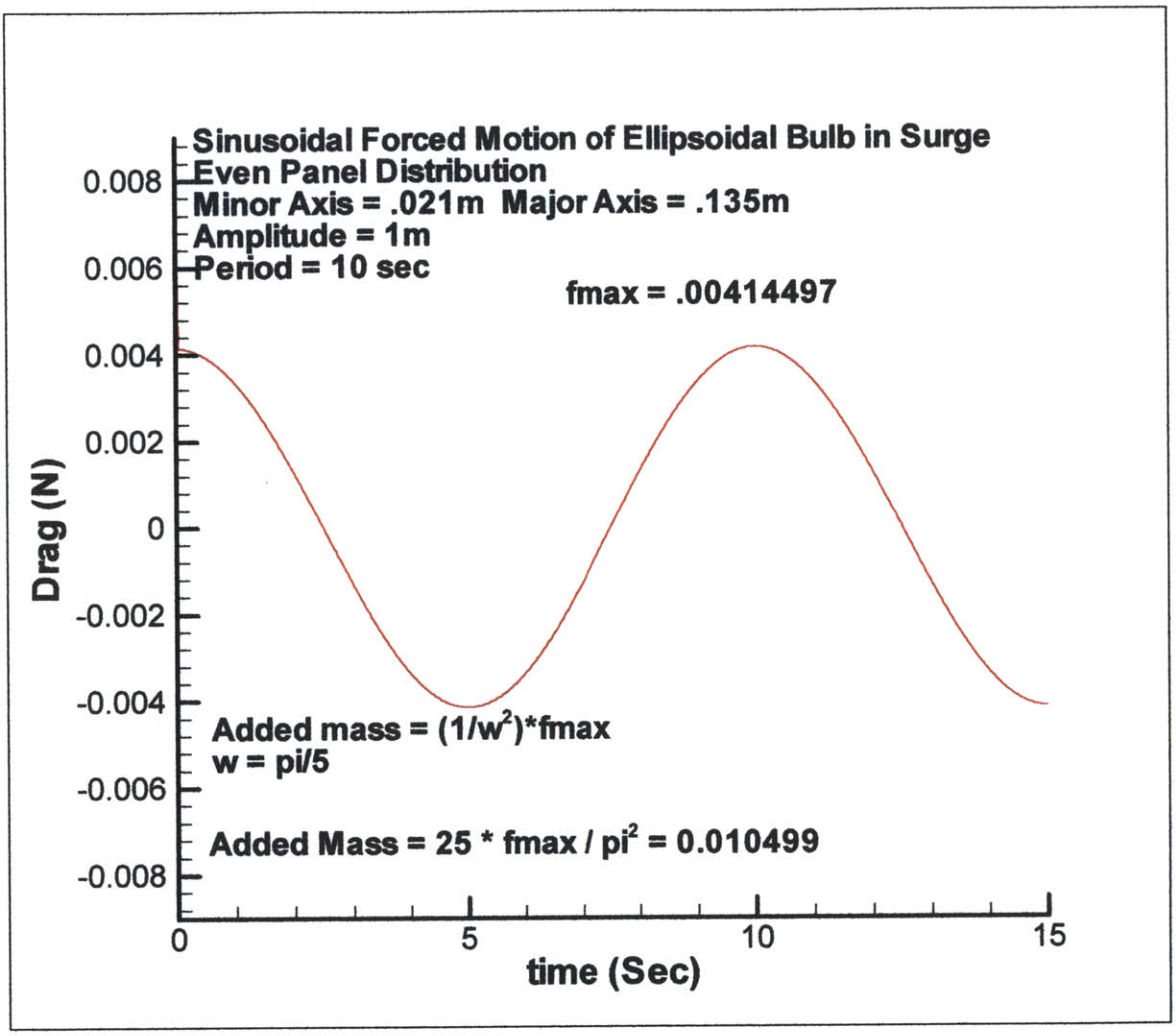

Figure 12

Several different panel densities were examined ranging from 312 to2400 panels over the surface of the ellipsoid. The following data were generated:

panels	Fmax(Even)	Ma(Even)	Fmax(Sine)	Ma(Sine)	Ma(Theory)
312	0.00428875	0.0108635	0.0039516	0.01001	0.010412
442	0.00419921	0.0106367	0.00400668	0.01015	0.010412
792	0.00420079	0.0106407	0.00406039	0.010285	0.010412
972	0.00417012	0.010563	0.00406326	0.010292	0.010412
1152	0.00414957	0.01051098	0.00406494	0.010297	0.010412
1332	0.00413496	0.010474	0.00406615	0.0103	0.010412
1612	0.00414294	0.0104942	0.0040669	0.010301	0.010412

2400 0.00412804 0.010456 0.00408576 0.010349 0.010412

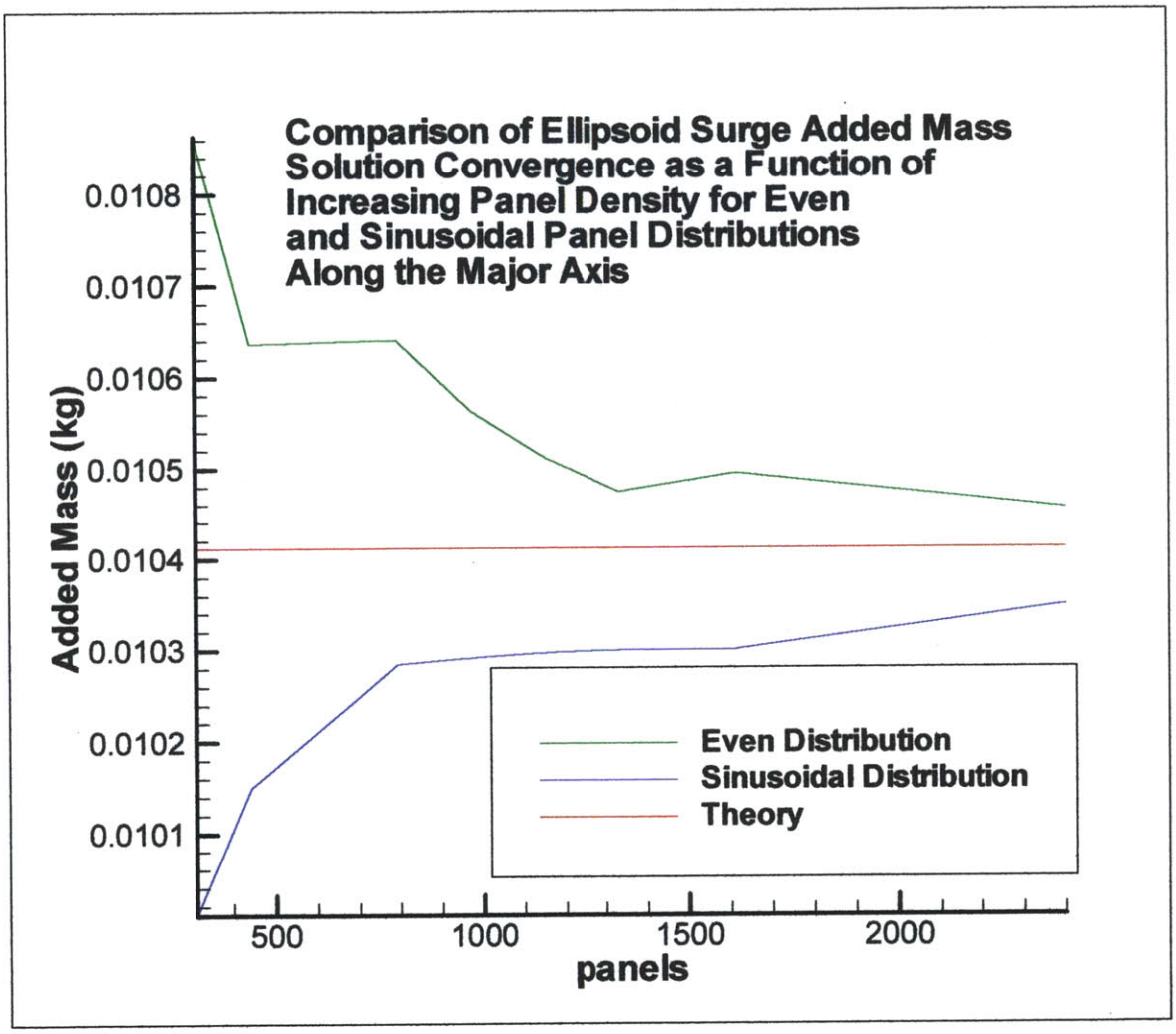

Figure 13

The most important aspect of these results is that they both converge on the exact value predicted by theory. Qualitatively, it seems as if the sinusoidal distribution might converge faster at lower panel densities but that the even distribution performs slightly better at higher densities.

As before, the amplitude of the sway motion was also set at 1m and the period set at 10 seconds. A typical time history is reproduced below.

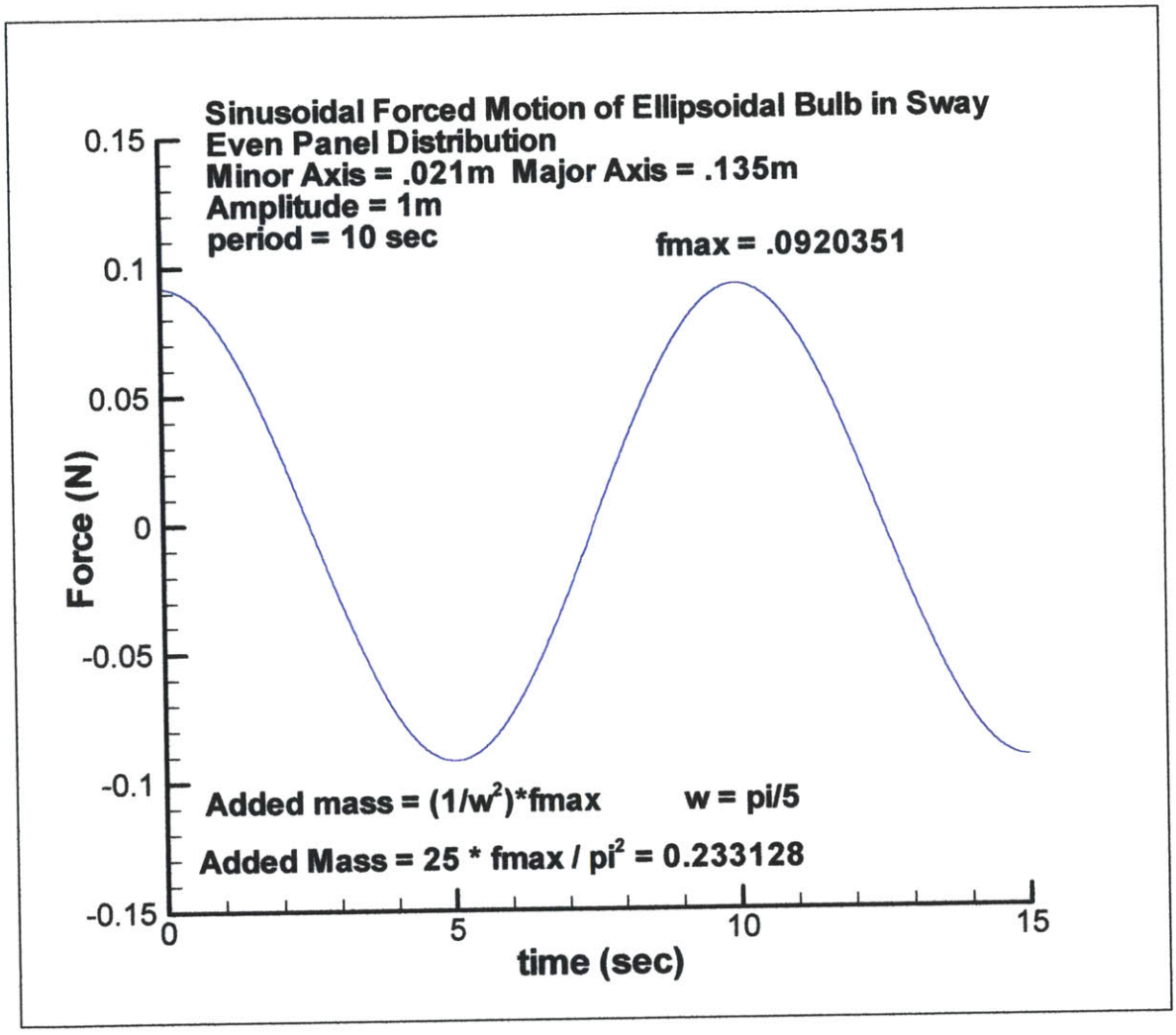

Figure 15

The same range of panel densities was used as was used in the surge analysis, varying from 312 to 2400 panels over the surface of the bulb. The following data were generated:

panels	Fmax(Even)	Ma(Even)	Fmax(Sine)	Ma(Sine)	Ma(Theory)
312	0.0887342	0.2247664	0.0906153	0.229531	0.23589
442	0.0906541	0.2296295	0.0917308	0.232357	0.23589
792	0.0914826	0.2317281	0.0921672	0.233462	0.23589
972	0.091865	0.2326968	0.0923594	0.233949	0.23589
1152	0.0921165	0.2333338	0.0924817	0.234259	0.23589
1332	0.092299	0.233796	0.092551	0.234434	0.23589
1612	0.092411	0.2340798	0.0925927	0.23454	0.23589
2400	0.0926411	0.2346626	0.0926411	0.2346626	0.23589

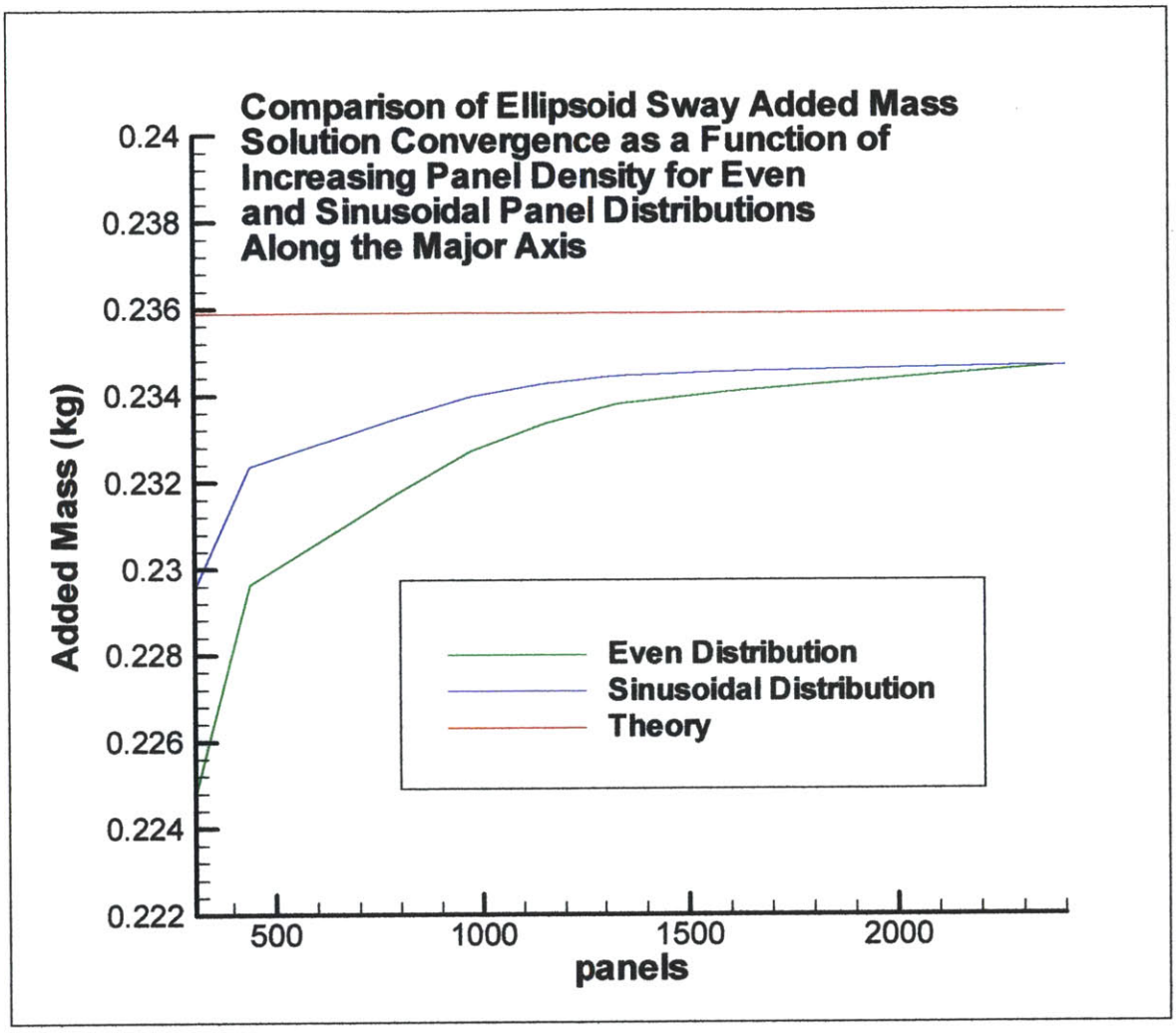

Figure 16

Most importantly, we again note the convergence towards the expected value. We also see that while the sinusoidal distribution performs better at lower panel densities, the even distribution seems to deliver equal or better performance at higher densities.

SWAN MUNK MOMENT RECOVERY:

Having validated the results of the SWAN produced added masses, the next step in the project was to run the ellipsoidal bulb at a variety of angles of attack and examine the resulting force time records. As mentioned above, we expect to see zero forces and moments except for the Munk moment, described by (22) above.

The same bulb geometry as was used in the added mass analysis was also used in the following simulations. An even panel distribution is employed and the bulb is constructed of 30 panels in the longitudinal direction and 30 panels radially.

The bulb was inclined to the x-y plane. Angles of attack ranging from 0 to 32 degrees were examined. The center point was submerged 2 meters below the surface to eliminate free surface effects.

Two panelization schemes were used. However, each had identical geometry. The difference was merely that the first scheme arranged the panels in one continuous sheet around the body whereas the second broke the body into two sheets along the uninclined x-y plane. The errors generated by the first scheme eventually motivated the second.

In our subsequent discussion of error, we again take as our reference force stagnation pressure times the uninclined frontal area, and obtain

$$F_{ref} = \frac{1}{2}\rho U^2\left(\pi b^2\right) = 0.177N$$

The following data, excluding the Munk moment, were obtained from the first, single sheet setup.

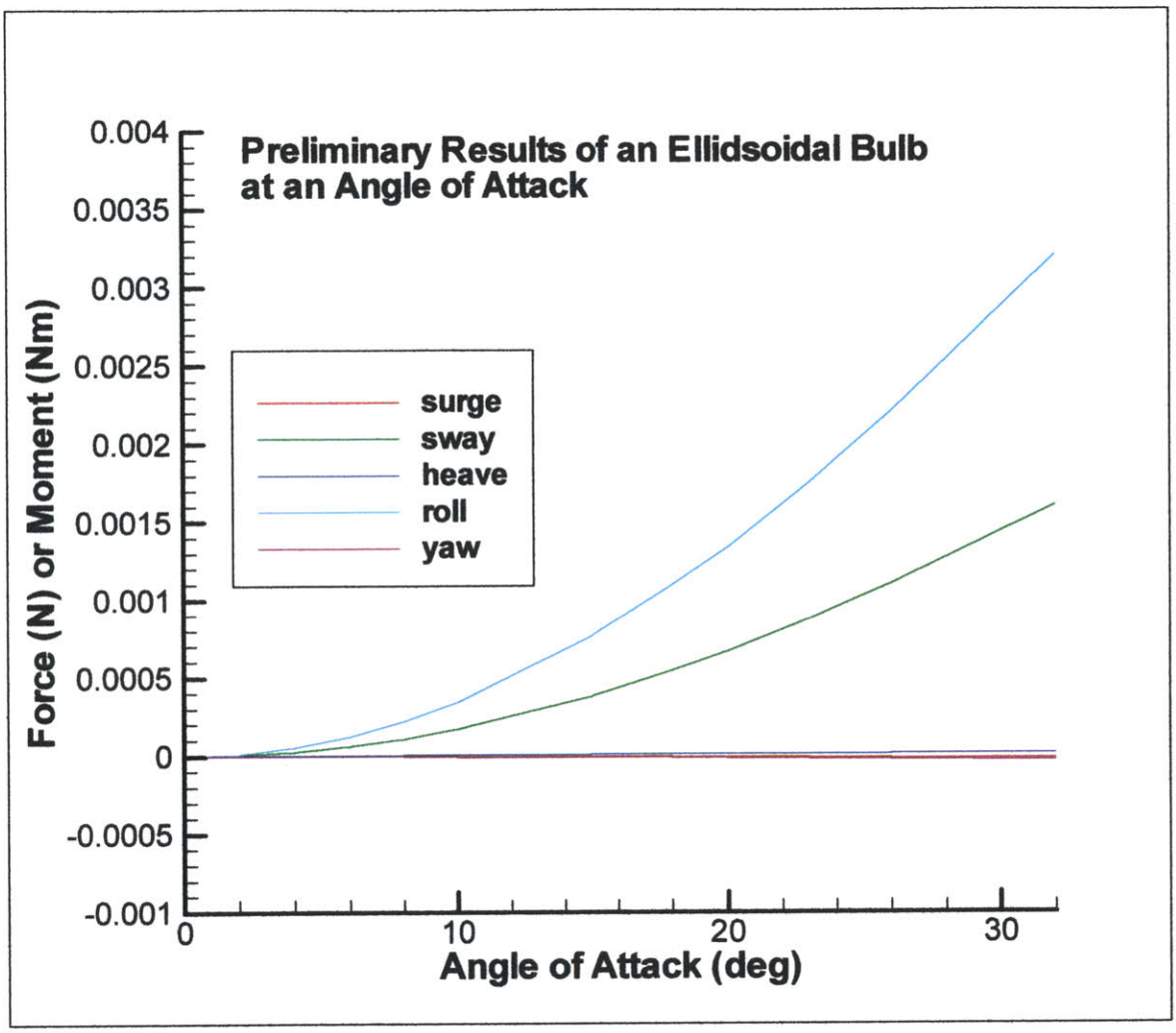

Figure 17

The first conclusion made from the plot above was that the roll moment was merely a byproduct of the erroneous sway force. If we subtract the moment generated by this force at a distance of 2m from the origin from the SWAN generated roll moment, we recover the independently computed SWAN roll moment and the results begin to look better.

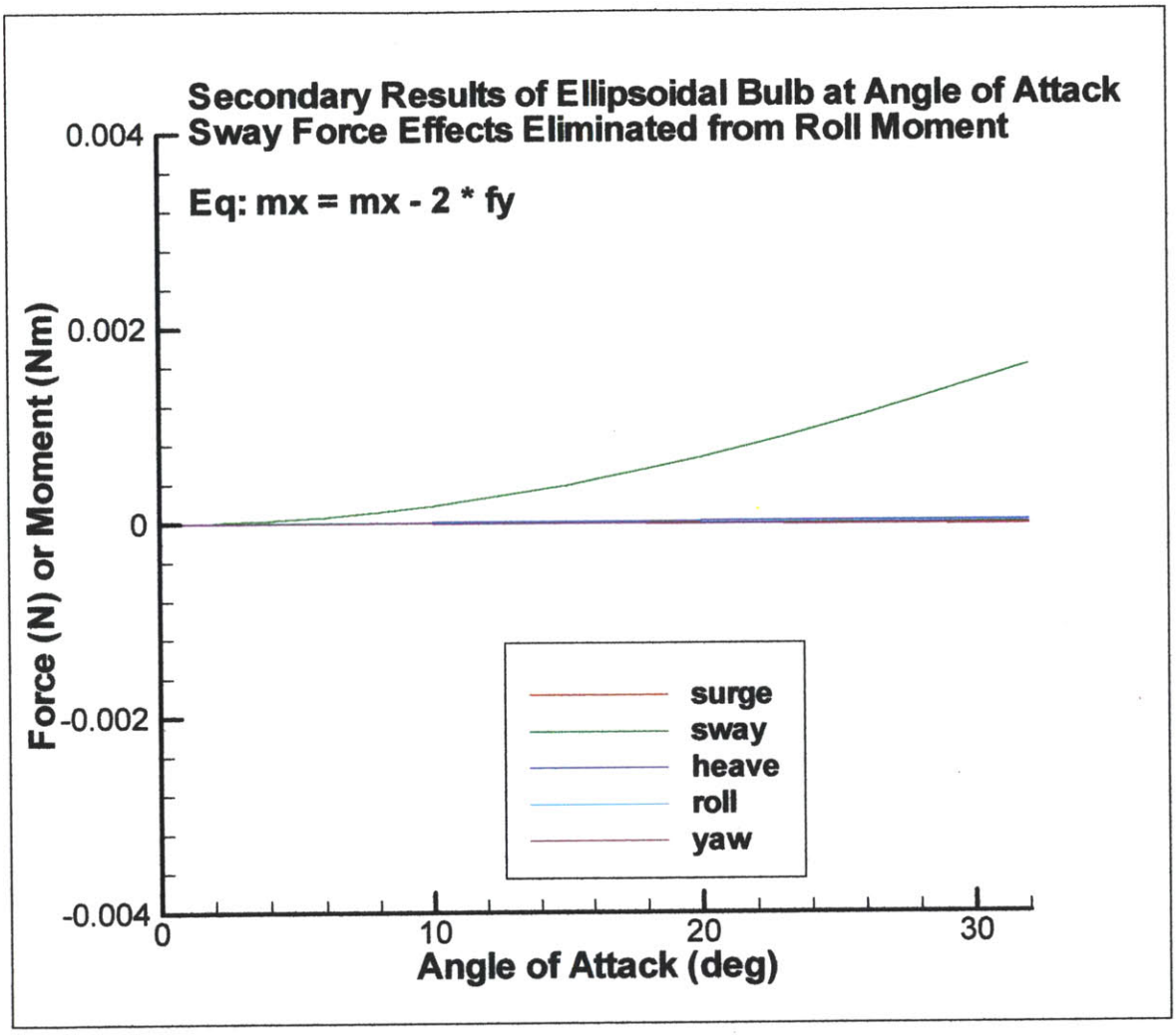

Figure 18

It is worthwhile to note that while the erroneous sway force is still small compared to our reference force being on the order of 10^2 times smaller, it is still quite large compared to the other forces and is therefore a source of some concern.

It was surmised that this force might have been a result of the asymmetry of the panel sheet setup. With a sheet boundary running along only one side of the bulb, any errors due to that boundary would occur only on that side and may therefore be the cause of the fictitious sway force.

A subsequent attempt used the second panelization scheme, cutting the bulb into two separate sheets meeting on the x-y plane of the uninclined bulb. Preliminary results are as follows, again eliminating the Munk moment from the present discussion.

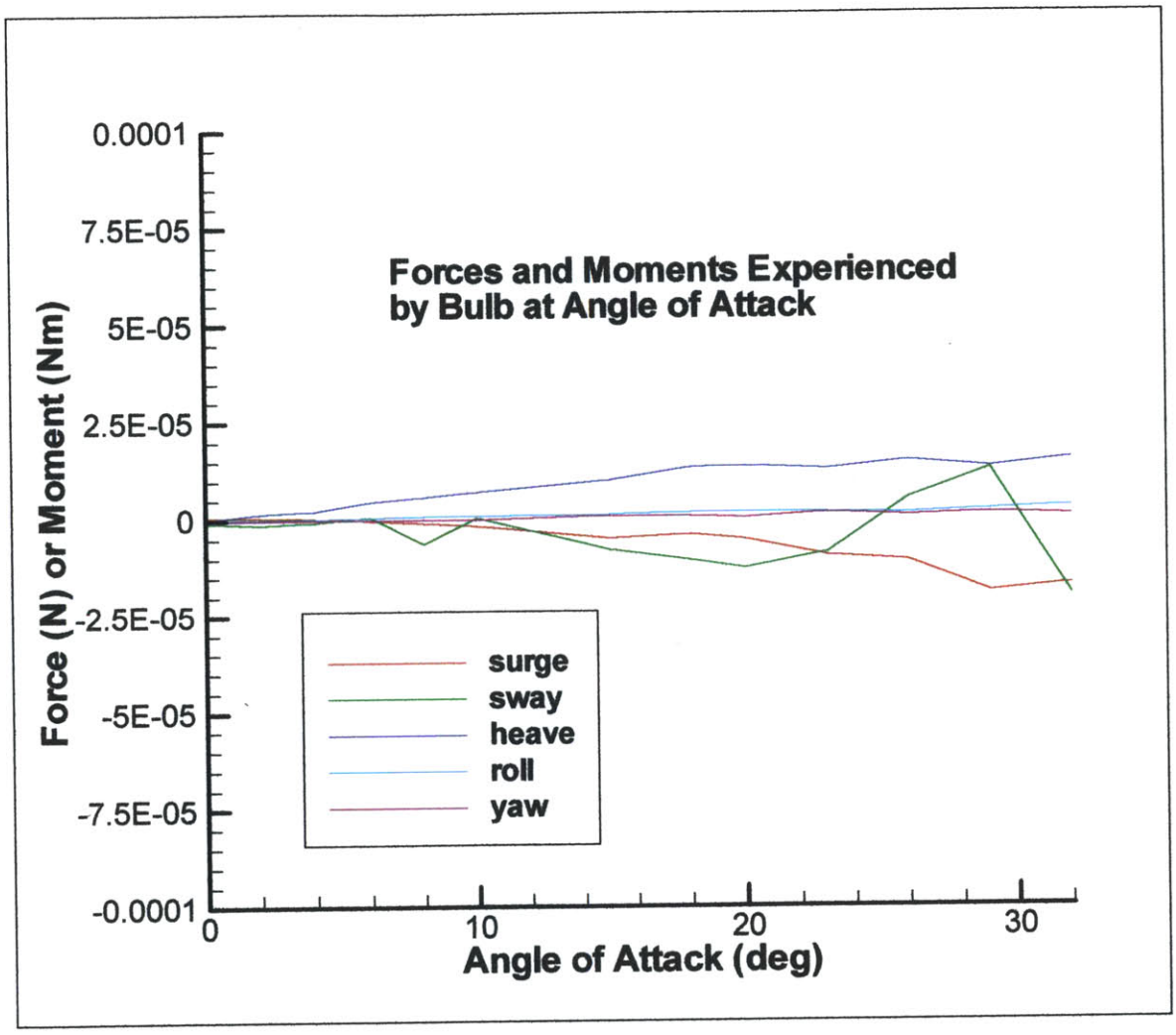

Figure 19

Clearly, this is an improvement over the previous simulations, with any errors being on the order of 10^4 times smaller than the reference pressure. Due to these results, all subsequent simulations employ this two-panel setup.

The only concern remaining is the Munk moment. Returning now to this aspect of the problem, the following plot shows the predicted Munk moment derived above as well as the Munk moments produced by SWAN and the SWAN produced moments multiplied by a factor of two.

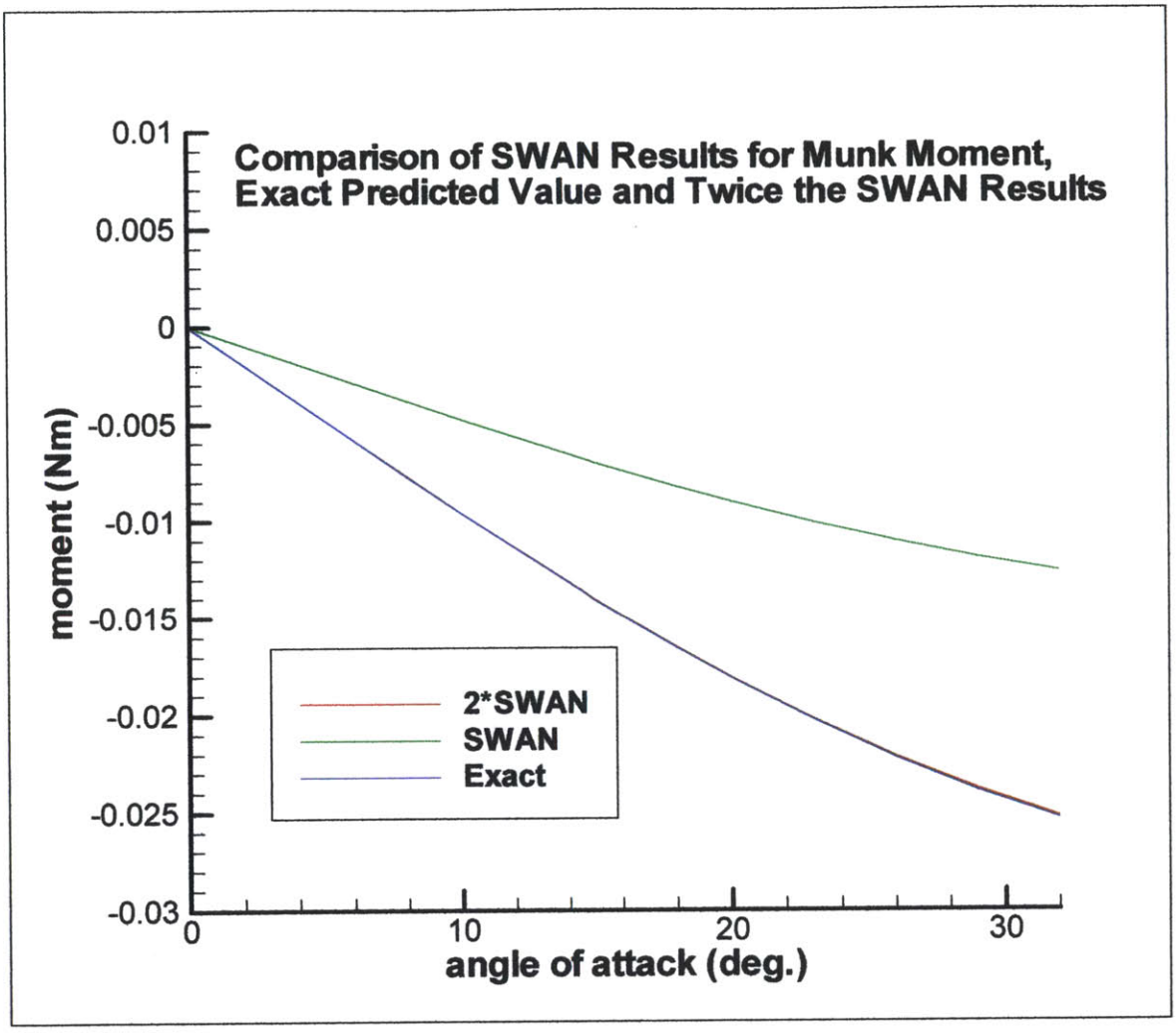

Figure 20

Clearly, the preliminary SWAN results compare quite unfavorably with the predicted outcome. However, the near exact agreement between the doubled SWAN result and theory make it fairly evident that the error involves a small problem somewhere in the SWAN coding rather than anything on the background theory level.

Further evidence of a problem with the results comes from a plot of the dynamic pressure over the surface of a bulb at zero angle of attack, reproduced below.

Preliminary Hydrodynamic Pressure Plot Resulting from Uncorrected Basis Flow Generation Routine in SWAN's SETUP Routine

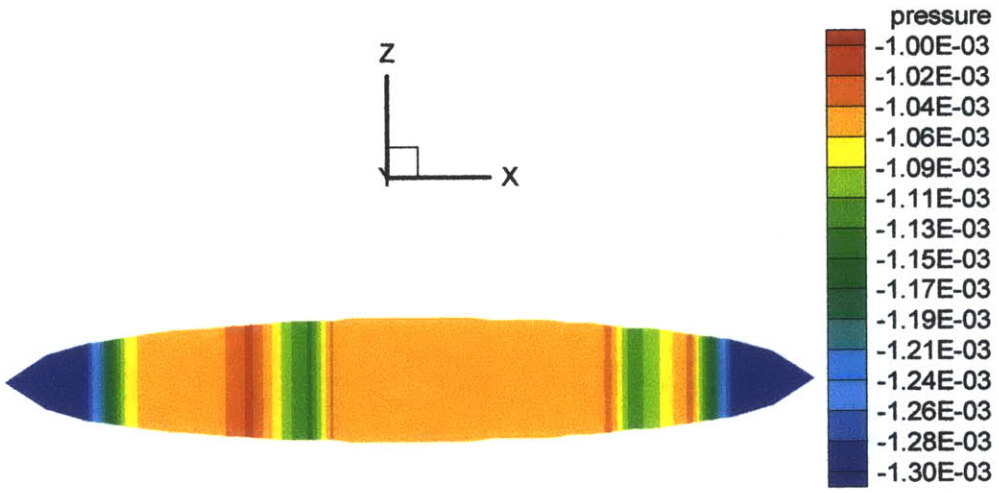

Figure 21

The most troubling aspect of this plot, aside from the rather arbitrary and asymmetric nature of the pressure changes, is that it violates Bernoulli's equation. This equation implies an inverse relationship between fluid velocity and pressure. As a result, speaking generally, we expect to see the highest pressures at the leading and trailing ends, where stagnation points occur (using a reference frame fixed to the body).

These concerns were voiced to MIT research fellow, Dr. Sungeun Kim, who made adjustments to the code. The adjusted code produced the following plot of Munk moments. Note also, that results for both the one and two sheet panelization strategies are included.

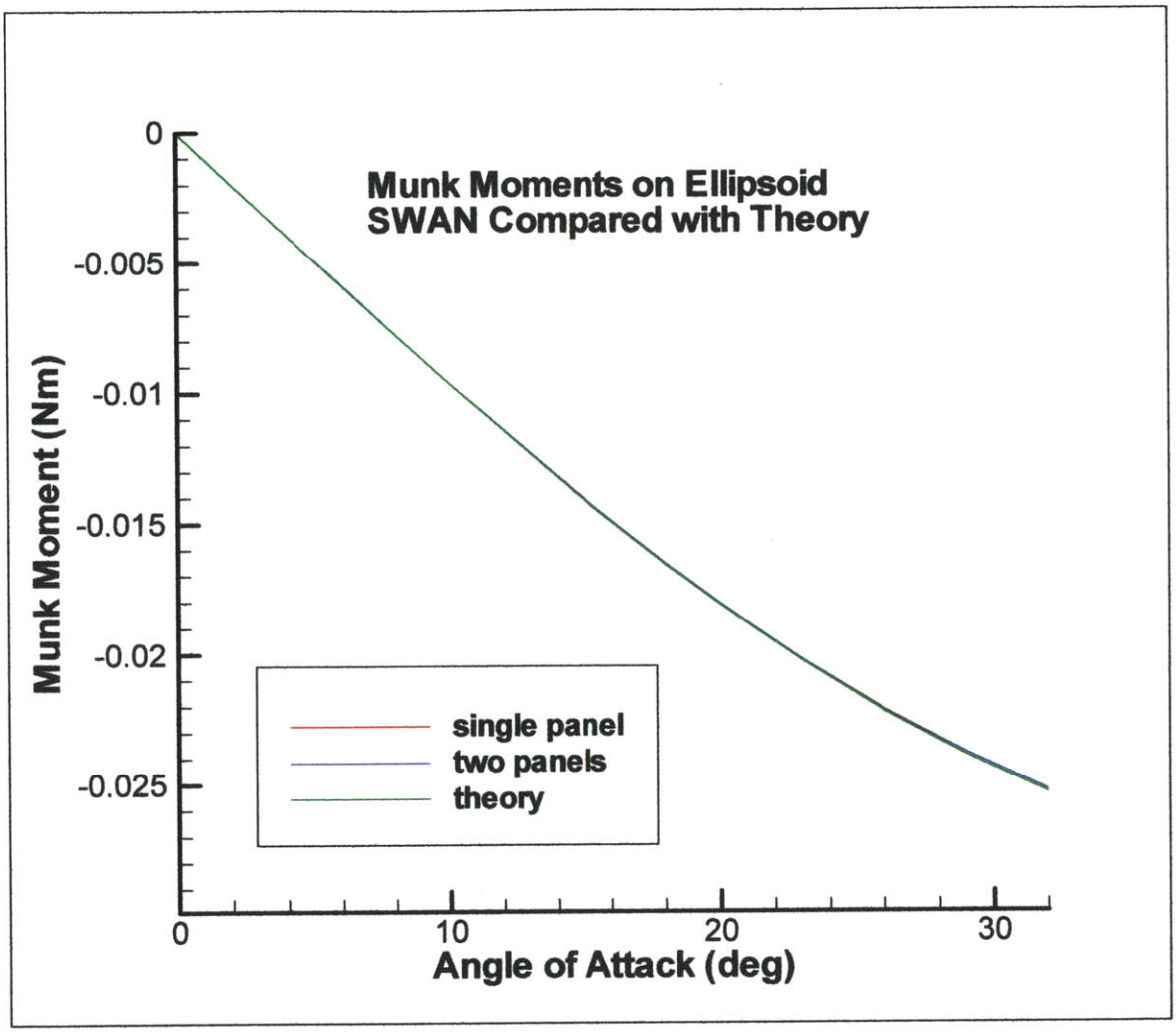

Figure 22

Clearly, the adjustments were successful as now SWAN is producing good results for the Munk moment with both schemes. The following plot shows a comparison of the error generated in order to confirm that the two sheet method having proven successful at eliminating erroneous sway forces is preferable in the analysis of the Munk moment.

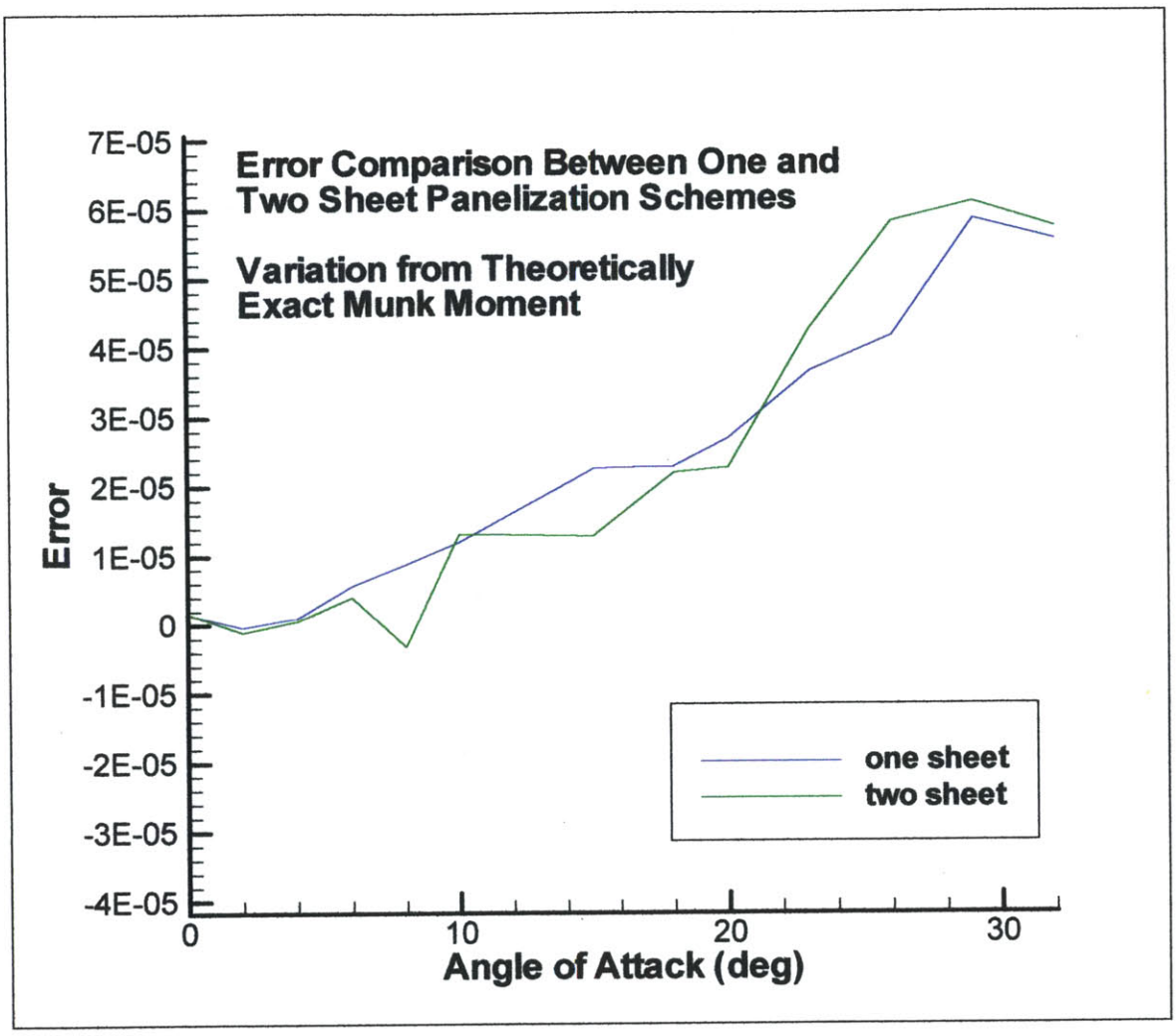

Figure 23

From the plot above, we can see two things. First, there are similar levels of error in each panelization scheme, so the breaking up of the bulb did not adversely affect the Munk moment results. Secondly, the error is small compared to the theoretical Munk moment being on the order of 500 times smaller, representing an error of approximately 0.2%. We conclude from this that the two sheet meshing is the superior option.

Returning briefly to the dynamic pressure over the surface of the bulb, Figure 24 below shows that the adjustments which resulted in accurate Munk moments also solved the problem with the pressure plots.

Hydrodynamic Pressure Plot Resulting from Corrected Basis Flow Generation Routine in SWAN's SETUP Routine

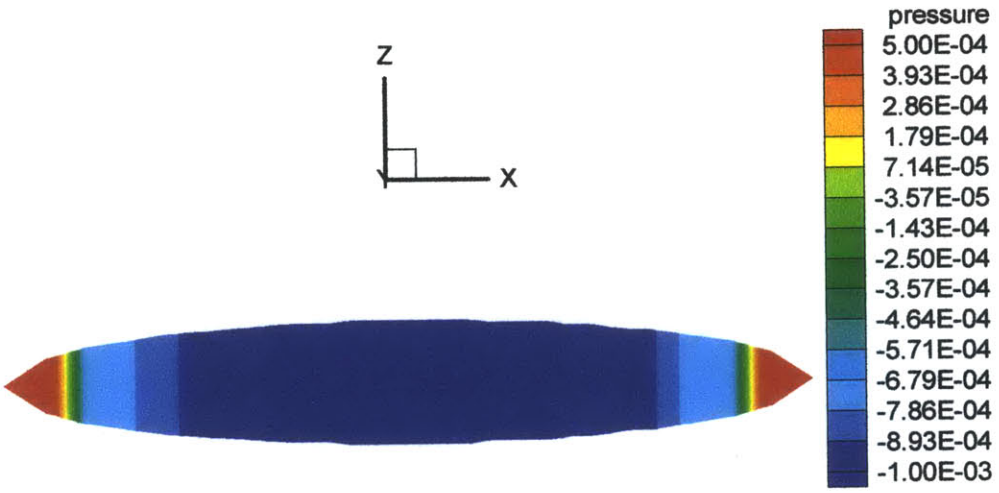

Figure 24

Note that now we do see, as expected, high pressure at the leading and trailing ends of the bulb, as well as a rather reassuring symmetry to the pressure changes.

Note also that all added mass convergence tests run with the corrected SETUP returned identical results to those produced above and, as a result, need not be reproduced here.

With SWAN now producing good values for the Munk moment, a convergence test was run in order to demonstrate that SWAN's results converge on the exact theoretical value with increasing panel density. The same geometry was used and the bulb was run at an angle of attack of 10 degrees at a velocity of 0.5 m/s. The exact theoretical value for the Munk moment in this simulation, obtained from equation (22), is $9.848*10^{-3}$. Bulb panel density was varied from 80 to 1680 panels over the surface of the bulb. The results for the Munk moment are reproduced below.

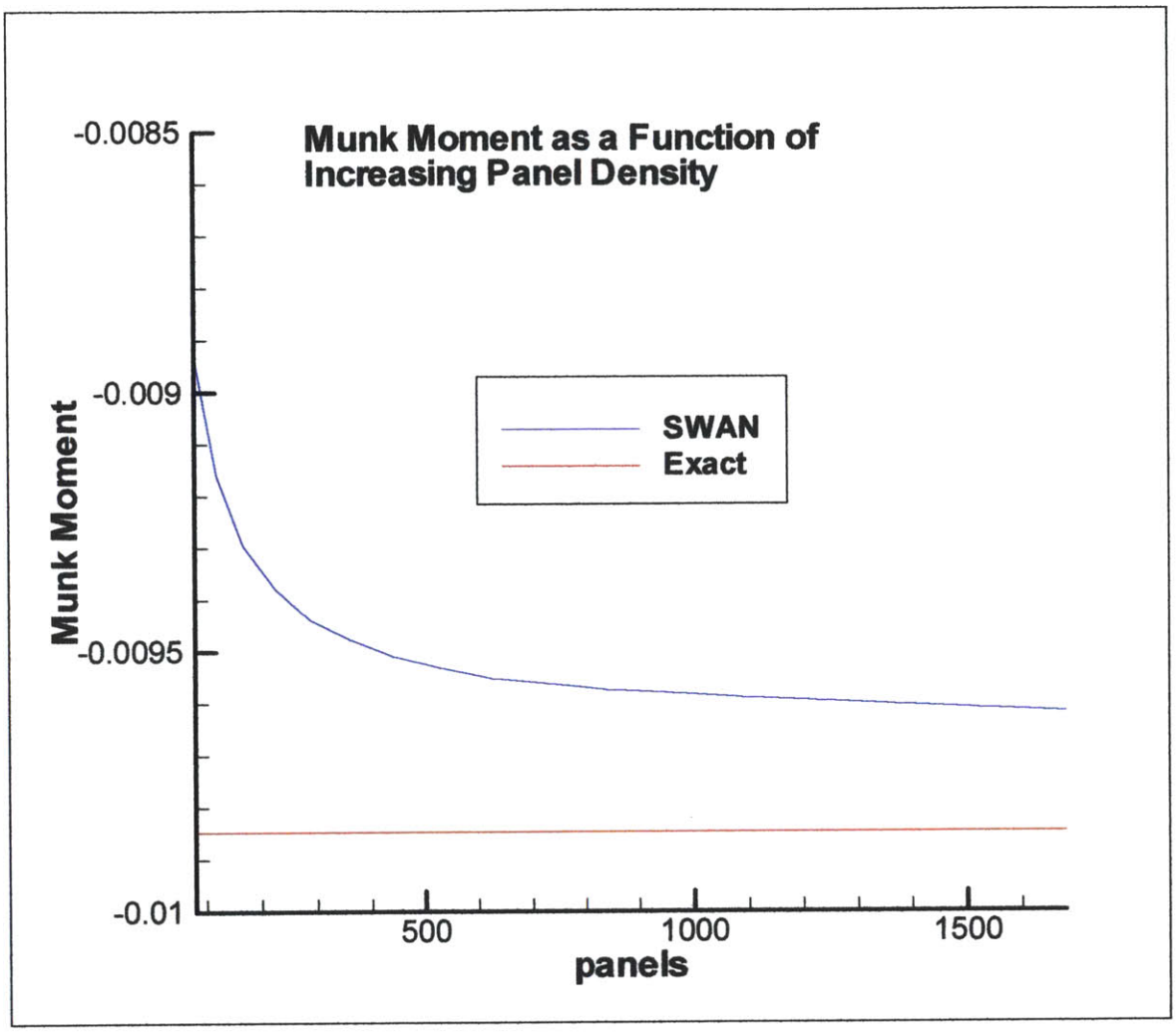

Figure 25

Conclusions from the plot above are that the SWAN results are indeed converging on the exact value as expected. A plot of the densest meshing is included below.

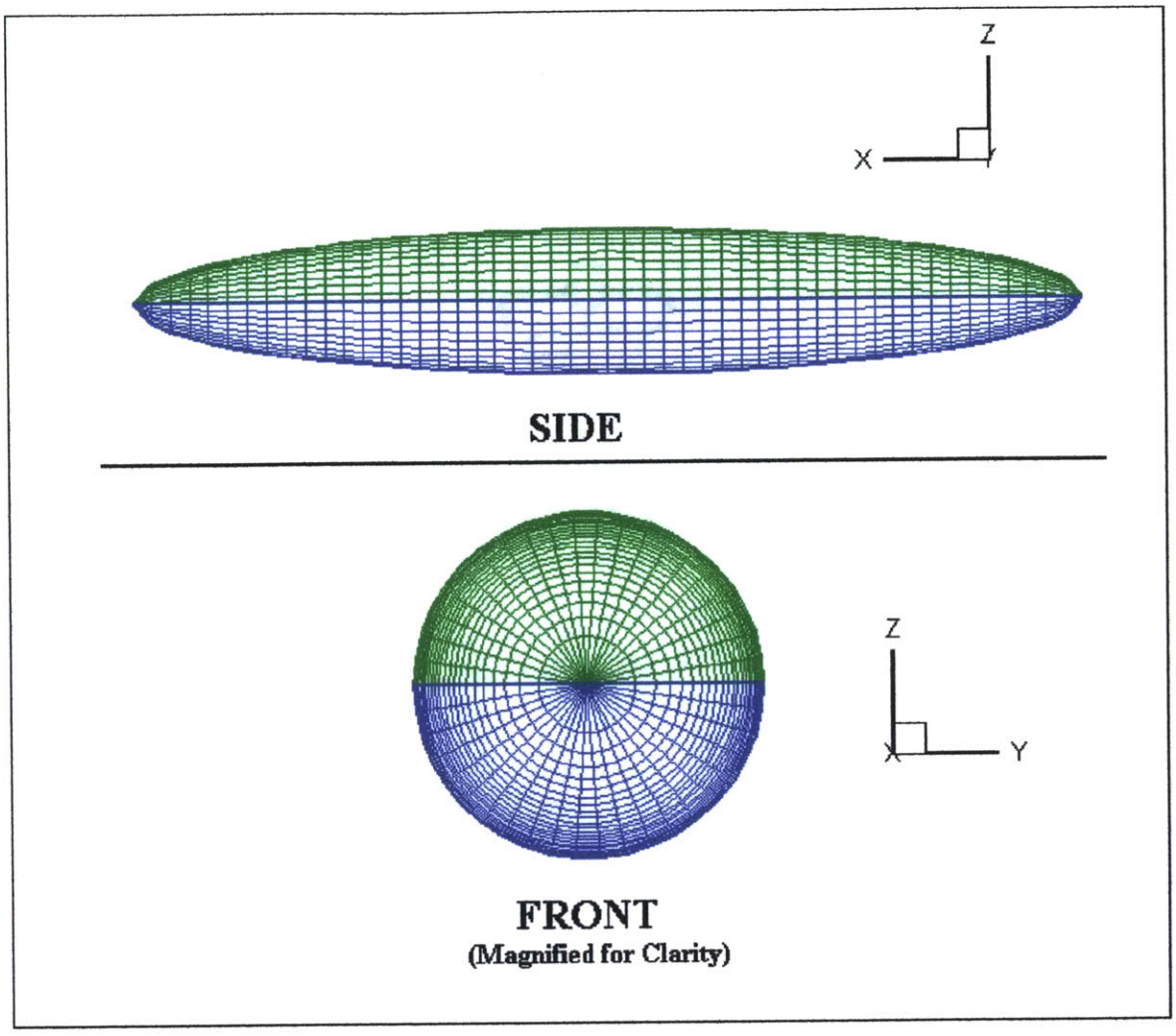

Figure 26

To conclude, the results generated by the corrected SWAN in the evaluation of an ellipsoidal bulb are very accurate. Deviation from the expected zero values for both force and moment is minimal. We get good agreement with theory for the Munk moment and see good convergence to expected added mass values with increasing panel density.

THE SYMMETRIC FOIL:

A typical symmetric foil was chosen for this portion of the simulation, with geometry as shown in Figure 27 below. Several values are of interest in the associated simulations, including lift, moment and induced drag. Note that for a horizontal foil undergoing translation at an angle of attack, we expect to see only these effects and no others. Therefore, sway forces should be nearly zero, and roll and yaw moment should be zero as well.

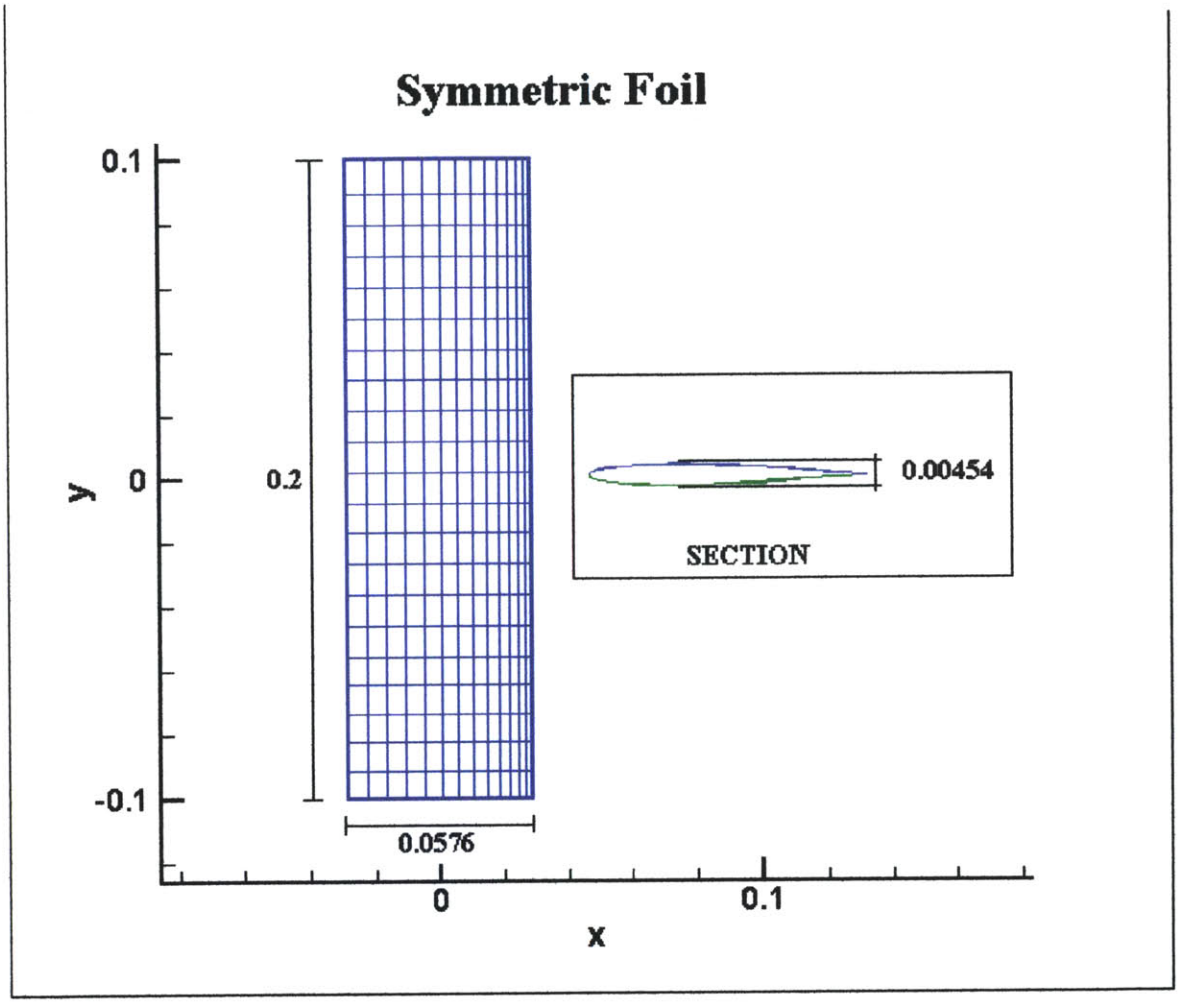

Figure 27

In section, the foil is elliptical from the leading edge back to the quarter-chord point where it attains maximum thickness. Aft of the quarter-chord point, the foil section goes to zero thickness at the trailing edge quadratically, in a manner that ensures zero slope at the intersection of the forward and aft sections.

Note that the foil is assumed to be a component of a typical IACC yacht keel, and is accordingly nondimensionalized with the hull length.

Therefore,

Span, $S = 0.2$,
Chord length, $c = 0.05767$,
and thickness, $t = 0.00454$.

Note also that in conformity with lifting surface convention, the leading and trailing edges are located at c/2 and –c/2 respectively and the mid-span point is located on the x-axis. In addition, for all simulations, a planar wake sheet was included that was attached to the foil at the trailing edge, extended over the entire span of the foil in width and some variable distance down stream in length, that appropriate distance being a quantity of interest for convergence testing. The function of this wake sheet was to allow for a velocity jump across its upper and lower surfaces, with convergence to equality occurring at the limits. This method allows for the generation of lift along the foil.

Two conditions are required to proceed with our potential flow lifting surface analysis if any further applications are expected in a viscous regime. First, the foil shape must be thin. Thin in this context implies that the form is not bluff and therefore causes little separation as it passes through the water. Secondly, and again to avoid separation, the foil must be operated at small angles of attack. This small angle of attack assumption is used in developing the various formulas below and therefore, it can be stated that an error is small if it is less than that produced by this small angle approximation.

Potential flow theory taken from Hoerner(1985) gives us the following formula for the lift force on a finite length rectangular foil undergoing translation at an angle of attack.

$$L = \frac{1}{2}\rho U^2 A_p C_L' \alpha$$

where planform area,

$$A_p = Span * Chord = 0.011534,$$

and lift curve slope taken from Hoerner,

$$C_L' = \frac{1}{\frac{1}{1.8\pi} + \frac{1}{\pi AR} + \frac{1}{2\pi AR^2}} \qquad (27)$$

where aspect ratio,

$$AR = Span / Chord = 3.46921$$

This gives us a value for the lift coefficient slope of

$$C_L' = 3.54842$$

Setting the foil velocity at a constant 0.5 m/s, we then expect a theoretical lift of

$$L = 5.23872\alpha . \qquad (28)$$

CONVERGENCE TESTING:

An examination of panelization schemes was done, testing for convergence to the expected lift value calculated above. The first attempt involved varying the density of the panelization on the foil itself and ascertaining the affects on accuracy. In all cases, the angle of attack was 10 degrees and the wake sheet from the trailing edge extended to x = -0.2. Note that this angle of attack theoretically produces a lift of

$$L = 0.91422N,$$

which is taken as the exact solution below.

Due to the geometry of the foil, the number of panels along the span was kept at twice the number of panels along the chord. The number of panels along the chord varied, with values of 10, 13, 15, 18 and 20 panels. It was found that 20 panels was the maximum allowed due to panel number limitations. Results of this series are reproduced below in graphic form.

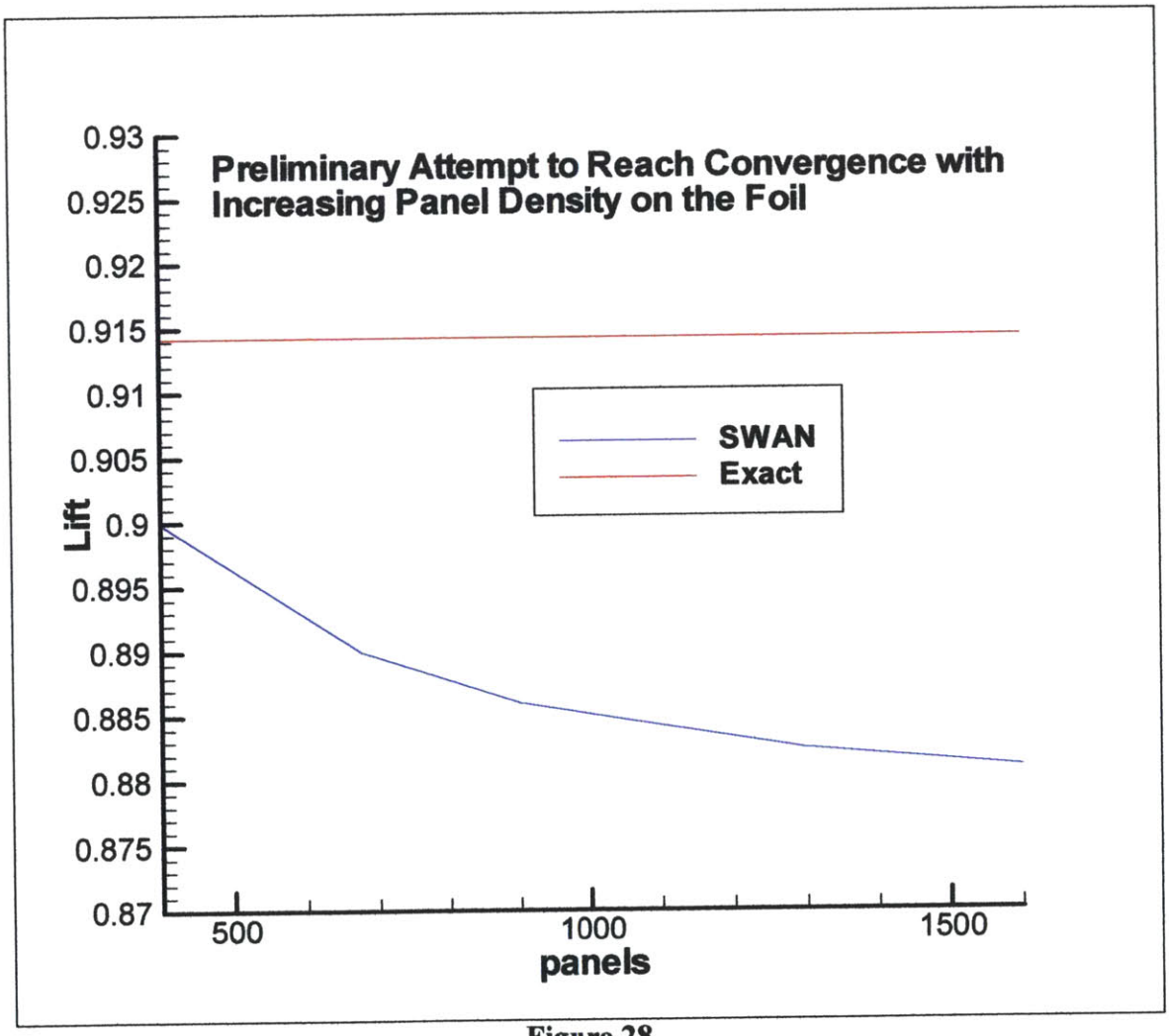

Figure 28

While it can be seen that the increasing density does lead to convergence for lift, the solution which is being converged upon is quite inaccurate with an error of 3.7% at maximum panel density, far greater than the 0.5% that our small angle approximation error allows.

Significantly, the value converged upon in the simulations above is less than the theoretical lift calculated previously, leading to thoughts that perhaps the velocity differences in the wake were not able to attain the levels required for accurate results. It was surmised therefore that the lack of accuracy could be overcome by adjusting the composition of the wake sheet. Either the original wake sheet was not long enough, or it did not contain enough panels, or both. Two sets of simulations were run to test the effects of increased wake panel density and increased wake length. Both tests were run on the 15 x 30 foil panelization.

In the first test, the length of the wake was kept constant, extending now to x = -0.4. The expansion ratio of the panels was varied from 1.01 to 1.05 in order to ascertain the effects of panel density on solution accuracy. The resulting number of panels composing the wake sheet then varied between 810 and 1320. The results of this series are reproduced below in graphic form.

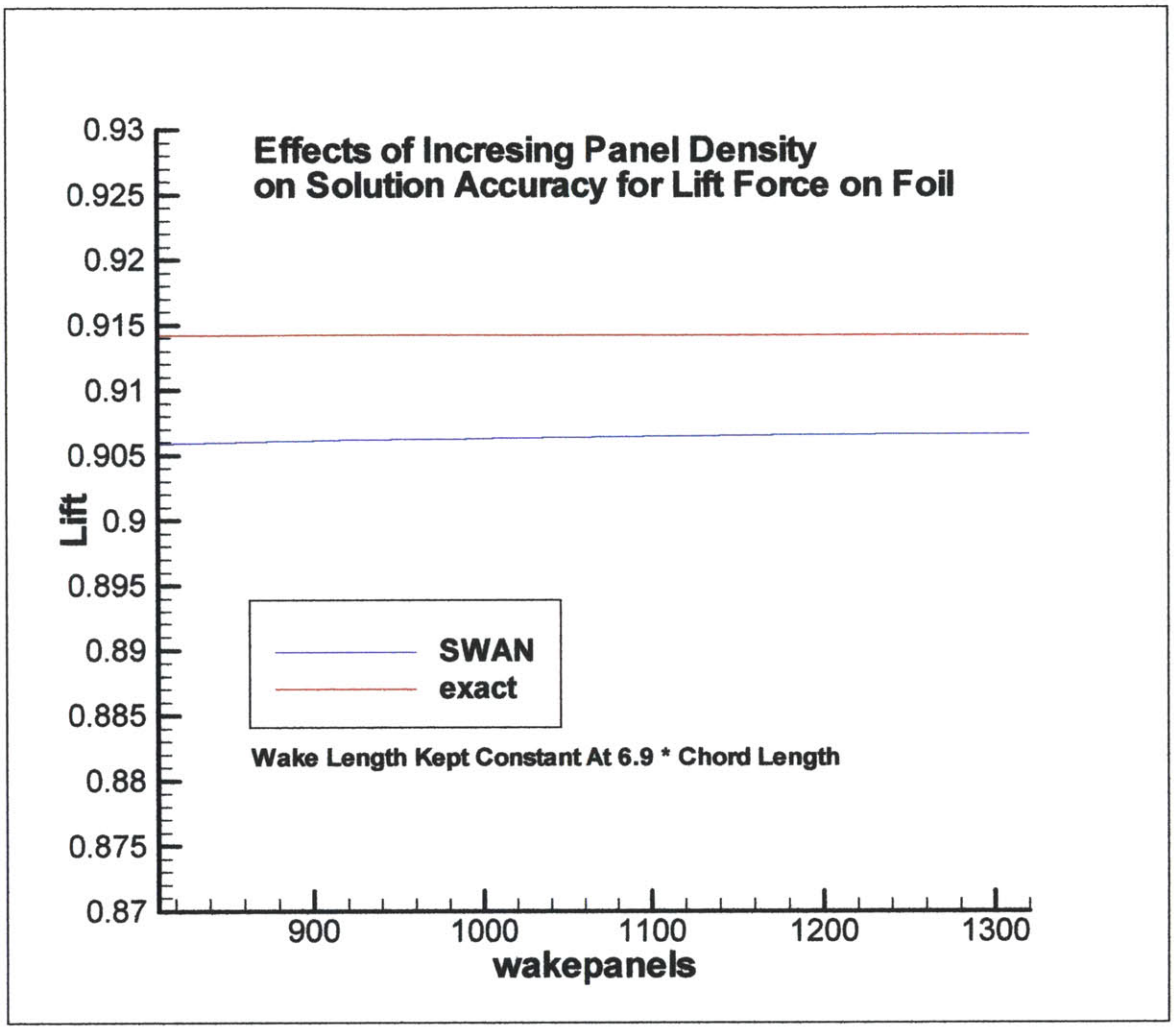

Figure 29

In Figure 29 above we can see that the solution is now converging on the correct answer. However, the rate of convergence is very slow and the error is still quite significant. At the maximum allowed panel density, we still see an error of 0.8%. While this is significantly less than the previous runs with the shorter wake sheets, this improvement is due mostly to the doubling of the wake sheet length, as one can see from the fact that even in the coarsest meshing, the error has already been cut to 0.92% by the wake sheet extension. Regardless, while increasing panel density shows an improvement, we can see that the remaining errors are still greater than the 0.5% error caused by the small angle approximation, and therefore, some further means of eliminating them should be sought.

This brings up the examination of the effectiveness of elongating of the wake sheet. In the next series of simulations, the number of wake sheet panels was kept nearly constant as the length of the sheet itself was increased. This was done so that any gains in accuracy would be directly attributable to the sheet length alone. The downstream extent

of the wake sheet was varied from x = -0.4 and x = -4.0. The results are reproduced in graphic form below.

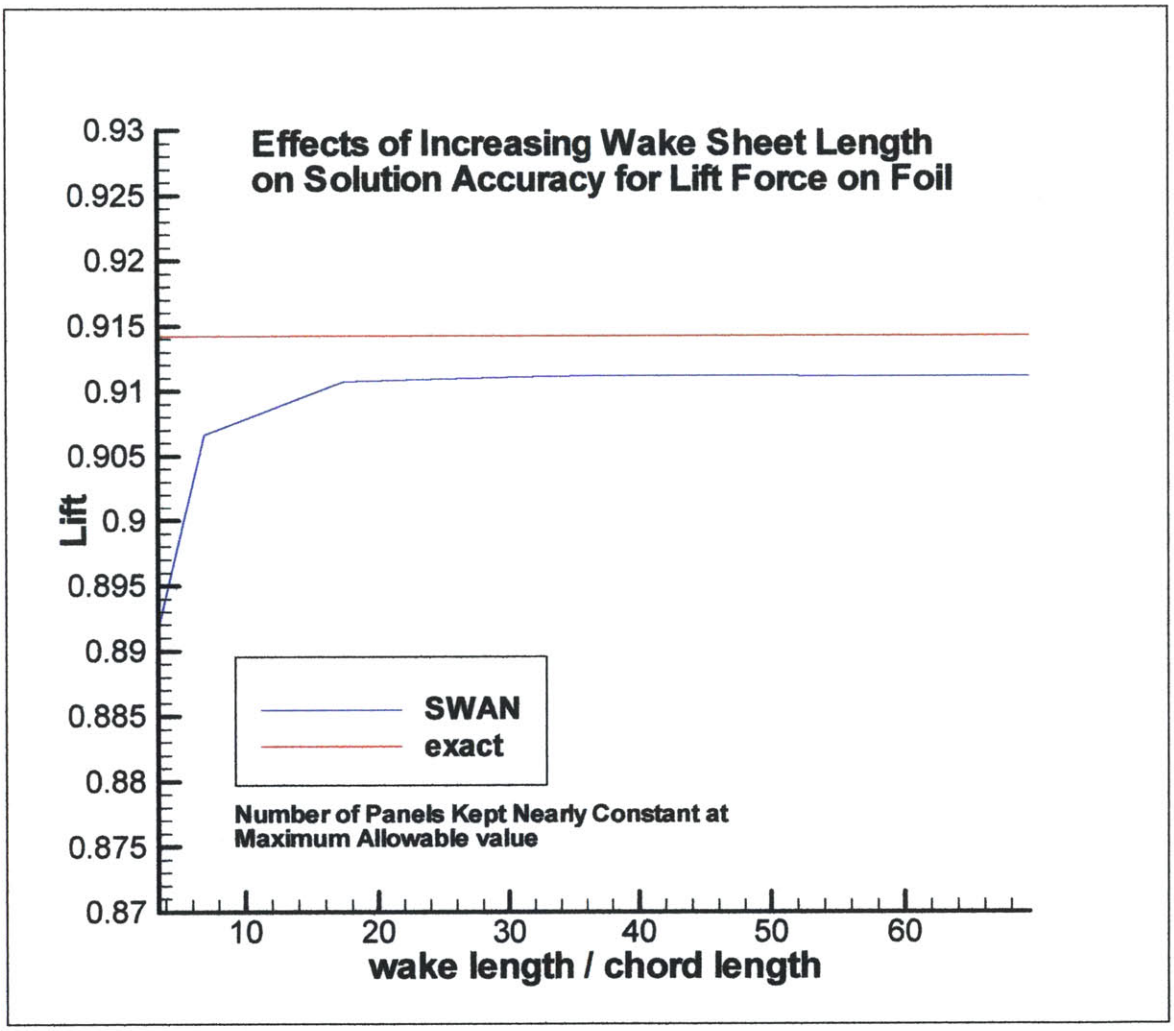

Figure 30

In Figure 30 above we can see a significant increase in the accuracy of the solution. Now the error is cut to 0.3%. Note that this value is less than the error produced by the small angle approximation used to form the lift coefficient formula, equation (28).

We can conclude from these two tests that the length of the wake is the primary factor in ensuring the accuracy of the solution. A wake that is too short will not produce a solution that converges to the exact one.

Interestingly however, the second test shows that increasing the wake length beyond a certain critical value will not increase the accuracy any further. In fact, as the slight drop-off in the results in Figure 30 show, unless the panel density is kept constant, an impossibility given the finite number of panels available, there may actually be a

reduction in accuracy due to the fact that an increase in length will require a decrease in panel density. The plot implies that for a symmetric foil that peak level occurs at around 30 times the chord length.

The question remains, however, with a limited number of panels, what is the best distribution of panels between the foil and wake sheets that will provide the greatest accuracy of the total solution.

A coarsely paneled foil will allow for very dense wake panelization. Conversely, a very densely meshed foil will require coarse wake meshing. The same set of foil simulations was rerun on a foil with variable panel density, with a constant wake length set at approximately 30 times the chord length for maximum accuracy as shown above. The total number of available panels remaining after foil discretization was then used in the wake sheet. The following plot shows the percent error as a function of the ratio of the number of wake panels to the number of foil panels.

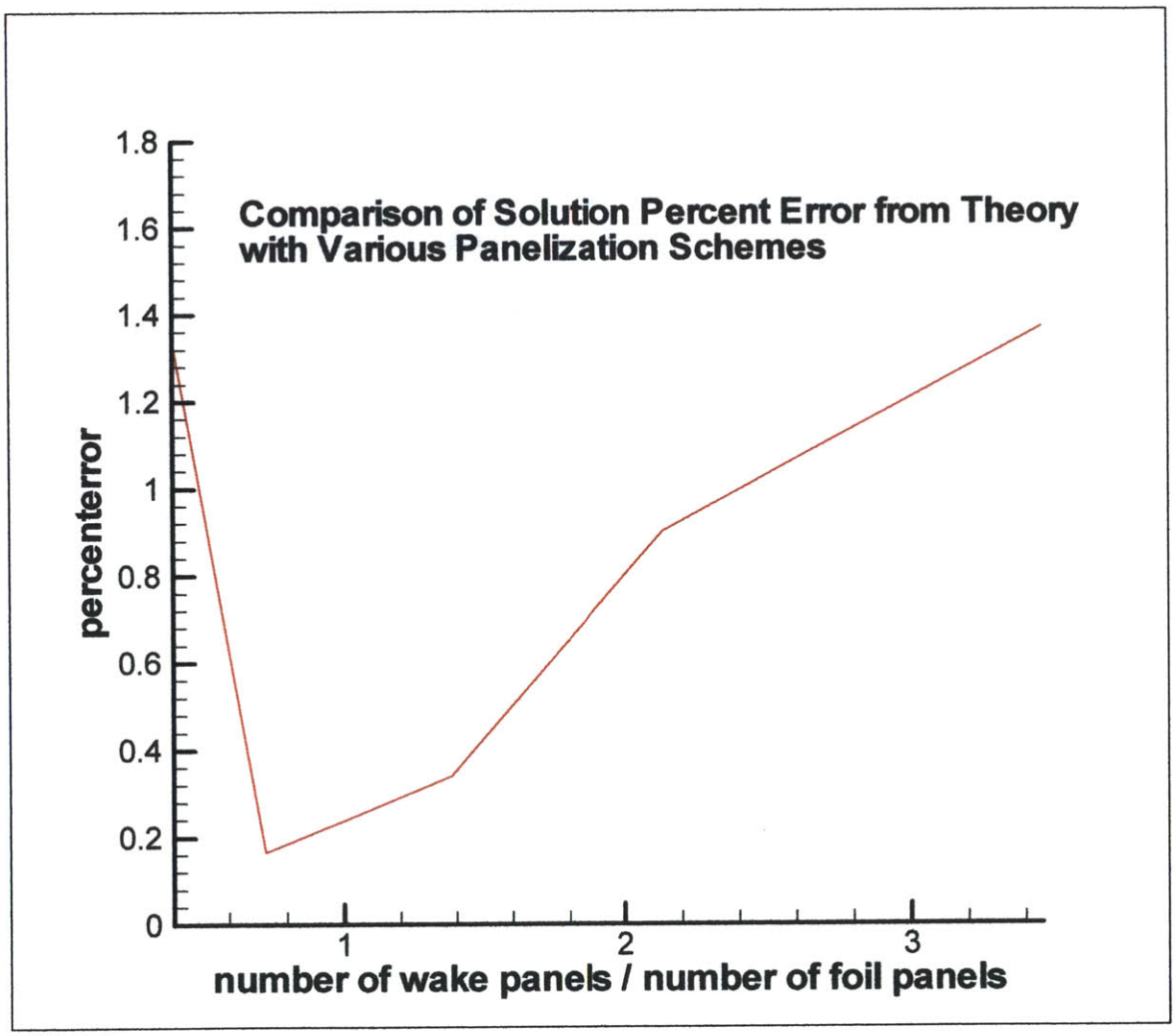

Figure 31

Conclusions from Figure 31 above are that, as a rule of thumb, the number of panels used to mesh the foil should be nearly equal to the number of panels in the wake sheet for greatest solution accuracy.

Further simulations were carried out, using the above findings. The solutions for lift as a function of angle of attack are reproduced below.

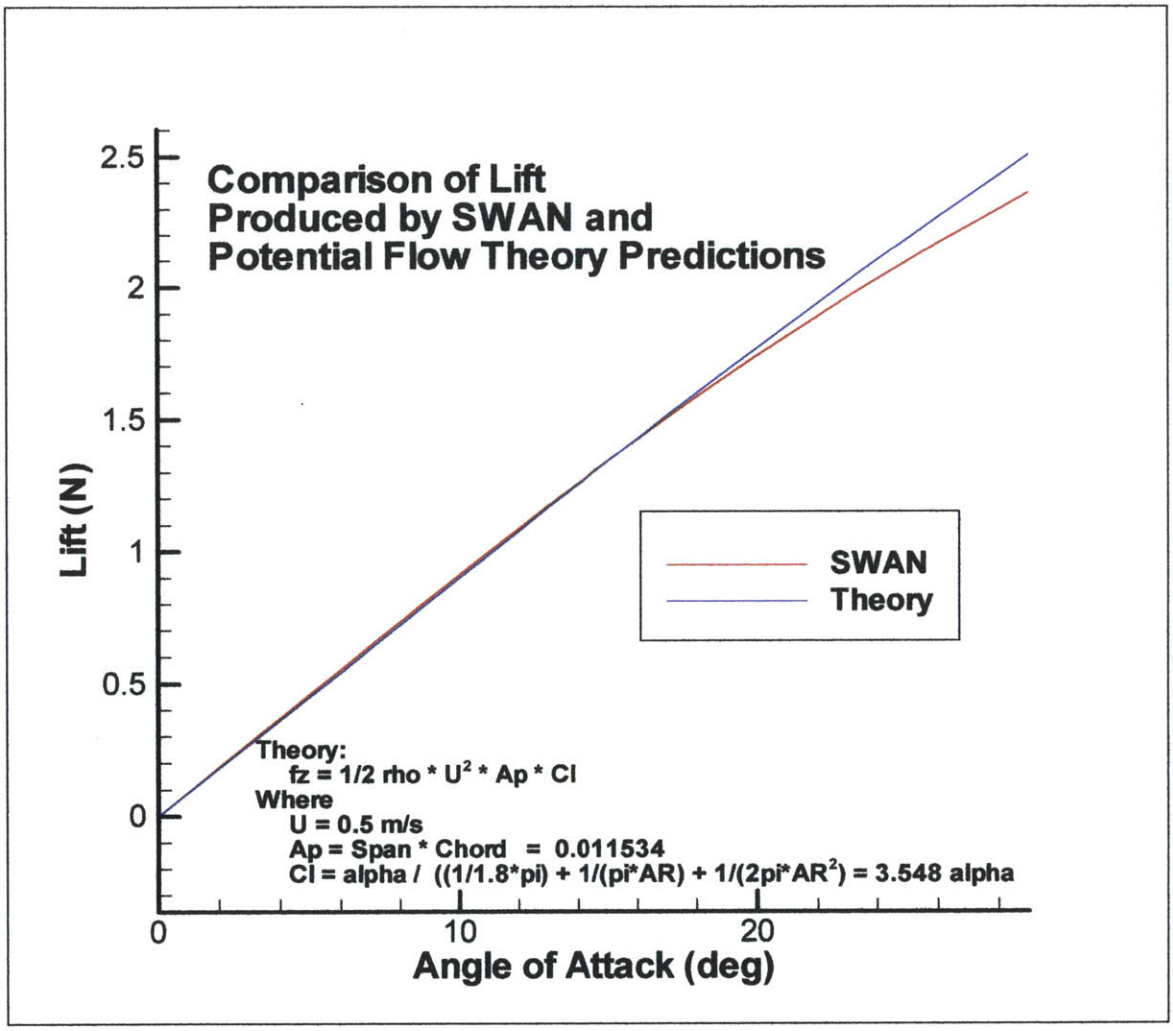

Figure 32

Figure 32 above shows that SWAN provides very good results for hydrodynamic lift across a range of realistic angles of attack.

MOMENT:

The second quantity of interest in foil simulation is the moment generated by the lift. Potential flow theory states that for a two-dimensional foil, the resultant lift force acts at the quarter-chord point. While some variation in these results may be expected due to the three-dimensional nature of our simulations, the results of our SWAN simulations ought to closely approximate this value.

The first step in the analysis of the pitch moment is to eliminate the induced drag related portion of the moment. Because our foil is operating 2m below the surface, the induced drag causes a moment to occur due to this 2m arm. Therefore, this needs to be subtracted out in order to obtain the pure lift related moment.

The plot below contains a graphic representation of this step over the complete range of angles of attack tested.

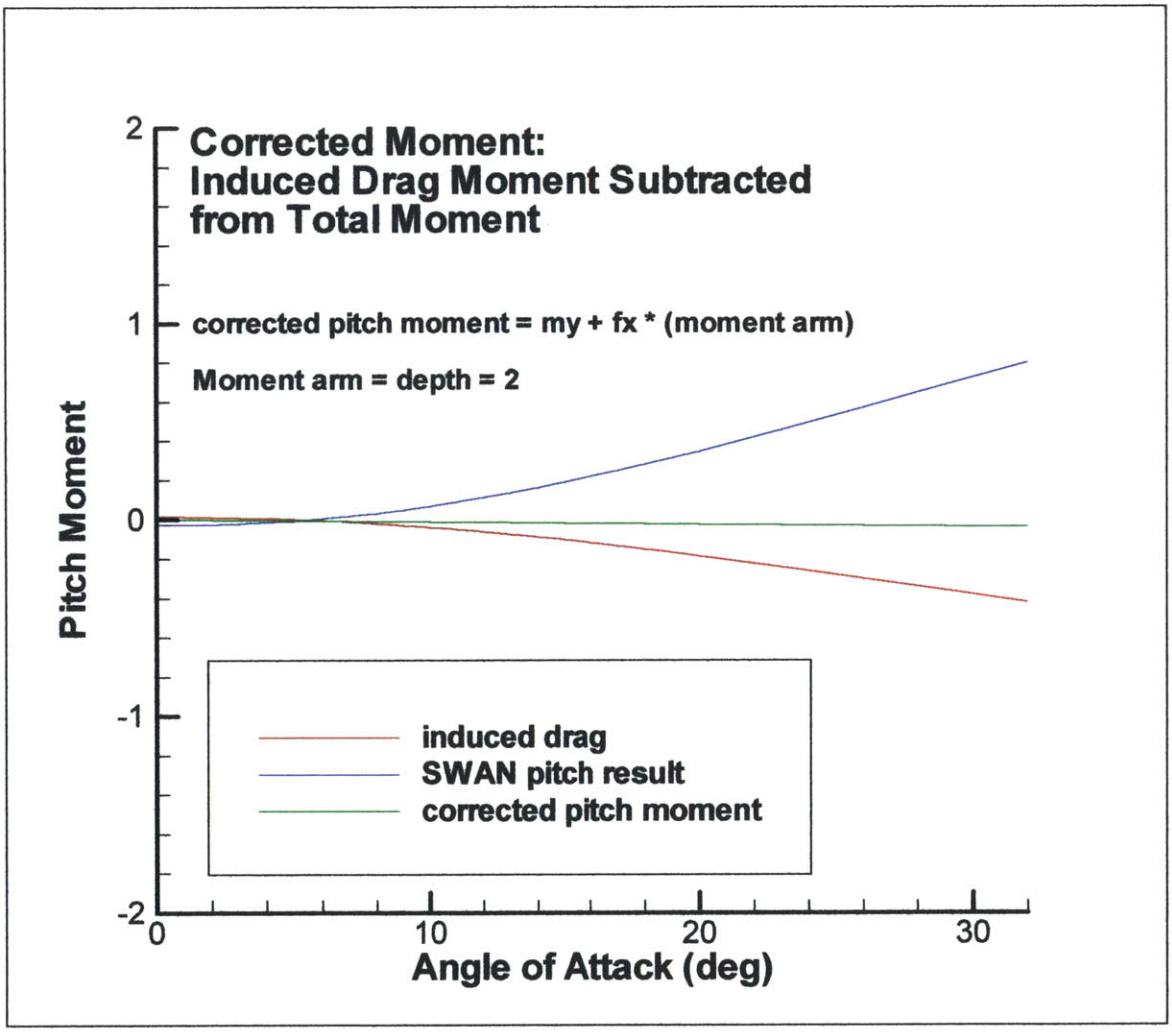

Figure 33

With the corrected moments in hand, an analysis similar to that done above can be undertaken to determine the optimal panel arrangement for accurate prediction of the lift related moment. In this case, however, having determined the optimal arrangement for predictions of lift, we want to eliminate lift errors from our comparison. This is done by comparing the SWAN predicted moment arm with the theoretical moment arm, the quarter-chord point. If we take the predicted moment, subtract the effects of the induced drag and then divide by the predicted lift force, we will generate a value for the predicted moment arm. See equation (29) below.

$$ARM_{SWAN} = \frac{(M_{SWAN} - 2 * DRAG_{SWAN})}{LIFT_{SWAN}} \qquad (29)$$

In this way, the errors in determining lift are eliminated and we are able to focus solely on the moment prediction capabilities of SWAN. The motivation behind this is to be able to compare the optimal panel arrangements for lift and moment predictions separately and then arrive at a compromise arrangement that maximizes the accuracy of both predicted quantities simultaneously. Figure 34 below shows the results of this analysis.

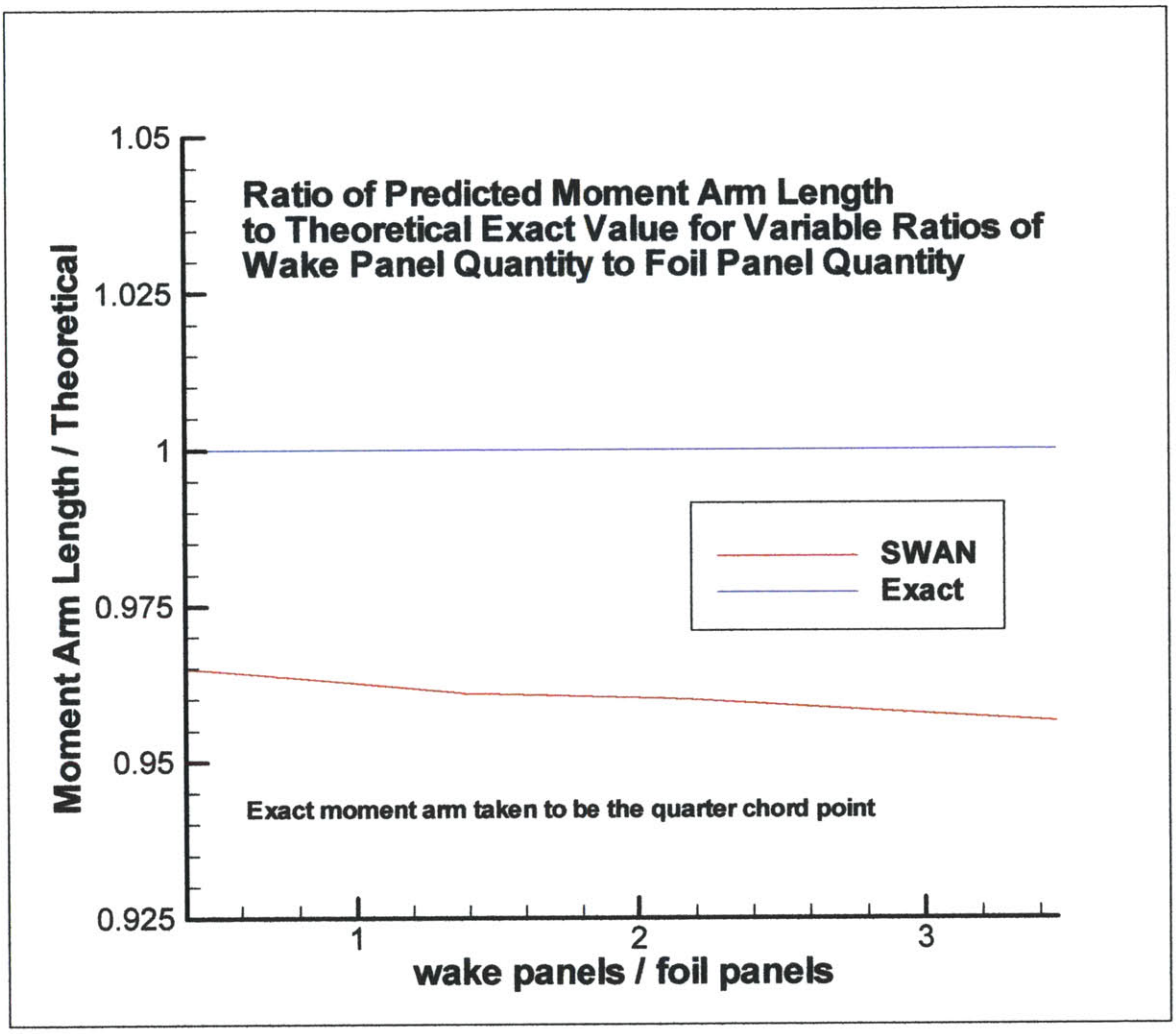

Figure 34

This figure presents results which might have been anticipated, namely, that the accuracy of the moment arm length prediction increases as foil surface panel density increases. More importantly, it shows that our original optimal arrangement of panels, with an equal number of panels on both the foil and the wake sheets, is still an acceptable arrangement for moment arm prediction. Given an unlimited number of panels, the theoretical value will be achieved.

With these results in mind, a 15 x 30 panel foil was run at a variety of angles of attack and the predicted moment observed. Figure 35 below shows the results of these simulations.

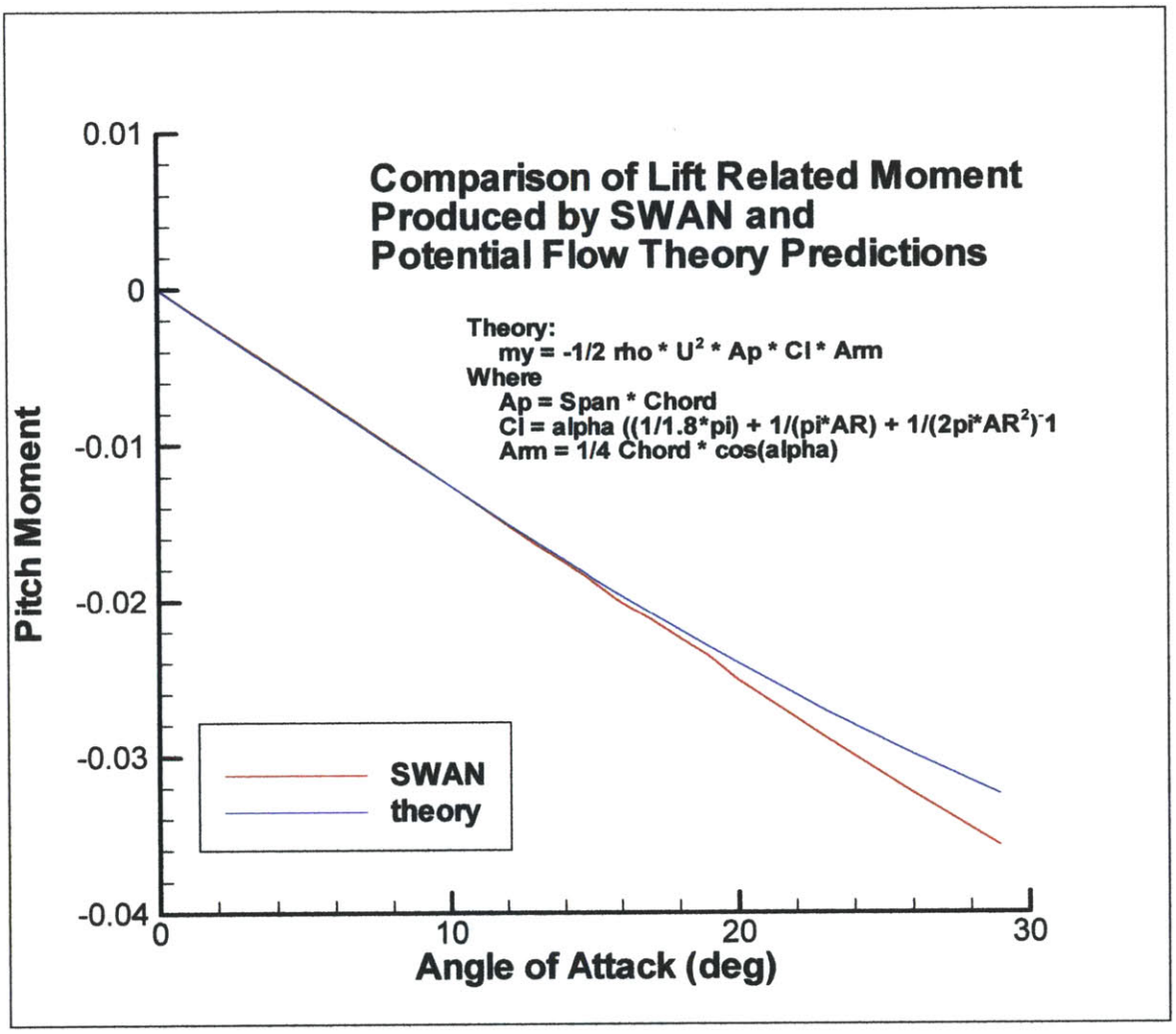

Figure 35

Again we see very good agreement between SWAN and potential flow theory for realistic angles of attack.

INDUCED DRAG:

The next step in the lifting surface analysis is the examination of induced drag. Hoerner writes that "Theory indicates that the optimum lift distribution over the span of a wing…is elliptical." As most discussions of induced drag tend to focus on this elliptical plan form, we will begin our examination there as well, simply noting for the time being that some adjustment will eventually have to be made for the rectangular plan form eventually used in the SWAN simulations.

Taking our geometry as below in Figure 36 and assuming the elliptical plan form,

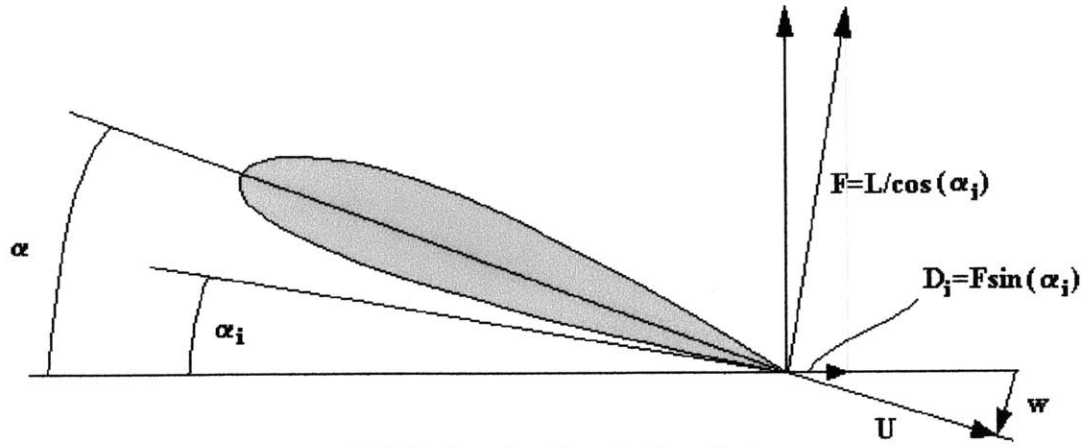

Induced Drag on a Foil Undergoing Steady Translation

Figure 36

Hoerner notes that the volume of fluid displaced by the wing is contained within a cylinder with a diameter equal to the span of the foil, S. From this, we note that the mass per unit length of the liquid deflected by the wing can be expressed as:

$$M_f = \rho\pi S^2 \qquad (30)$$

Hoerner then applies "force equal to mass times added velocity" to produce

$$L = \rho\pi S^2 U w, \qquad (31)$$

with w indicating the vertical downwash velocity at some distance downstream of the foil. He concludes that the average downwash angle is then

$$\frac{w}{U} = 2\frac{C_L}{\pi A} = 2\alpha_i \qquad (32)$$

where α_i is the induced angle of attack. Therefore,

$$\frac{C_L}{\pi A} = \alpha_i \qquad (33)$$

The result of this is that the angle of attack is effectively decreased and the lift force acts in a direction perpendicular to α_i instead of α and therefore, an induced drag force results. That drag force can be described as

$$C_{Di} = C_L \tan(\alpha_i) = \frac{C_L^2}{\pi A} \qquad (34)$$

using small angle approximations.

As mentioned above, this formula needs to be adjusted slightly to reflect the fact that we will not actually be dealing with an elliptical plan form in subsequent SWAN simulations. Hoerner suggests the use of an equivalent aspect ratio to accomplish this using the equation

$$C_{Di} = \frac{C_L^2}{\pi e A},$$

where eA represents the equivalent aspect ratio. He then states that Glauert actually computes the lift and drag curve slope values for rectangular plan forms of variable aspect ratios.

The first aspect of the Glauert material which must be understood is that he uses a lift formula of

$$L = C_L \rho A_p U^2 \qquad (35)$$

rather than the more conventional

$$L = C_L \frac{1}{2} \rho A_p U^2 \qquad (36)$$

used currently. Similarly, in discussions of drag, Glauert uses the formula

$$D = C_{Di} \rho A_p U^2 \qquad (37)$$

This difference in approach must be kept in mind when dealing with Glauert's formulas.

Going directly to Glauert's formula for the drag coefficient, we see

$$C_{Di} = \frac{2}{\pi A}(1+\delta)C_L^2 \qquad (38)$$

Glauert includes a table of results for the quantity delta, reproduced in part below.

A/a_o	δ
0.5	0.007
1.0	0.019

1.5	0.034

Here, a_0 is the theoretical value of the two dimensional lift curve slope which, in Glauert's regime is equal to π. Therefore, $A/a_0 = 1.1$ and δ can be interpolated as

$$\delta = 0.022$$

Avoiding the temptation to insert this value into the Hoerner formula, we instead continue with Glauert's equation (38) for consistency, and derive a value for the drag coefficient.

$$C_{Di} = 0.1875C_L^2 \qquad (39)$$

The lift coefficient can be obtained from our previous calculations of the theoretical value for lift (equation (28)). Substituting this in Glauert's formula for lift, equation (35), we get

$$L = 5.2387\alpha = C_L \rho A_p U^2 \Rightarrow C_L = 1.775\alpha \qquad (40)$$

and therefore

$$C_{Di} = 0.591\alpha^2 \qquad (41)$$

Finally, theoretical induced drag can be calculated again using Glauert's equation (37).

$$D = C_{Di} \rho U^2 A_p = 1.744\alpha^2 \qquad (42)$$

From this formula we can once again return to our test series and examine convergence of the SWAN results with theory. We again look at the case of an angle of attack equal to 10 degrees and an associated theoretical induced drag force of 0.0531, with foil panelizations ranging from 10 x 20 to 20 x 40. Due to our previous findings, the wake sheet was set to extend to the line x = -2.0 and all panels available after the meshing of the foil were used in the wake. The results of those simulations are reproduced below.

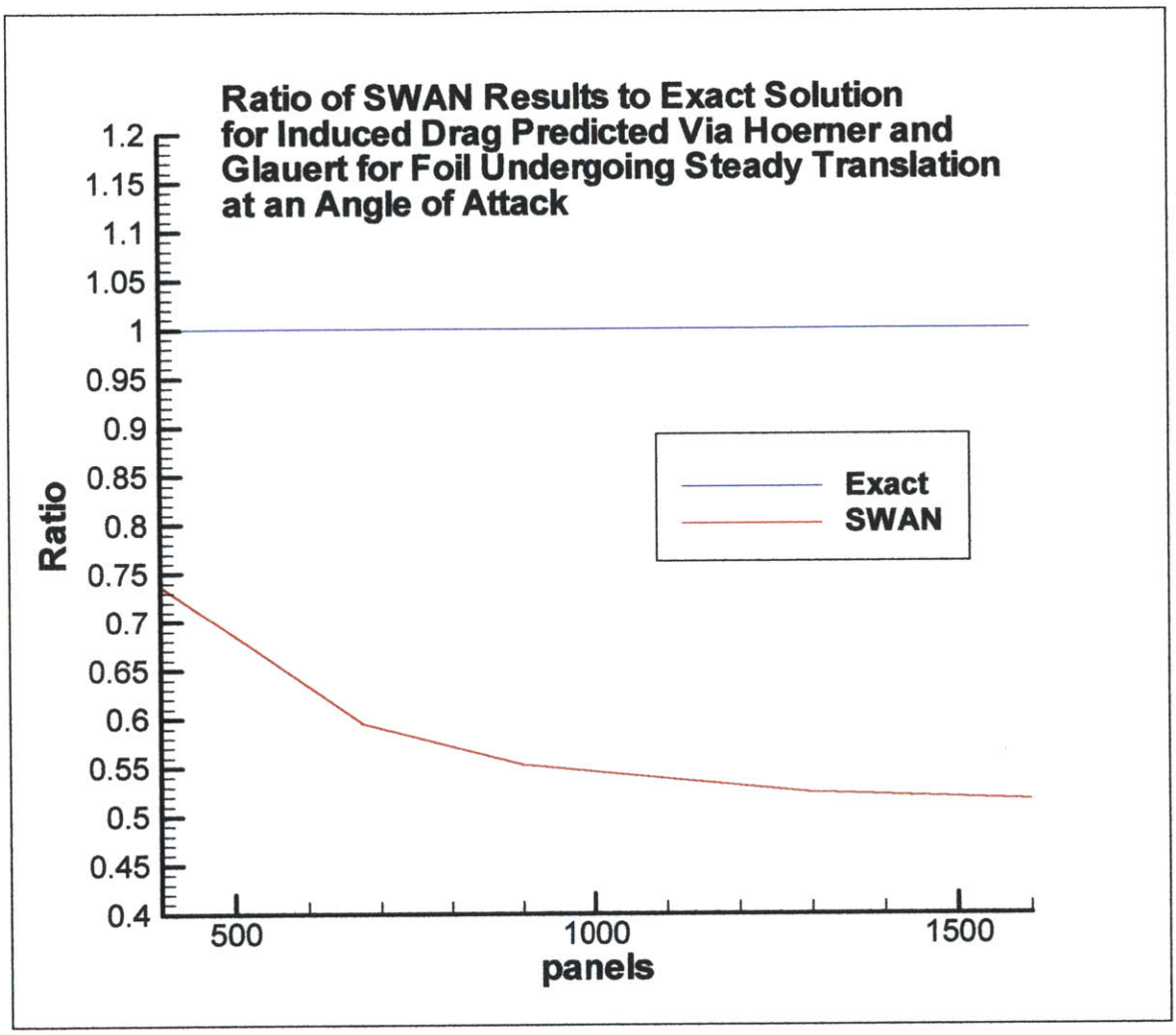

Figure 37

Once again, we see the results of the preliminary tests converging on some value with increasing foil panel density. Unfortunately, that value is significantly distant from the predicted one. In order to determine an effective method of increasing accuracy, we again turn to the 15 x 30 panel simulations to examine the effects of independently increasing wake panel density and wake length. The results for the variable panel density are reproduced below.

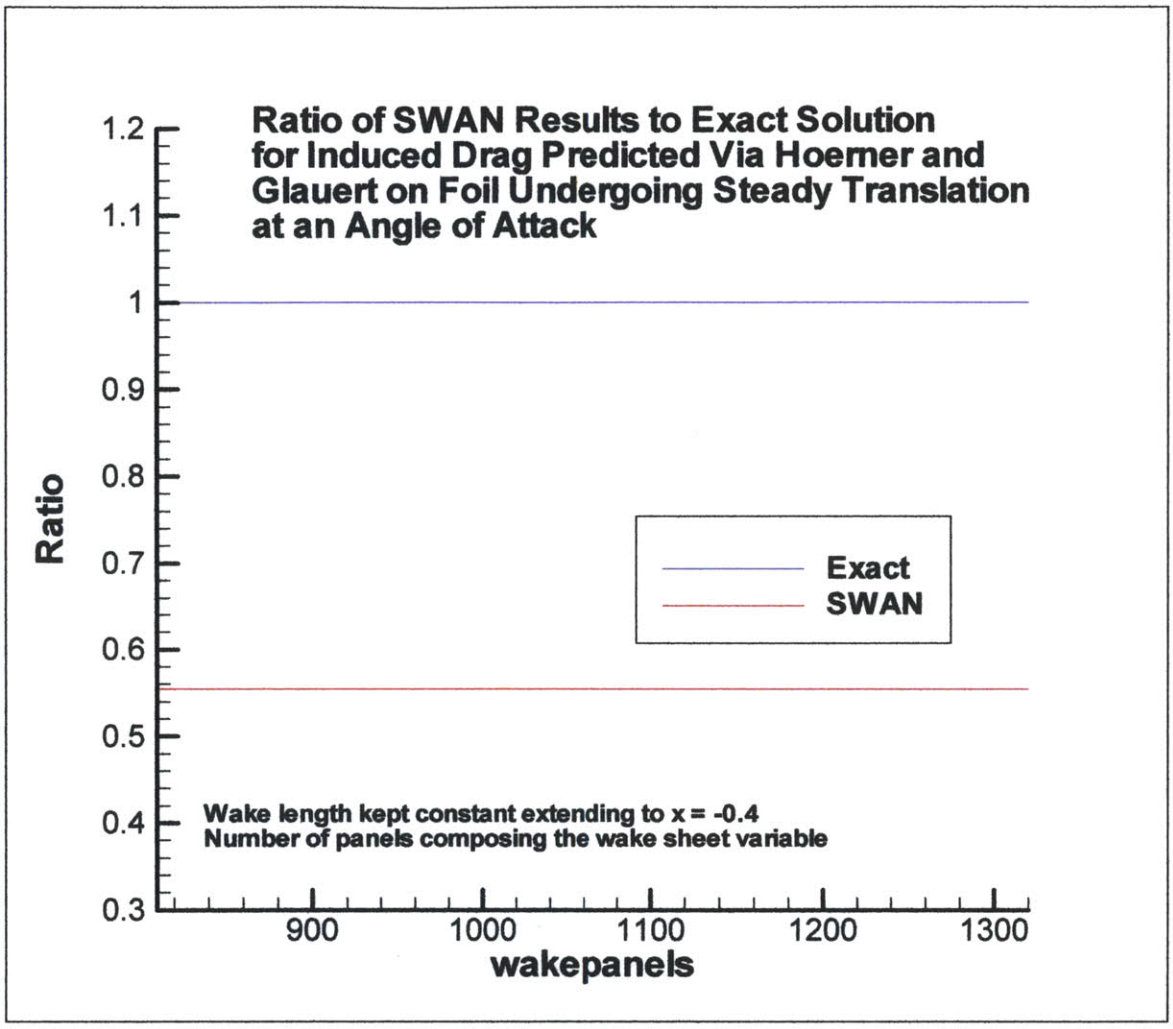

Figure 38

Clearly, the plot above shows that increasing wake sheet panel density has virtually no effect on the accuracy of the solution. The values shown are essentially constant and equal to the original value for the 15 x 30 foil calculated in the previous runs. The next attempt, as with the lift analysis, maintained wake panel density and increased the length of the wake sheet. The results obtained are reproduced below.

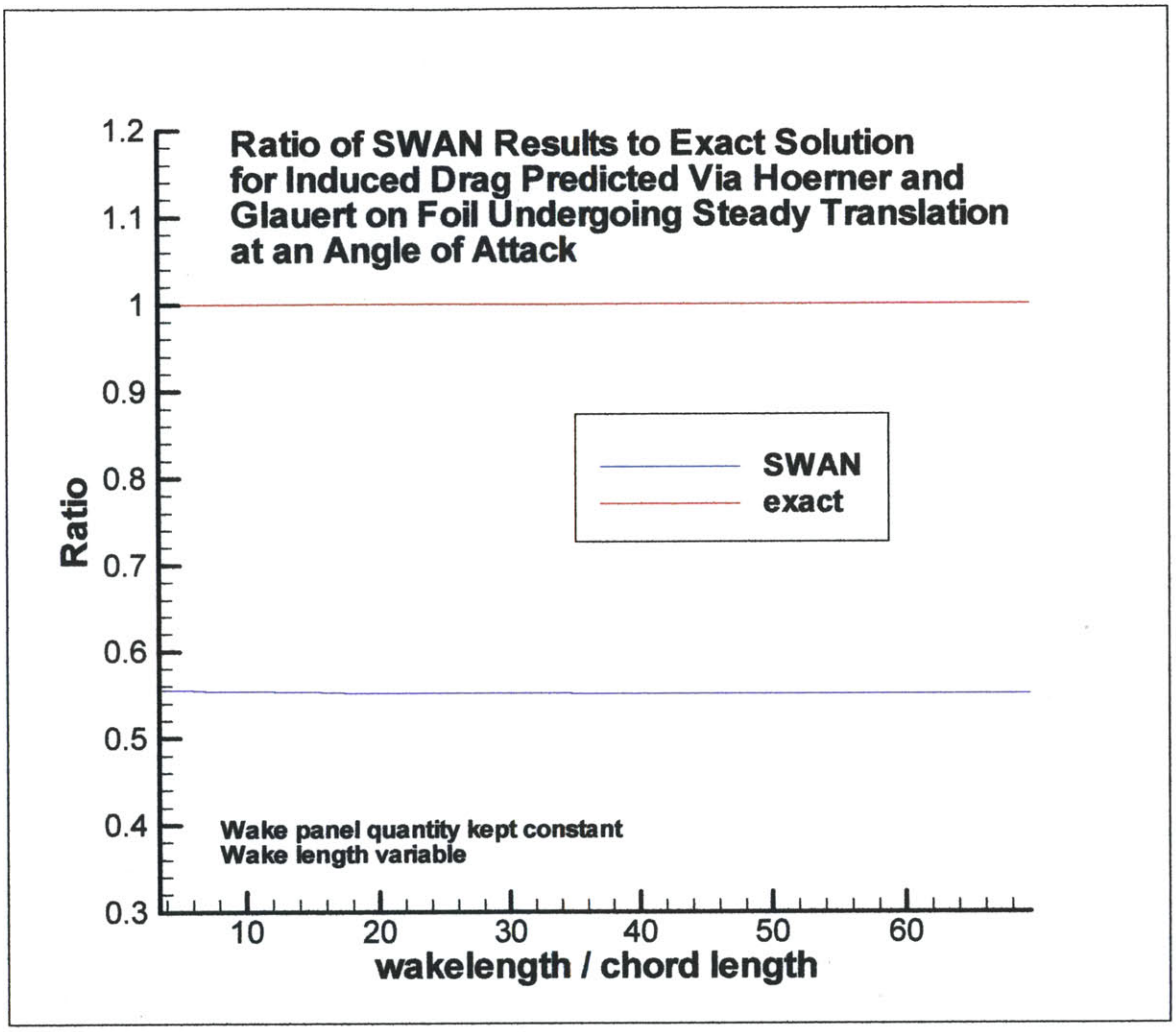

Figure 39

Now it is clear that the length of the wake has little to no impact on the induced drag. Having eliminated wake related sources of error, we conclude that the critical factor in producing accurate results for induced drag is the density of the foil panelization itself. Unfortunately, previous simulations have shown that increased foil panel density produces convergence to an inaccurate answer.

In order to gain some more insight into the nature of this error, I tried to ascertain how the error varies with the angle of attack. A series of simulations was done, again on the 15 x 30 panel foil with wake sheet extending to x = -2.0 downstream. Figure 40 below shows a comparison of theoretical results and the SWAN output.

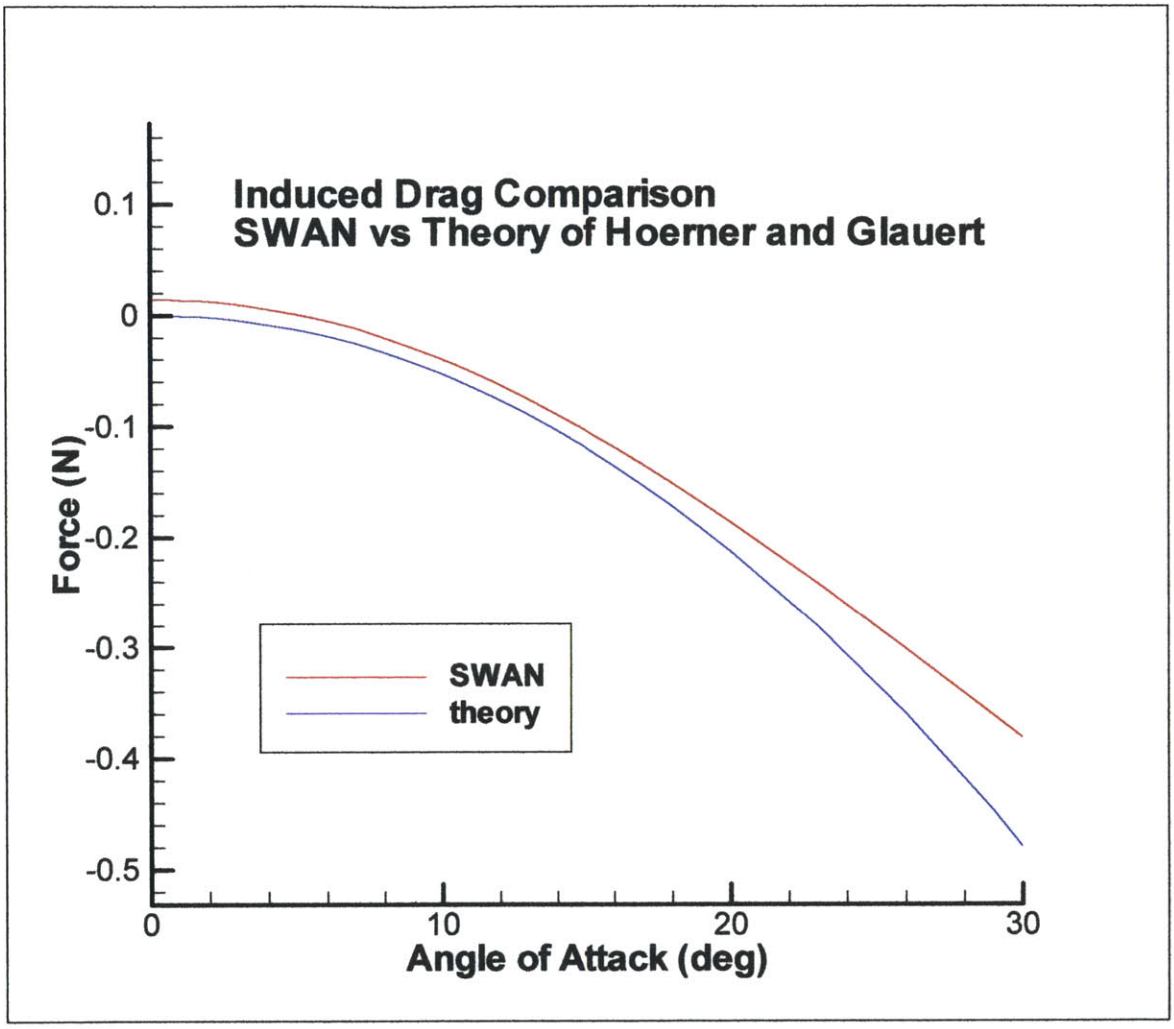

Figure 40

Interestingly, the plot above seems to show a virtually constant offset between the SWAN results and theory. More interestingly, that offset occurs even at zero angle of attack.

This serves to underline a fairly serious error in the SWAN results, namely, the non-zero drag force present at zero angle of attack. Several different panelization strategies were employed in an attempt to eliminate this error, including a single, wraparound sheet and sheets that connected at the outboard ends of the foil. None were successful, and all produced a similar output quantity.

All of these attempts, however, were done prior to the adjustments of the SWAN SETUP routine that were done in order to correct for inaccurate Munk moment results. After these adjustments had been made, the following plot of induced drag was produced.

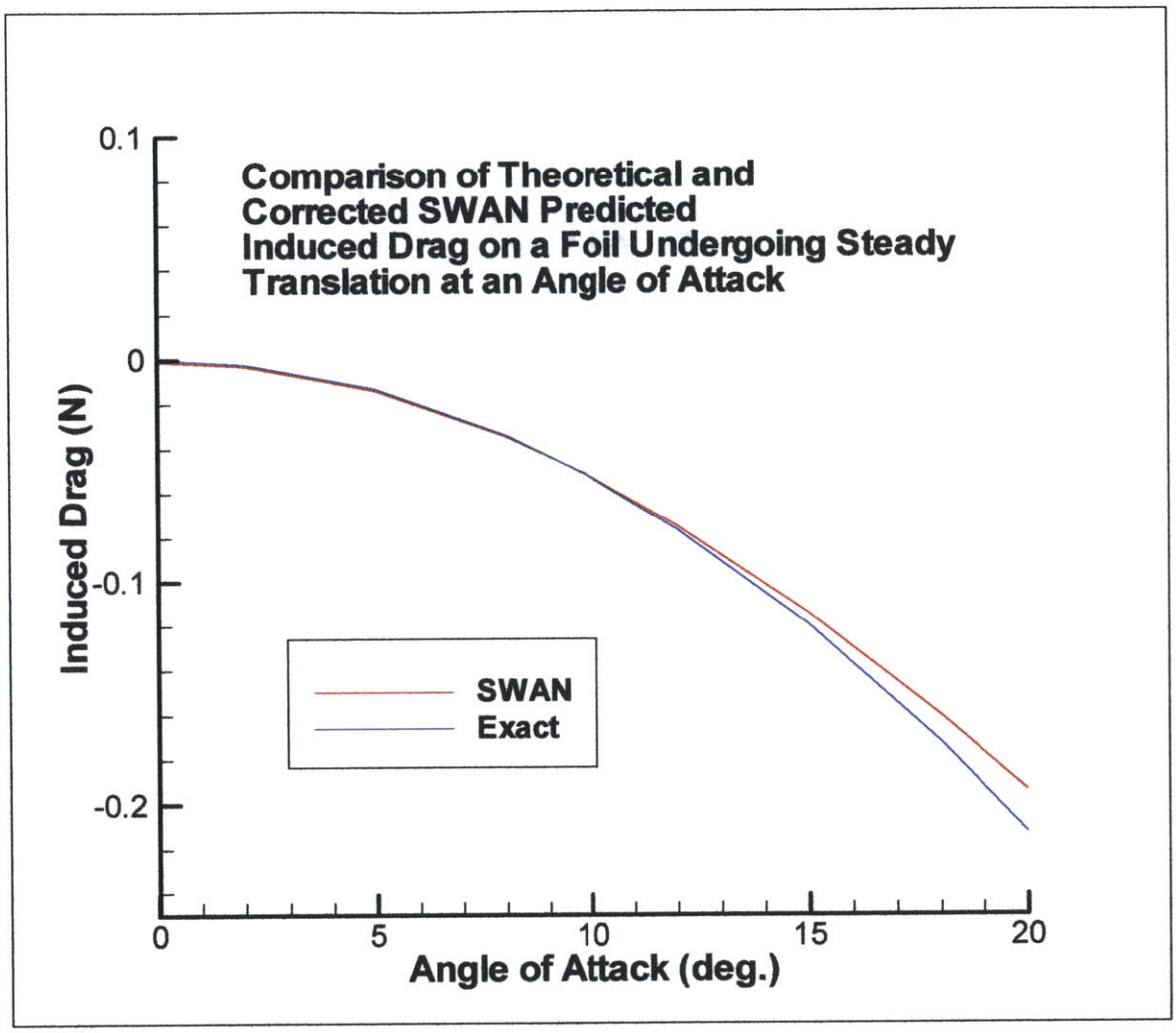

Figure 41

Note that now we see very good accuracy in the SWAN results up to about 20 degrees. So, we conclude that the source of both errors was the same.

As a check, to ensure that the adjusted SWAN still produces good values for lift, the same foil was run through the same range of angles of attack. The following plot was produced.

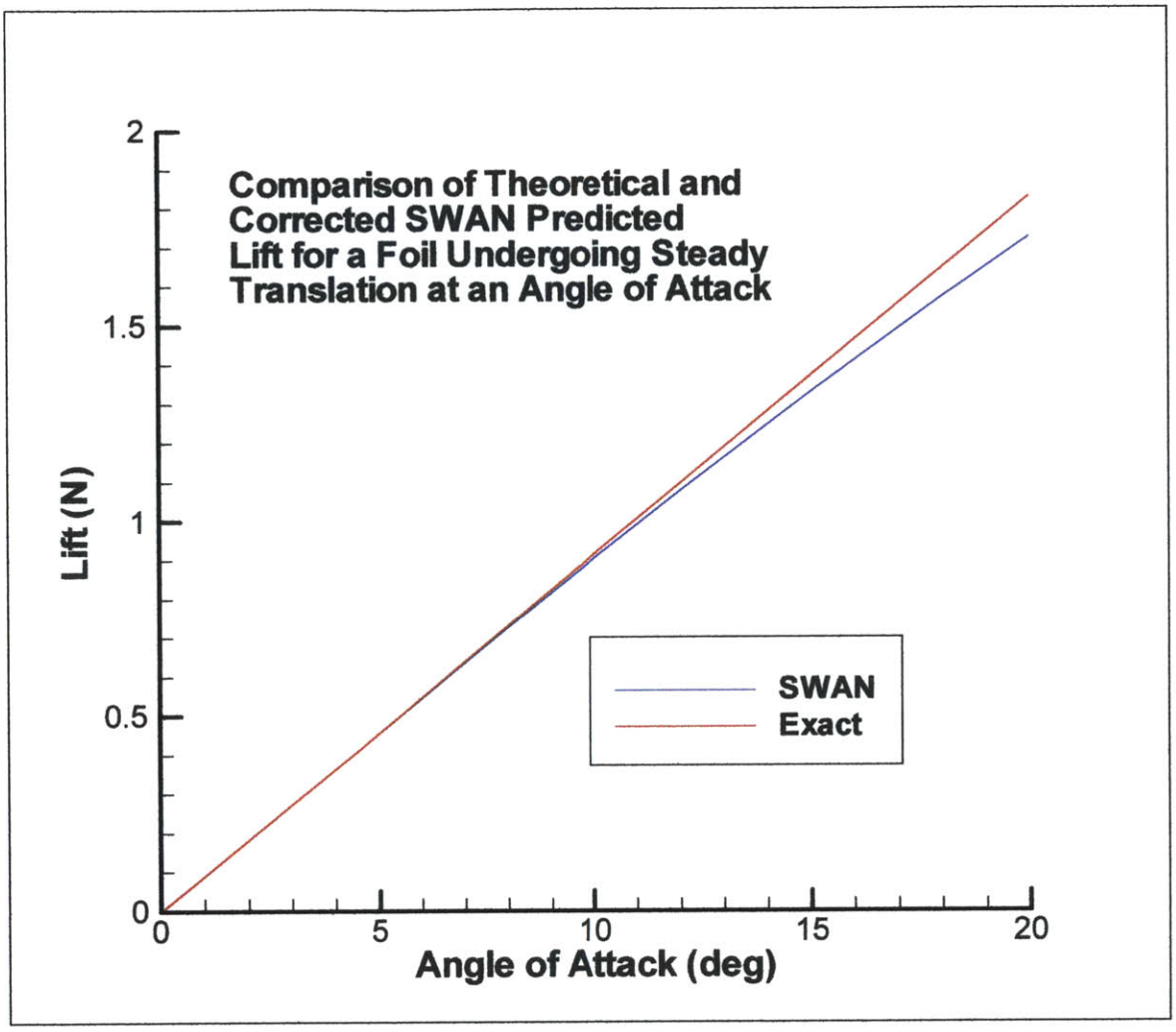

Figure 42

Clearly, the adjustments did not effect the lift values, as they are just as accurate as those produced previously.

To close out this discussion of symmetric foil shapes, I will note only that all of the other values that should be nearly zero are, in fact, equal to or close to zero as the following table illustrates.

Number of Panels	Sway Force	Roll Moment	Yaw Moment
400	0	$-1.5 * 10^{-7}$	$-5 * 10^{-9}$
676	0	$-3.6 * 10^{-7}$	$9.5 * 10^{-9}$
900	0	-1.25 * 10-7	$2.04 * 10^{-8}$
1296	0	$2.21 * 10^{-7}$	$1.16 * 10^{-7}$
1600	0	$-2.25 * 10^{-7}$	$9.5 * 10^{-8}$

A plot of the 15 x 30 meshing is included to illustrate the geometry in question. In it, one can clearly see the two-sheet meshing on the foil as well as the trailing wake sheet.

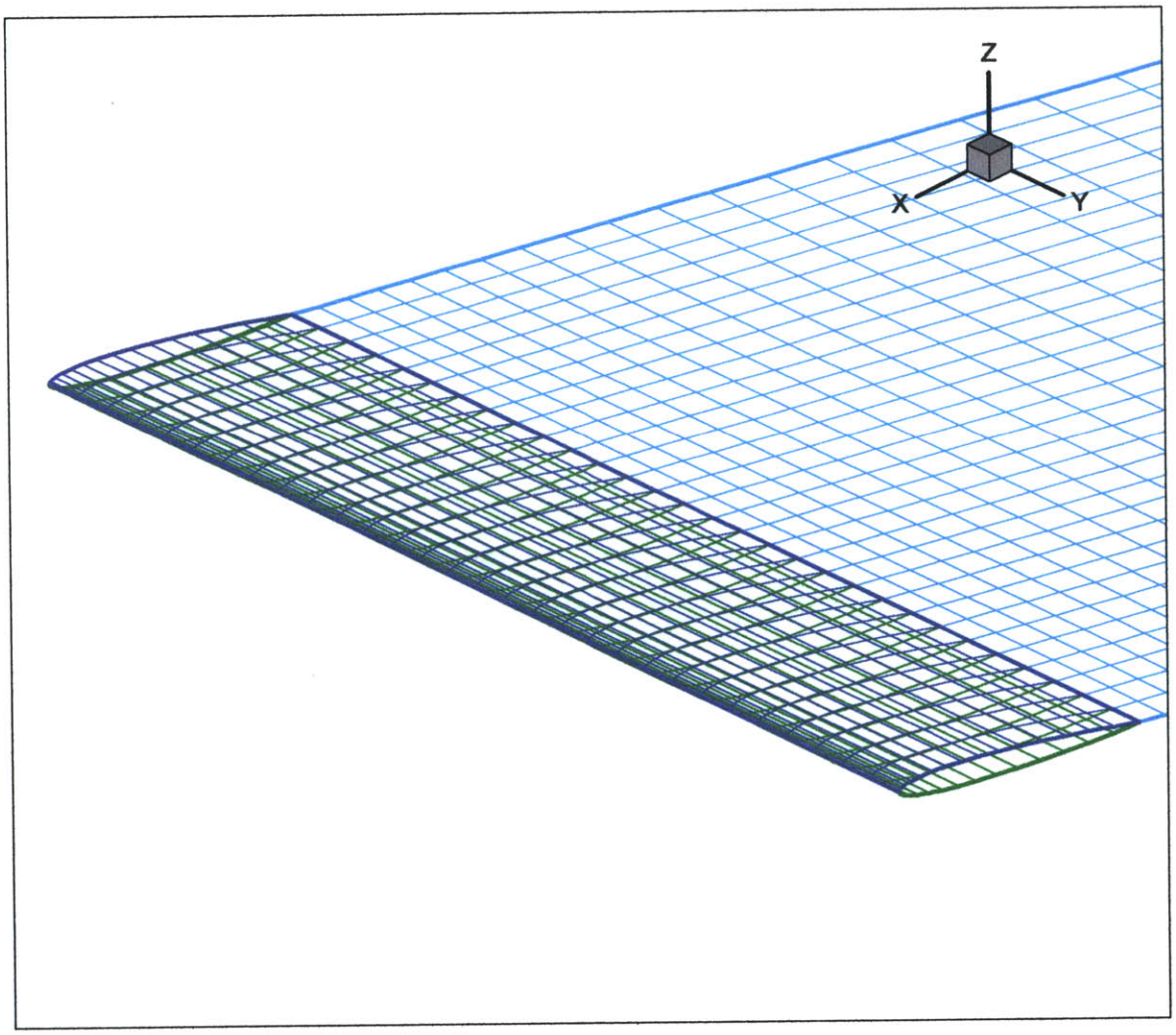

Figure 43

To conclude, the corrected SWAN produces very good results for lift, moment and drag on a foil undergoing steady translation at an angle of attack.

ASYMMETRIC (CAMBERED) FOILS

A brief examination of cambered foils was made in order to assess SWAN's abilities in the absence of foil symmetry. Newman states that "the simplest possibility is a parabolic arc mean camber line with slope"

$$\frac{d\eta}{dx} = \alpha - \beta x$$

where α is the angle of attack relative to the straight line connecting the leading and training edges and β describes the maximum camber height by

$$\eta_{max} = \frac{\beta c^2}{8}.$$

Under these conditions, Newman states that the lift coefficient will be

$$C_L = \frac{1}{2}\pi\beta c$$

and the moment coefficient will be

$$C_M = 0$$

implying that a parabolic arc mean camber line produces no additional moment. While these formulas apply only to two dimensional or hypothetically infinite span three dimensional foil shapes, some generalizations can be made in order to apply them to a finite length three-dimensional flow.

First, we can state that even with the three-dimensional nature of our flow, the zero moment coefficient implies that there should probably be no additional moment beyond that encountered in the uncambered foil simulations. Second, having calculated the lift for the finite length, symmetric foil to be only 11.3% of the theoretical two-dimensional value, we might expect, qualitatively, that the values produced by SWAN in the three dimensional, cambered case, with equal aspect ratio as used previously, would be a similar percentage of the two dimensional theoretical value.

In the following simulations, the same geometry was used for the foil as in the symmetric case except that a parabolic camber was introduced as illustrated below

Cambered Foil
Midheight = .0025

Figure 44

Note that a mid-height of 0.0025m was used above for clarity while a value of 0.00125m was used in subsequent simulations.

First, we will check the zero additional moment prediction. SWAN simulations were run through a range of angles of attack and the pitch moment, corrected as before, is compared with the uncambered moment obtained previously. The difference between the two values is plotted below.

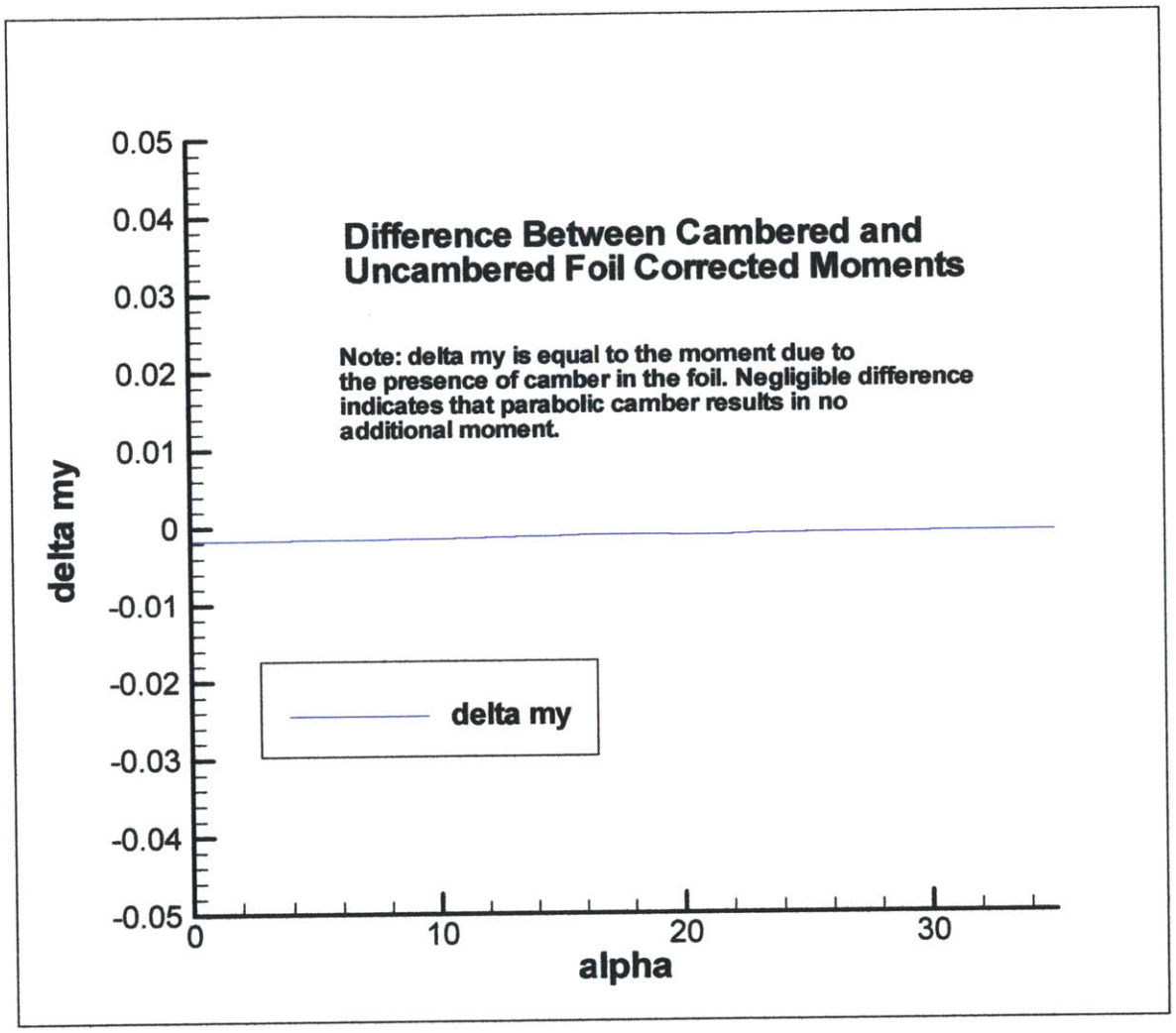

Figure 45

Clearly, there is minimal pitch moment caused by the addition of the camber, with the nearly constant result being on the order of 3% of the uncambered pitch moment at 10 degrees angle of attack.

Next, we turn our attention to lift. With the camber-related lift coefficient dependent only on the geometry of the foil, we expect to see a nearly constant value for camber-generated lift over a range of angles of attack. If we assume that this value is equal to the lift generated at zero angle of attack and subtract it from the total lift on the cambered foil, should recover a lift curve identical to the uncambered case. Doing this, we observe the following results.

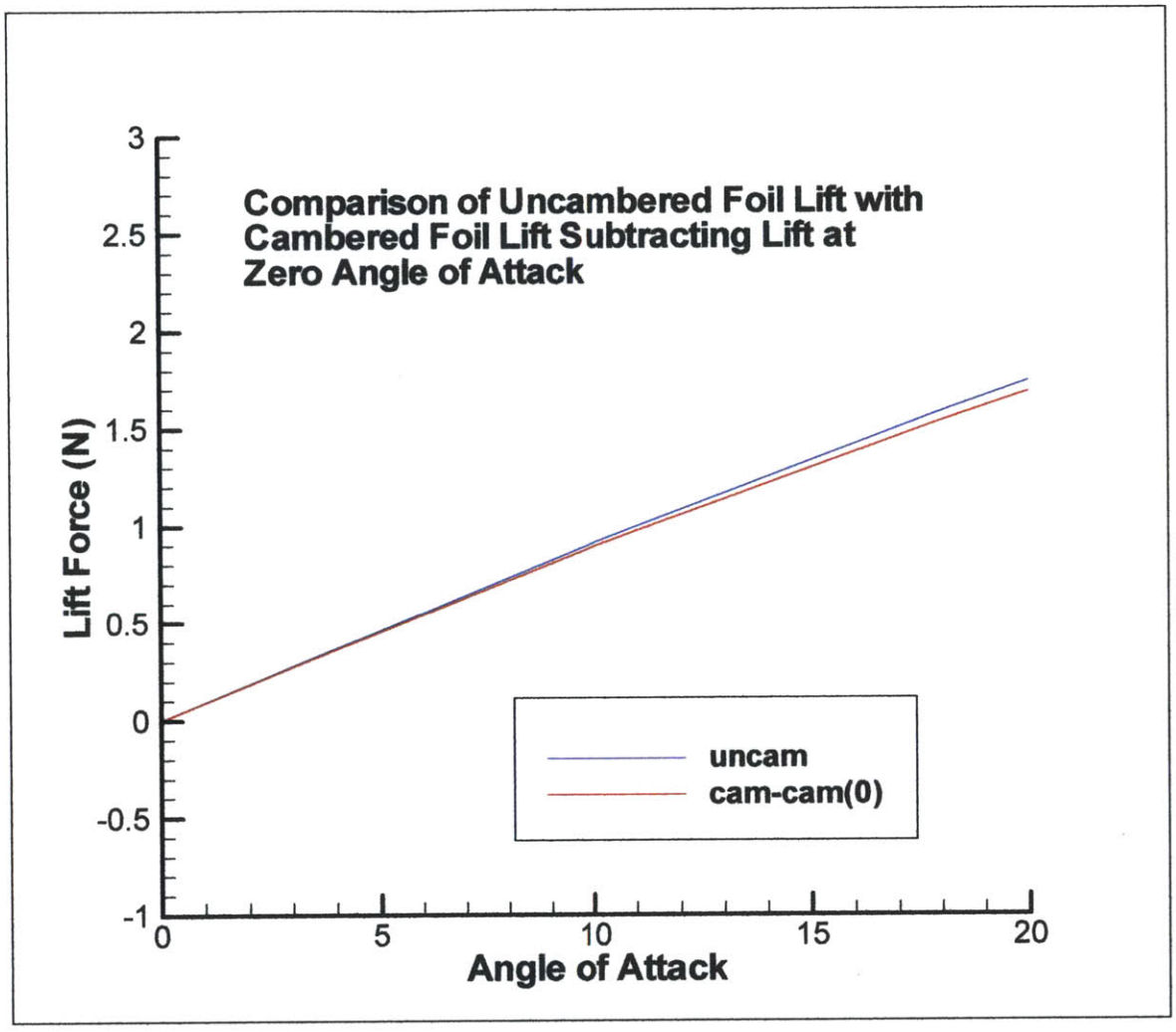

Figure 46

Here, from the proximity of the two solutions, we can conclude that SWAN's results are correctly predicting that camber-related lift is nearly constant and therefore independent of angle of attack Indeed, the increasing difference between the two solutions is an indication that the flow becomes more three-dimensional in nature as angle of attack increases and therefore the accuracy of the two-dimensional approximation decreases.

Finally, we look to the prediction that our total lift force can be described as a percentage of the two-dimensional lift force. Taking our lift coefficient to be

$$C_L = 2\pi\alpha + \frac{1}{2}\pi\beta c$$

and using the assumption that the three dimensional percentage of lift generated will be similar to previous results, 11.3% of the two-dimensional value, we obtain the lift formula

$$L = .113C_L \frac{1}{2}\rho U^2 c = .8338C_L$$

Comparing the results of this theoretical lift to that generated by SWAN, we get the following plot:

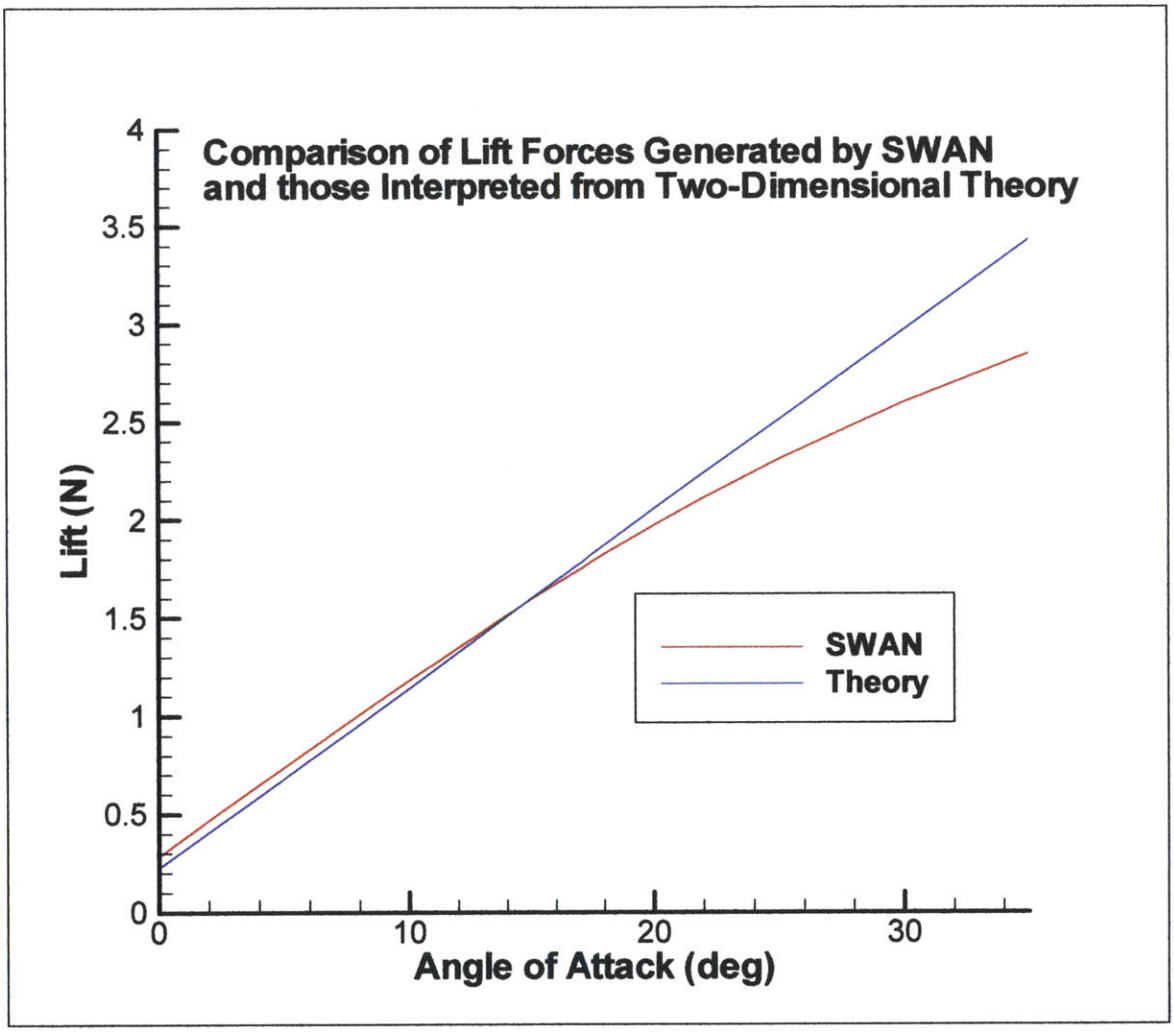

Figure 47

Two things can be inferred from these results. First, we see pretty good agreement between SWAN and the predicted values, especially so since those predicted values are somewhat suspect in their origin. Secondly, the similar slope of these lines towards the

origin indicates that it is the constant valued camber-related lift causing the error. If perhaps the cambered foil converges on its two-dimensional solution faster that the uncambered foil, that would explain the above discrepancies. Admittedly, however, I note that we are now trying to fit theory to SWAN rather than the reverse, a practice of questionable value at best.

To conclude this discussion of cambered foils, I believe we see qualitatively reasonable results from SWAN for the preceding simulations. All values expected to be zero are quite close including the drag force at zero angle of attack. Additionally, lift and moment calculations tend to give qualitatively correct answers.

COMPOSITE FORMS:

Having verified the accuracy of the SWAN output for a variety of simple geometries, the next step in the simulation is to combine these shapes into composite forms and evaluate the response.

The first composite form of interest is a foil and bulb combination reminiscent of a racing yacht keel. The foil shape is almost identical to those tested in previous simulations, with a variable density, two panel meshing scheme. A slight change, however, was necessitated by the now critical limit to the available panels. The wetted foil span was halved to 0.1. This enables us to better assess convergence by freeing up a number of panels which can then be used to increase the panel density on the remaining half of the foil.

This change does not necessarily lessen the applicability of the following results to longer foil lengths, however. The difficulty in modeling this flow is due almost entirely to the foil-bulb juncture and is largely unaffected by the length of the foil itself. Indeed, at a distance of 0.1m from the bulb surface, the flow over the foil seems virtually unaffected by the presence of the bulb. As a result, assuming that convergence is shown below, one could either extrapolate full length results or, given an adequate number of panels, simulate them directly.

Two configurations were tested for convergence. First, the foil and the bulb were merely constructed in such a way as to make them butt up against each other at the foil-bulb juncture as seen in Figure 48 below.

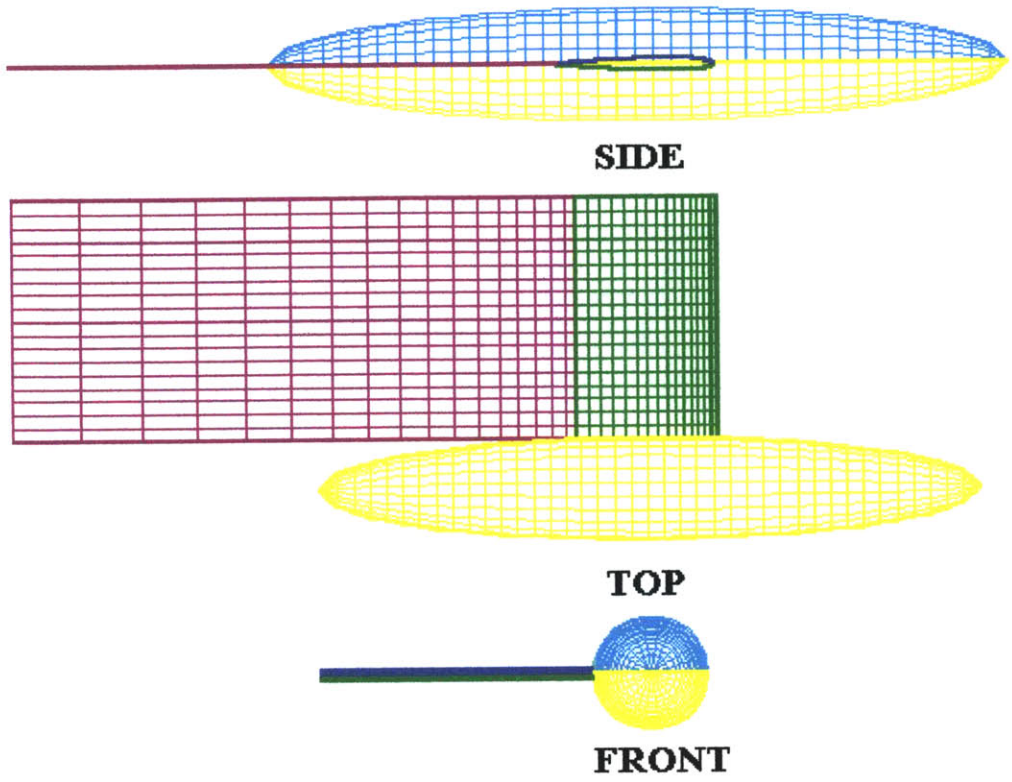

Figure 48

The second geometry had the foil extend inside the bulb to the axis of symmetry. The goal behind this was to then be able to extend the wake sheet through the aft end of the bulb and potentially capture a more accurate simulation of the flow. This geometry is depicted below in Figure 49.

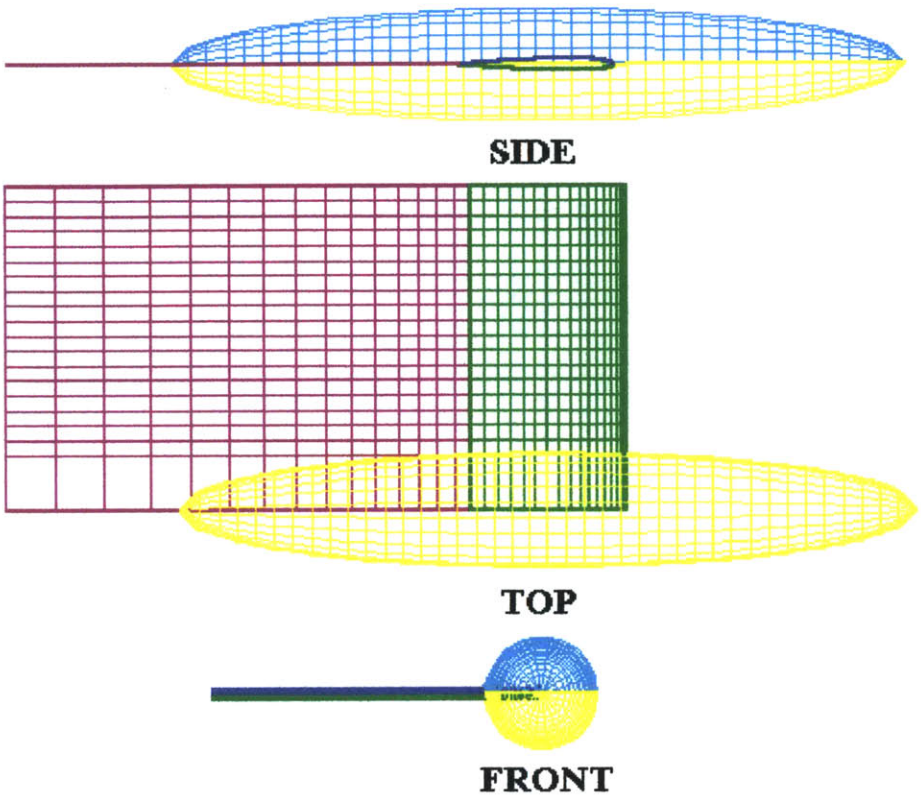

Figure 49

Note that in both of these geometries the first row of foil panels conforms exactly to the side of the bulb. Also note that in the second geometry, the rows of bulb panels directly adjacent to the foil conform exactly to the foil geometry. An enlargement of this area is shown below in Figure 50.

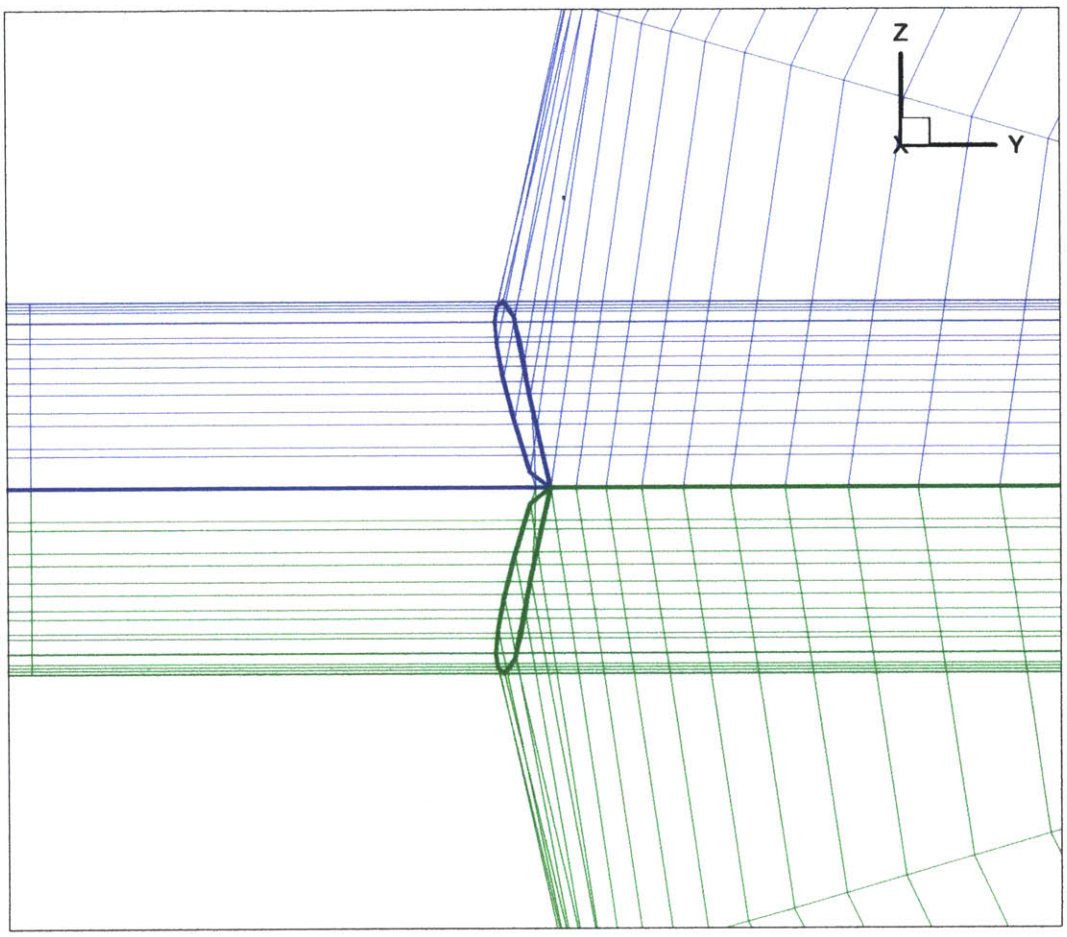

Figure 50

Leaving this more complex geometry for now, we will first concentrate on the simple geometry wherein the two forms merely butt up against each other.

As a means of judging the quality of the solutions converged upon, we first need to get a baseline figure for lift, sway force and drag. A typical approximation technique for a foil mounted on a body is to invoke the method of images and use an aspect ratio that is exactly double that of the actual geometry. We note here, however, that this approximation is exact only for a foil mounted on an infinite wall aligned parallel to the flow. Our bulb is clearly not infinite and the approximation will contain some error as a result.

To get a sense of the actual flow properties as compared to the case of the infinite wall scenario, it may be helpful to note that whereas the infinite case causes no perturbation in the velocity, the ellipsoid will clearly cause the flow to accelerate around it leading to higher fluid velocities than the ambient flow. This in turn will lead to a set of qualitative modifications of our expected results.

First, we expect the lift, as a function of the velocity, to be greater than that predicted by the infinite wall situation. Second, we expect the drag, also a function of fluid velocity, to be greater than that predicted as well. Finally, and most subjectively, we note that the presence of the foil on one side of the bulb only will cause asymmetry in the flow. The presence of the foil will cause additional fluid acceleration around it resulting in higher fluid velocities on the bulb side of the foil. This higher velocity will in turn cause a slight suction force on the bulb side.

While it could be argued that this suction force would be cancelled by the loss of the sectional area occupied by the foil, a counterargument would rely on the fact that the foil's sectional area is on the order of 200 times smaller than the sectional area of the bulb along the x-z plane. Therefore, while its effects will be felt over a large portion of the bulb's surface, the loss of its sectional area from that surface is nearly inconsequential. As a result, we expect to see a small, but negative force in the sway direction.

Referring to the Glauert and Hoerner equations (35) through (38) and (39) through (42) used to develop values for lift and drag, we can see that it is actually very convenient that we have halved the length of the foil. As a result, when we double the aspect ratio to account for the presence of the bulb, we regain our original foil. Therefore,

$$C_L' = \frac{1}{\frac{1}{1.8\pi} + \frac{1}{\pi AR} + \frac{1}{2\pi AR^2}} = 3.5484$$

and

$$L = \frac{1}{2}\rho U^2 A_p C_L' \alpha = 0.457N$$

using an angle of attack of 10 degrees a velocity of 0.5 m/s and our actual projected area rather than the doubled area used to determine the lift coefficient slope.

Moving to the Glauert equations for drag, we see

$$L = 2.618\alpha = C_L \rho A_p U^2 \Rightarrow C_L = 1.774\alpha$$

and therefore,

$$C_{Di} = 0.1875 C_L^2 = 0.590\alpha^2$$

and as a result,

$$D = C_{Di}\rho U^2 A_p = 0.871\alpha^2 = -0.0265N$$

for our ten degree angle of attack. The negative sign on the drag force is included to show that the force will act in a direction opposite to the body motion.

Unfortunately, no such simple estimate is possible for the sway force. Qualitatively, it can again be stated that the sway force is a suction force, and therefore a negative quantity. Also, I would not expect this force to be greater in magnitude than the drag force. So perhaps we can set reasonable limits for the sway force to be somewhere between zero and the predicted drag force.

RESULTS:

Two methods were used for the simple non-intersecting geometry. In the first, the panels were evenly distributed over the surface of the foil and bulb. In the second, the panels were distributed in such a way as to provide greater panel density toward the foil-bulb juncture This method is referred to as "dense" in the following plots. Results from both panelization schemes are reproduced below. Note that in preliminary runs, panel density was increased on the foil and bulb simultaneously, with a constant geometric relationship between the maximum panel size on each. Results were as follows for drag, sway and lift forces:

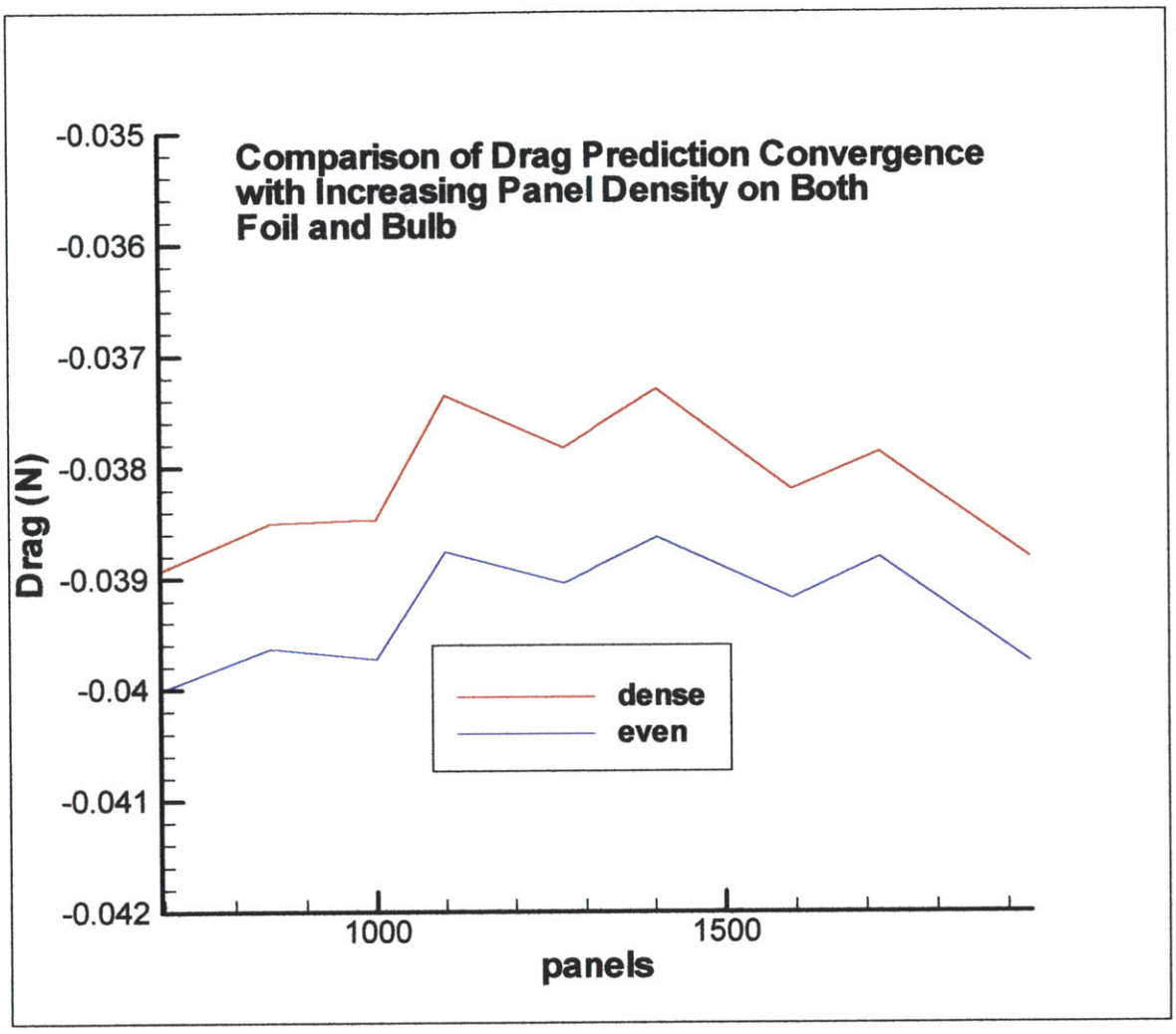
Comparison of Drag Prediction Convergence with Increasing Panel Density on Both Foil and Bulb
Drag (N)
-0.035
-0.036
-0.037
-0.038
-0.039
-0.04
-0.041
-0.042
1000
1500
panels
dense
even

Figure 51

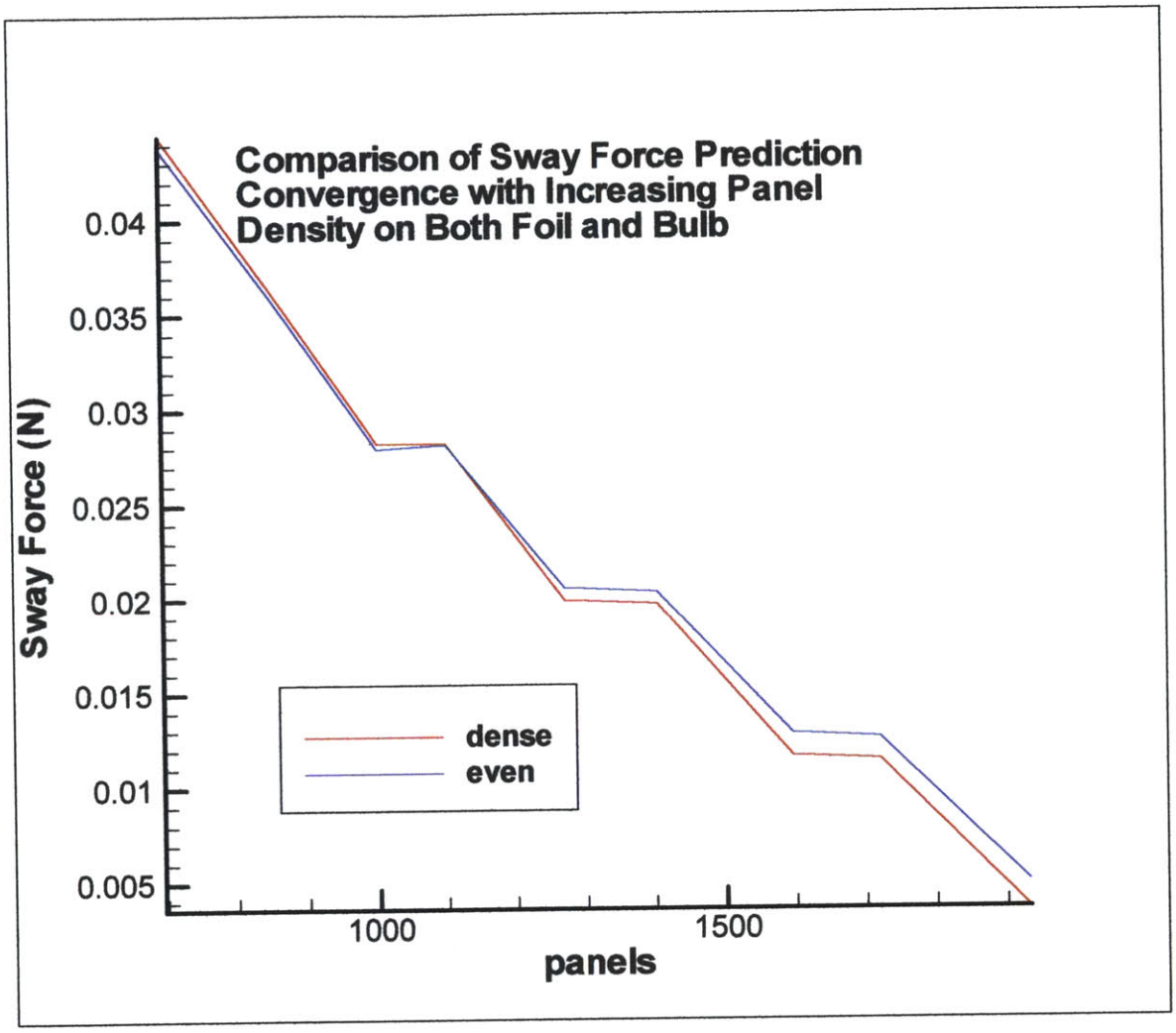
Comparison of Sway Force Prediction Convergence with Increasing Panel Density on Both Foil and Bulb
Sway Force (N)
0.04
0.035
0.03
0.025
0.02
0.015
0.01
0.005
1000
1500
panels
dense
even

Figure 52

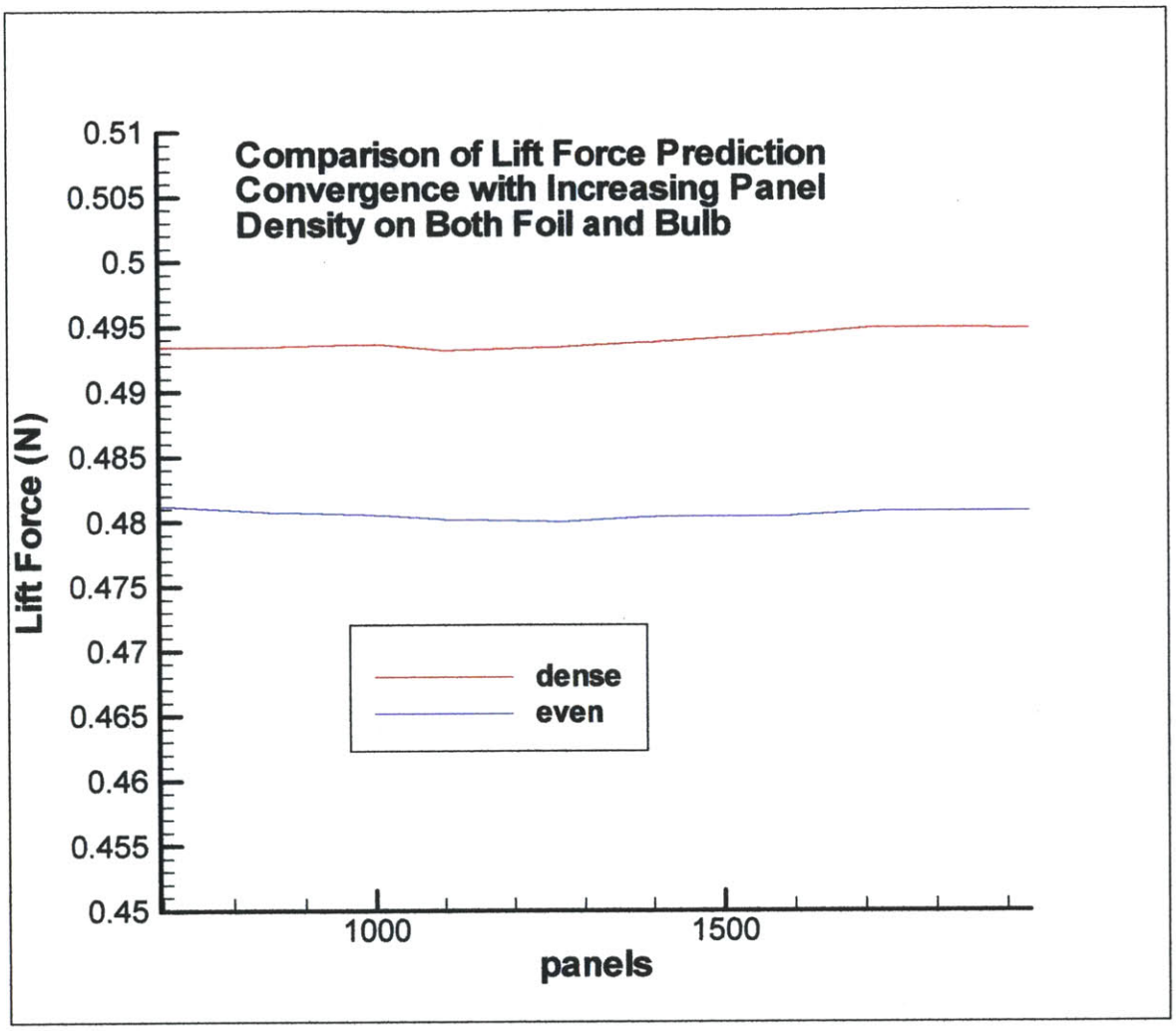

Figure 53

Clearly, the results above are inconclusive as to whether or not increasing panel density will lead to convergence. As a result, it was decided that the effects of increasing foil panel density and of increasing bulb panel density should be examined separately in order to ascertain the individual effects of each. This was done by keeping one panel density constant in the middle of its previous range, and varying the other density from a minimum to the maximum possible density allowed by panel quantity limits.

The first set of simulations used increasing foil panel density with constant bulb panel density. The results are shown below.

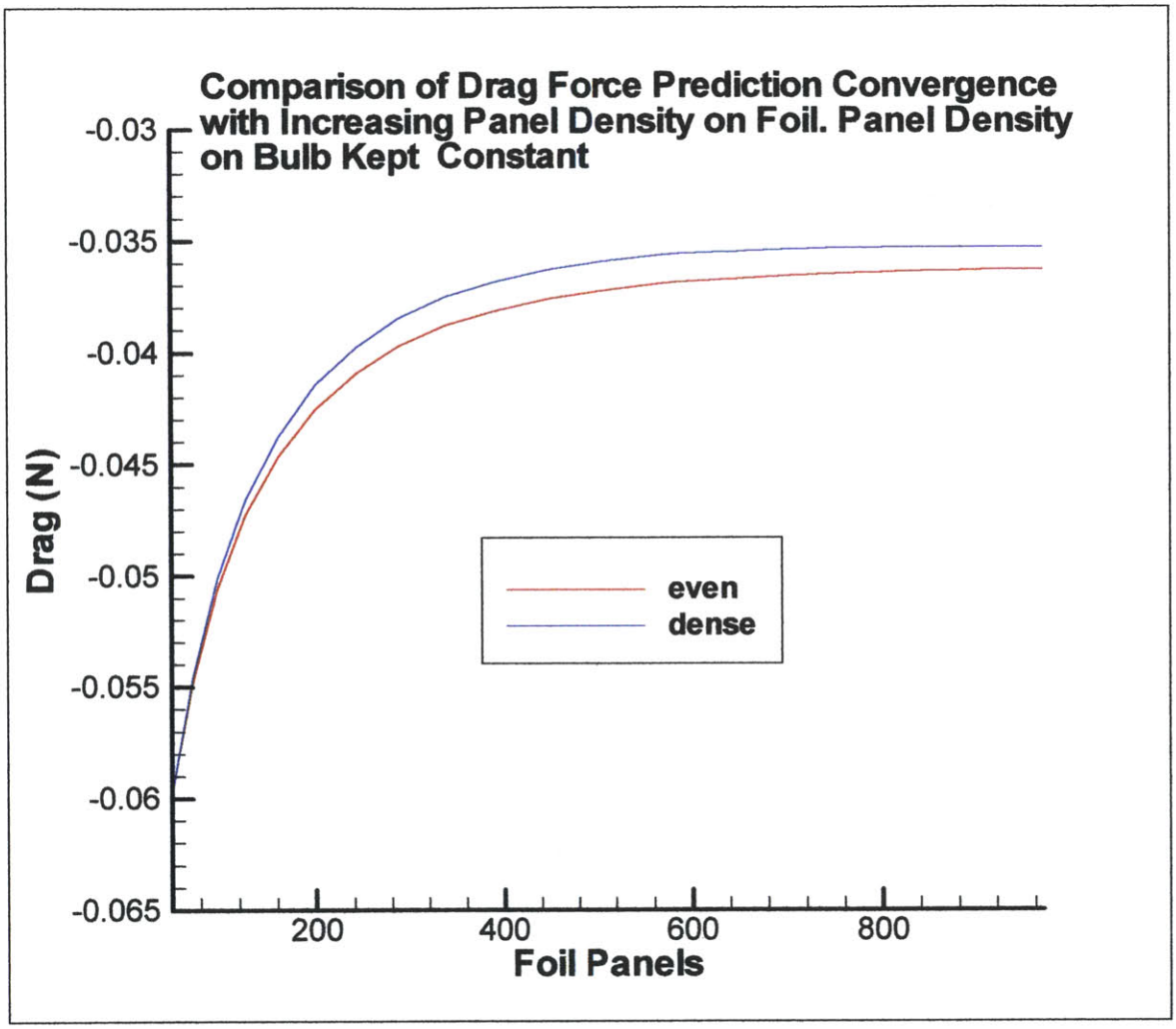
Comparison of Drag Force Prediction Convergence with Increasing Panel Density on Foil. Panel Density on Bulb Kept Constant
-0.03
-0.035
-0.04
-0.045
-0.05
-0.055
-0.06
-0.065
Drag (N)
200
400
600
800
Foil Panels
even
dense

Figure 54

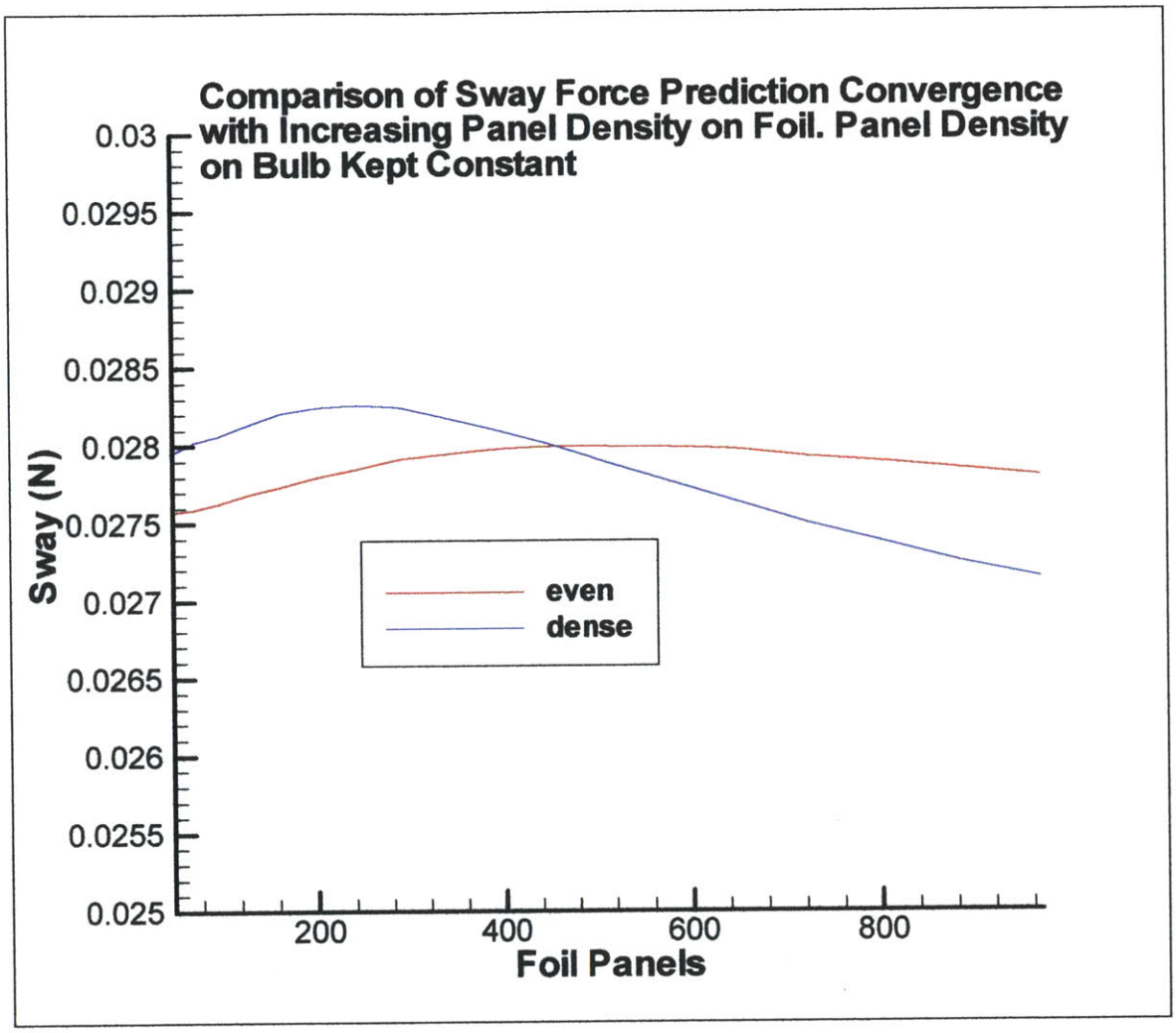
Comparison of Sway Force Prediction Convergence with Increasing Panel Density on Foil. Panel Density on Bulb Kept Constant
0.03
0.0295
0.029
0.0285
0.028
0.0275
0.027
0.0265
0.026
0.0255
0.025
Sway (N)
200
400
600
800
Foil Panels
even
dense

Figure 55

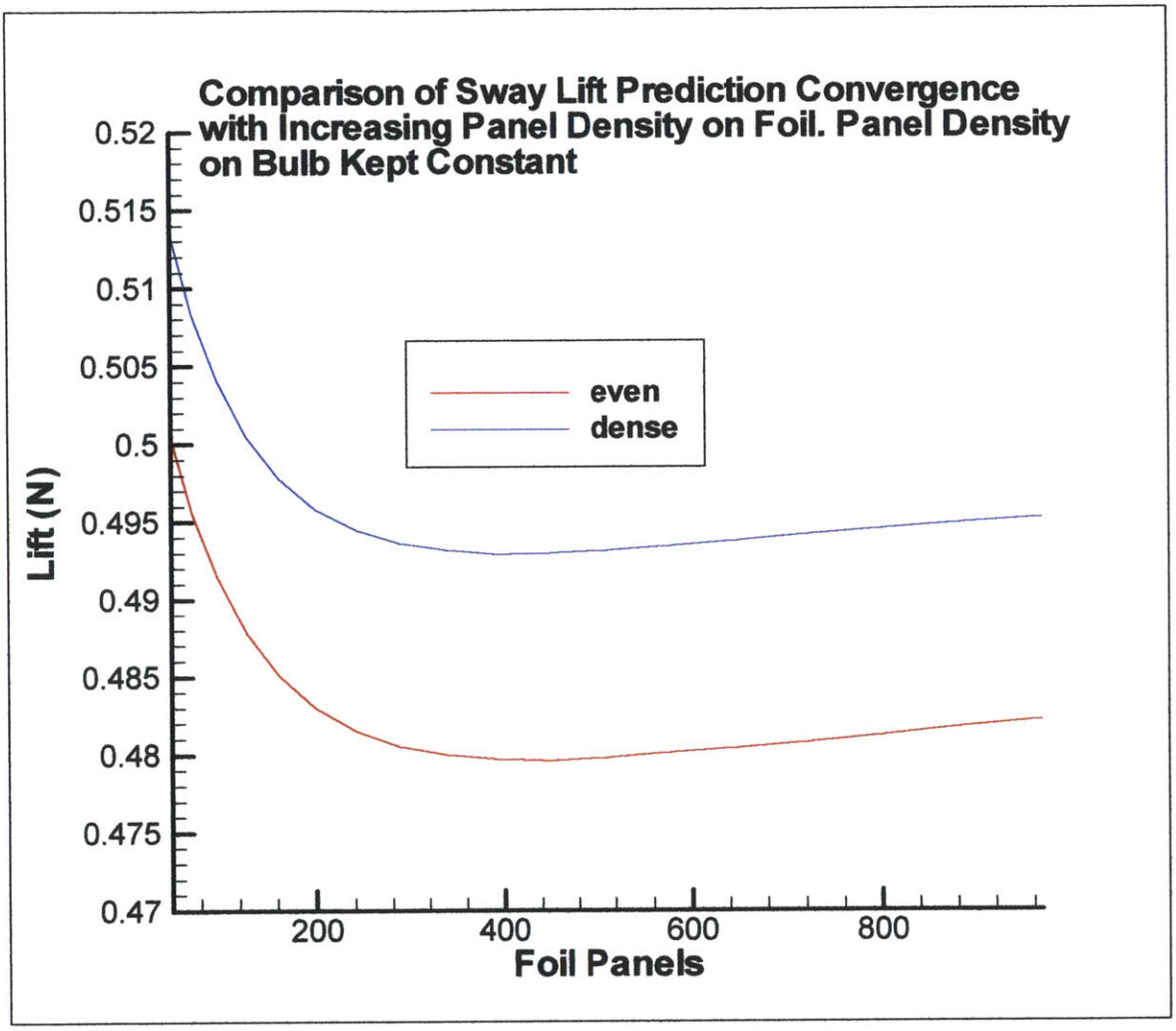

Figure 56

The results for the opposite situation, with constant foil density and variable bulb panel density are reproduced below:

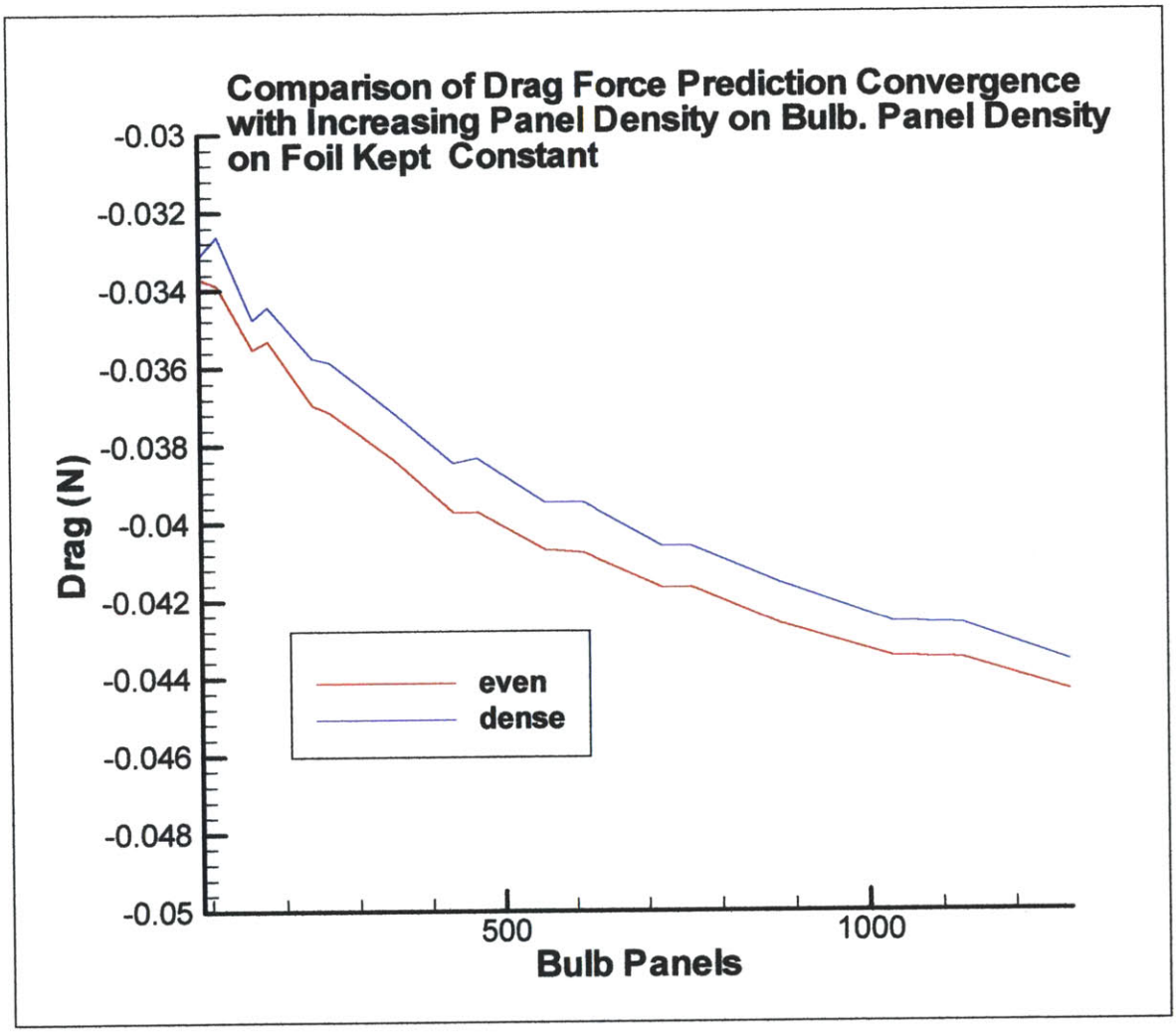
Comparison of Drag Force Prediction Convergence with Increasing Panel Density on Bulb. Panel Density on Foil Kept Constant
-0.03
-0.032
-0.034
-0.036
-0.038
-0.04
-0.042
-0.044
-0.046
-0.048
-0.05
Drag (N)
500
1000
Bulb Panels
even
dense

Figure 57

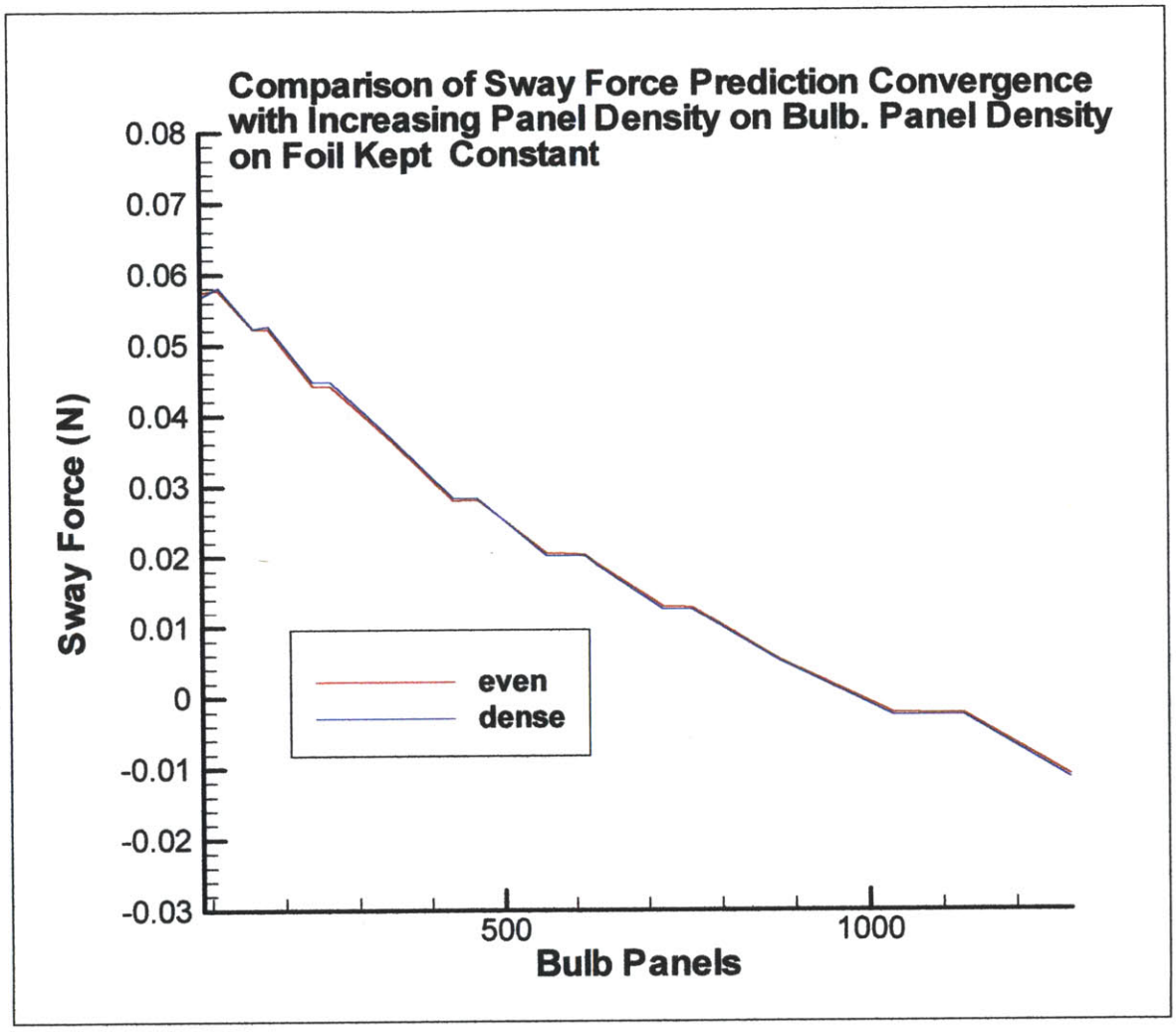
Comparison of Sway Force Prediction Convergence with Increasing Panel Density on Bulb. Panel Density on Foil Kept Constant
Sway Force (N)
0.08
0.07
0.06
0.05
0.04
0.03
0.02
0.01
0
-0.01
-0.02
-0.03
500
1000
Bulb Panels
even
dense

Figure 58

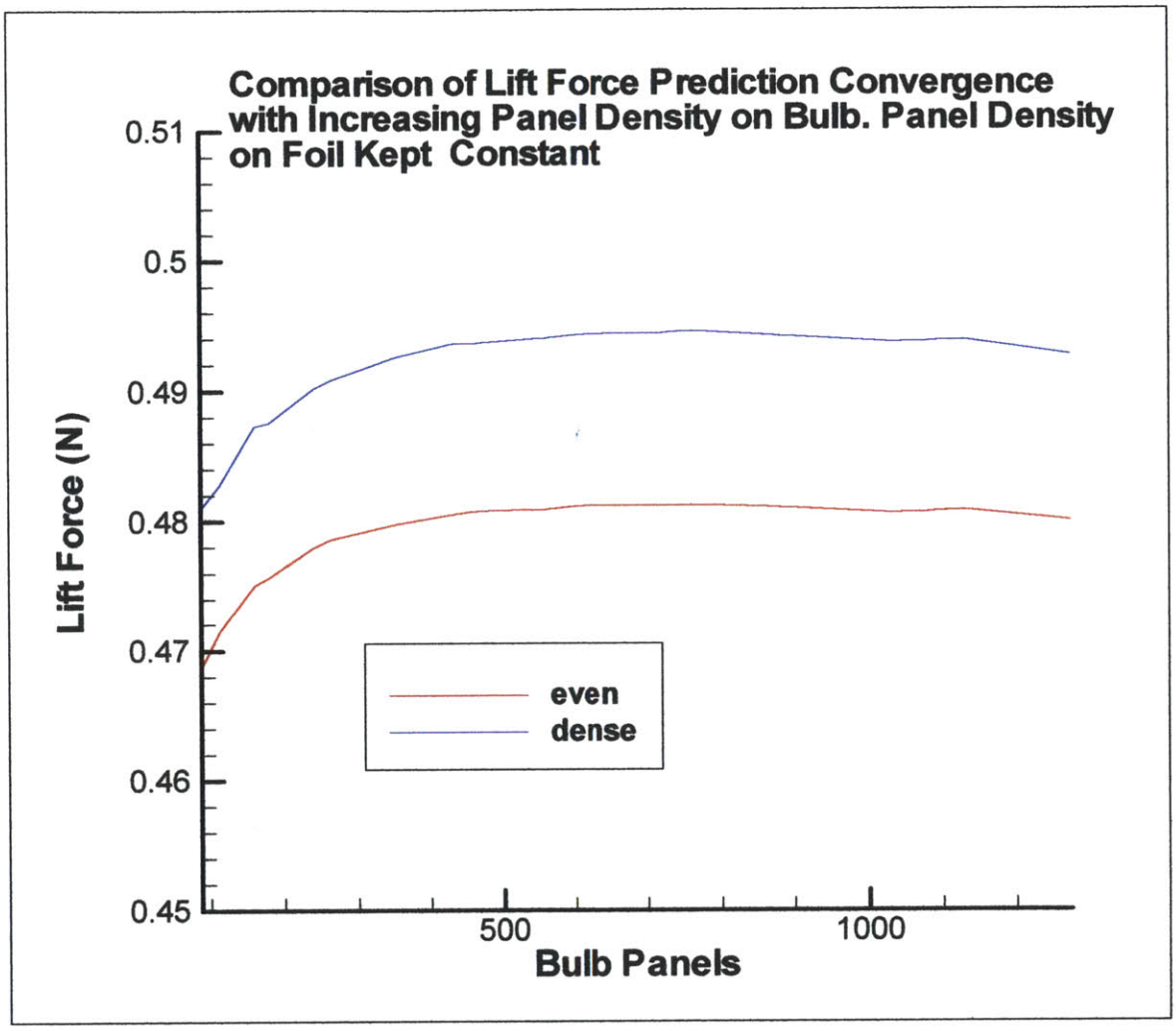

Figure 59

Taking an analysis of each force in turn, the first but perhaps most important observation from the drag plots is that they begin to explain the unconventional convergence plots seen previously wherein both foil and bulb panel density varied simultaneously. We note that we do, in fact, see convergence in both the foil varying and bulb varying cases but also note that the two cases show convergence from opposing directions. While the plot of foil panel density variation has drag converging from below, the plot of bulb panel density variation has drag converging from above. The result of this is that when both foil and bulb panel density vary simultaneously, the convergence errors tend to offset each other and the convergence is not readily apparent. This effect is magnified by the fact that increasing both foil and bulb density together reduces the maximum density allowed on each surface due to panel number limitations and therefore, convergence is even less evident.

The following table was produced in order to compare the effects of each method on convergence. The values entered show the absolute value of the maximum variation over the course of the convergence.

	Foil Variation	Bulb Variation
Even Panel Drag Variation	$2.343*10^{-2}$	$1.066*10^{-2}$
Dense Panel Drag Variation	$2.450*10^{-2}$	$1.046*10^{-2}$

We see from this table that increasing the foil density is more than twice as effective as increasing the bulb density when it comes to speeding up the convergence of the drag force result. This is not surprising in that it is the foil that generates the drag and therefore one would expect its mesh density to have a greater effect on the solution convergence.

It should be noted that in the preceding simulations the two solutions converged upon are not the same. This may be due to the fact that while the density of one portion of the body is increasing towards an optimal value, the density of the other remains unchanged. While this is helpful to show that the independent solutions will converge, the fact remains that each independent solution is still held back from some optimal single value by the remaining, less than optimally meshed portion of the body.

Another observation from the drag results is that it seems as if the dense panel meshing scheme results in faster convergence than the even scheme. It also should be noted that both converged results ($-3.628*10^{-2}$ and $-4.436*10^{-2}$) are reasonably close to our baseline value of $-2.65*10^{-2}$ as well as being greater in magnitude, as predicted.

Turning now to the sway force, one can see that increasing either foil or bulb panel density seems to result in convergence toward a solution from above. Progress towards this solution convergence is extremely slow, however, particularly in the foil variation case and the plot indicates that it will take a great number of panels to finally achieve.

The most significant conclusion, illustrated by the table of the sway force variation over the range of the convergence seen below, is that bulb panel density utterly dominates foil panel density in its effects on sway force solution convergence.

	Foil Variation	Bulb Variation
Even Panel Sway Variation	$4.165*10^{-4}$	$6.875*10^{-2}$
Dense Panel Sway Variation	$1.116*10^{-3}$	$6.818*10^{-2}$

Note that the variation due to bulb panel density is approximately two orders of magnitude greater than that produced by foil panel density variation. This result should come as no surprise to us. The foil meshing should have little to no effect on the solution due to the fact that its surface is oriented parallel to the force in question.

A final observation on the sway force is to note that it does seem to be converging on a solution that is supported by our baseline range, somewhere between 0 and the drag

force. Most importantly, it is certainly a negative value, one that is qualitatively justifiable from theory.

Finally we turn to lift and note again that both foil and bulb panel variation seem to lead towards convergence. While it is more typical, in my experience, to see a monotonic, asymptotic approach towards convergence, the plot of foil panel density effects still shows both values approaching convergence after some overshoot. This is demonstrated by the negative second derivatives displayed by the slightly "concave-down" geometry of the plot lines as they head towards the maximum limit of . Similar to the drag force convergence, we again see convergence from opposite sides of the convergent value, a behavior that obscures the convergence because low panel density values tend to cancel each other out.

In order to assess the relative importance of the meshing of each portion of the body on lift results, the same type of table was constructed showing the total variation of the lift force over the range of convergence.

	Foil Variation	Bulb Variation
Even Panel Lift Variation	$2.095*10^{-2}$	$1.270*10^{-2}$
Dense Panel Lift Variation	$2.071*10^{-2}$	$1.357*10^{-2}$

Here we see that, similar to the drag results, the lift convergence is almost twice as sensitive to the variation in the foil than it is to variation in the bulb. Again, this comes as no surprise due to the geometry in question.

Checking our baseline value of $4.570*10^{-1}$, we can see that the results produced by SWAN are reasonable. They are very close to the baseline value, but slightly greater, as predicted previously.

One remaining source of concern, however, is the large separation between the even and dense panelization lines for lift, a separation that does not seem to grow smaller as they head towards convergence. Obviously the cause is the different meshing techniques as all other aspects of the flow are identical. This raises the point of consistency between simulations for the purposes of comparisons. The only way any valid comparisons can be made between different forms is to maintain nearly identical meshing schemes. While both the dense and even panel distributions seem to show convergence, it is evident that the indicated solutions will not be the same. The best strategy then, is to opt for a meshing scheme and stick to it throughout the simulations.

We now return to the more complex geometry discussed previously, in which the foil shape is allowed to pass into the bulb. Drawing on experience gained above, it was decided to do convergence testing prior to any other simulations. Additionally, only the even meshing was employed. If that meshing proves successful, then the dense meshing can be examined as well.

The same simulations were done, with angle of attack, velocity and all other geometry remaining unchanged. Variation was again allowed first only on the foil and subsequently only on the bulb. The drag, sway and lift results for the foil variations are reproduced below.

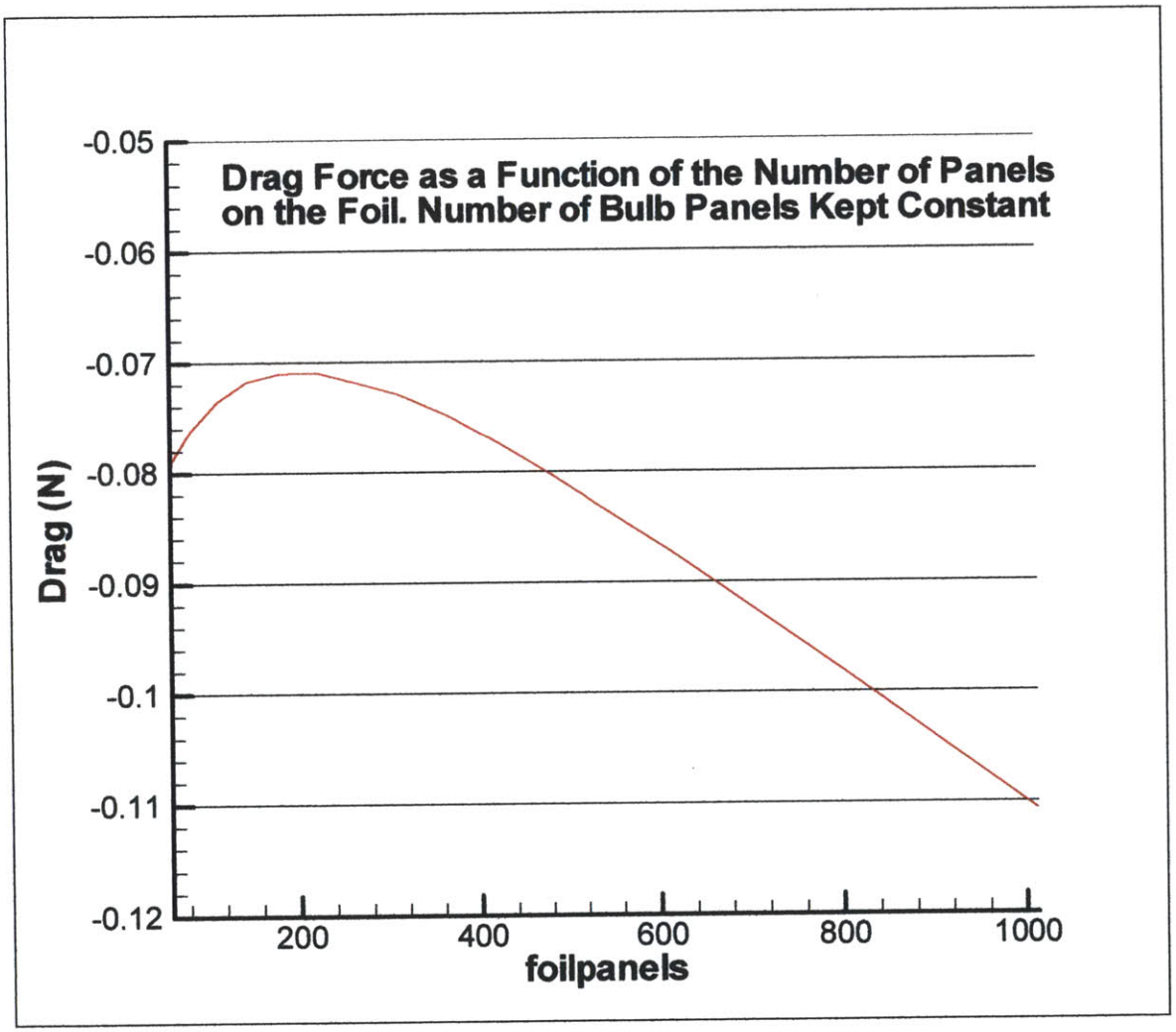

Figure 60

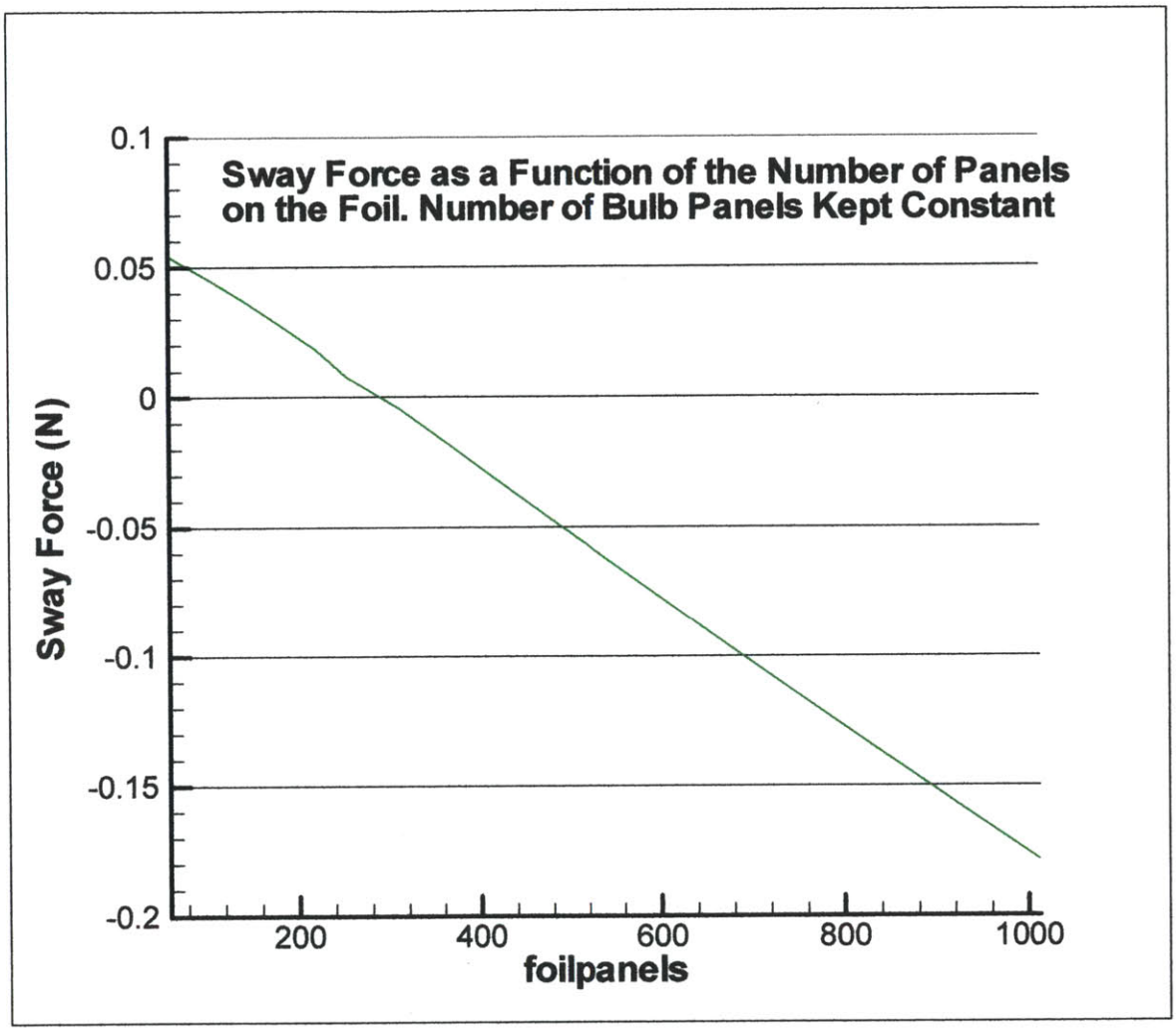
Sway Force as a Function of the Number of Panels on the Foil. Number of Bulb Panels Kept Constant
Sway Force (N)
0.1
0.05
0
-0.05
-0.1
-0.15
-0.2
200
400
600
800
1000
foilpanels

Figure 61

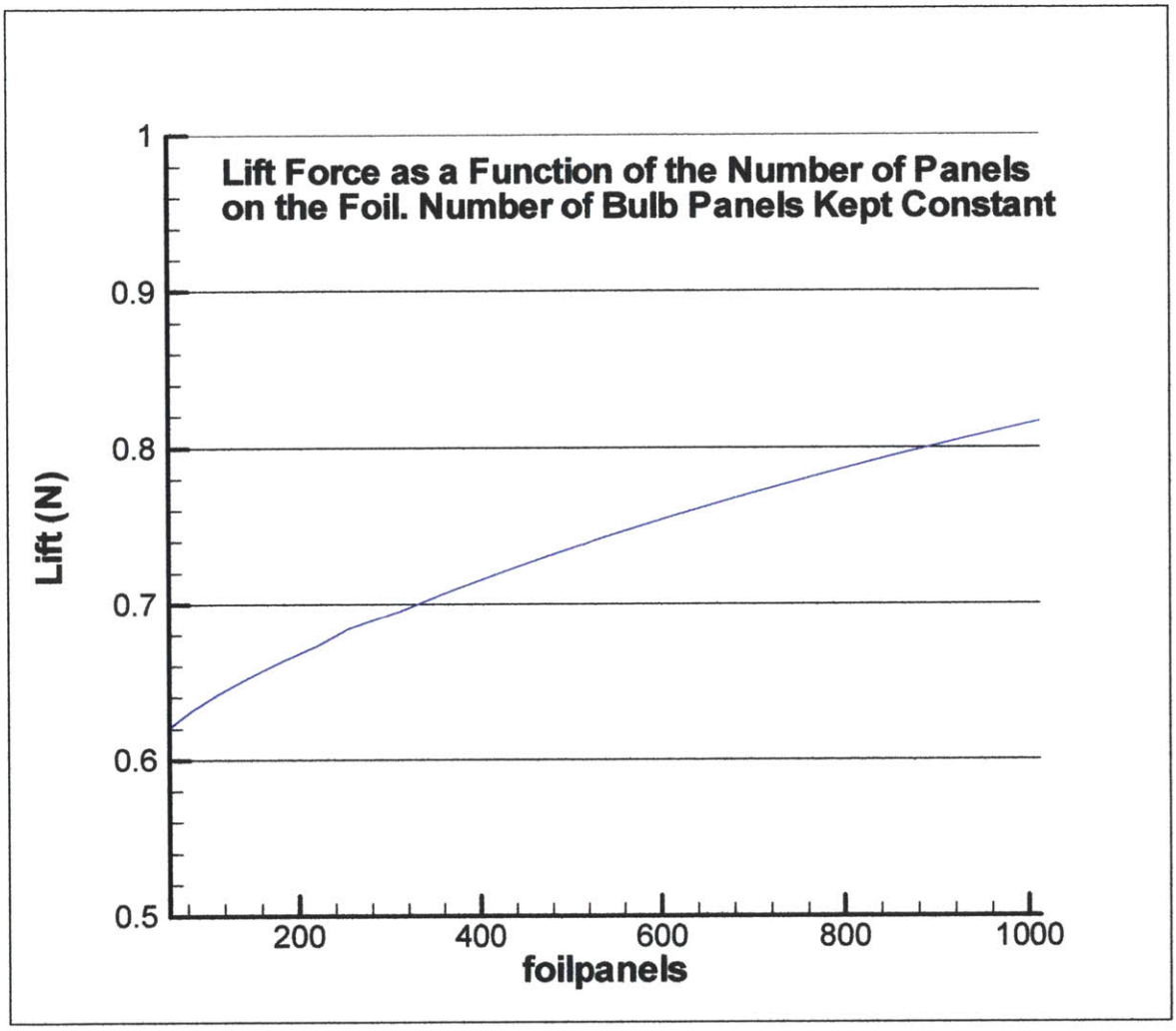

Figure 62

Clearly, none of these plots looks too promising from a convergence point of view. Nonetheless, the series with bulb panel density variation was run with the following results for drag, sway and lift.

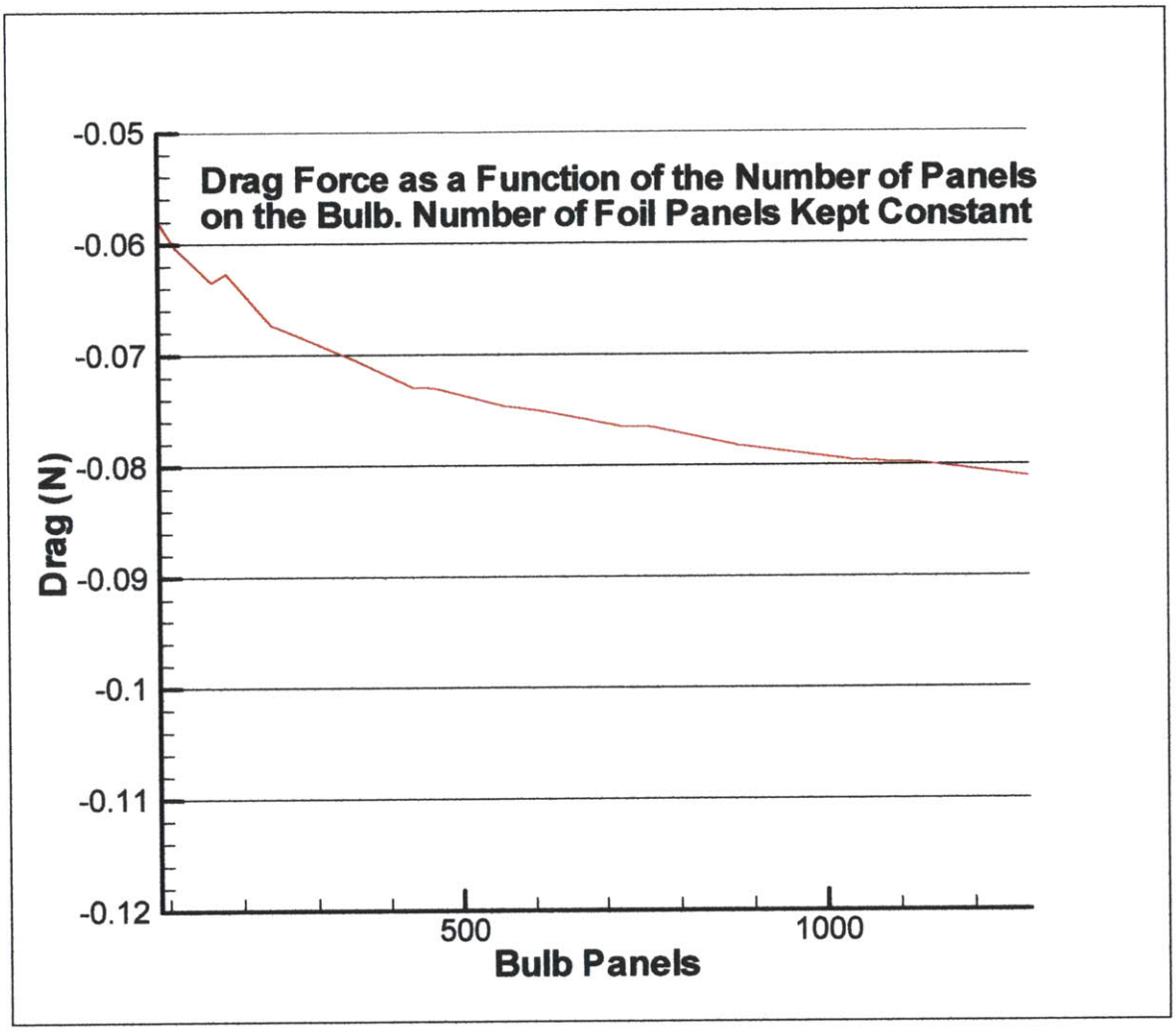
Drag Force as a Function of the Number of Panels on the Bulb. Number of Foil Panels Kept Constant
-0.05
-0.06
-0.07
-0.08
-0.09
-0.1
-0.11
-0.12
Drag (N)
500
1000
Bulb Panels

Figure 63

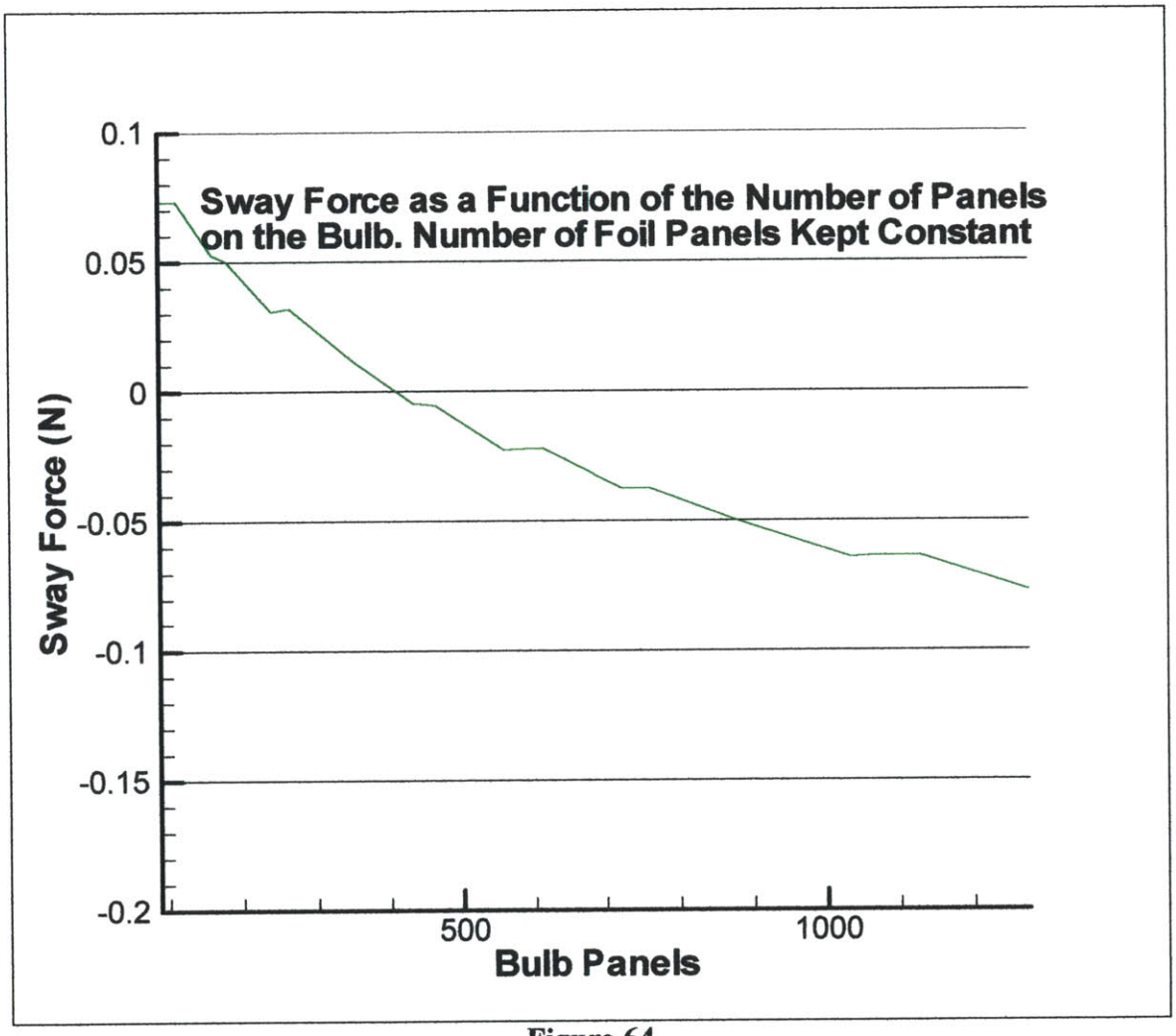
Sway Force as a Function of the Number of Panels on the Bulb. Number of Foil Panels Kept Constant
Sway Force (N)
0.1
0.05
0
-0.05
-0.1
-0.15
-0.2
500
1000
Bulb Panels

Figure 64

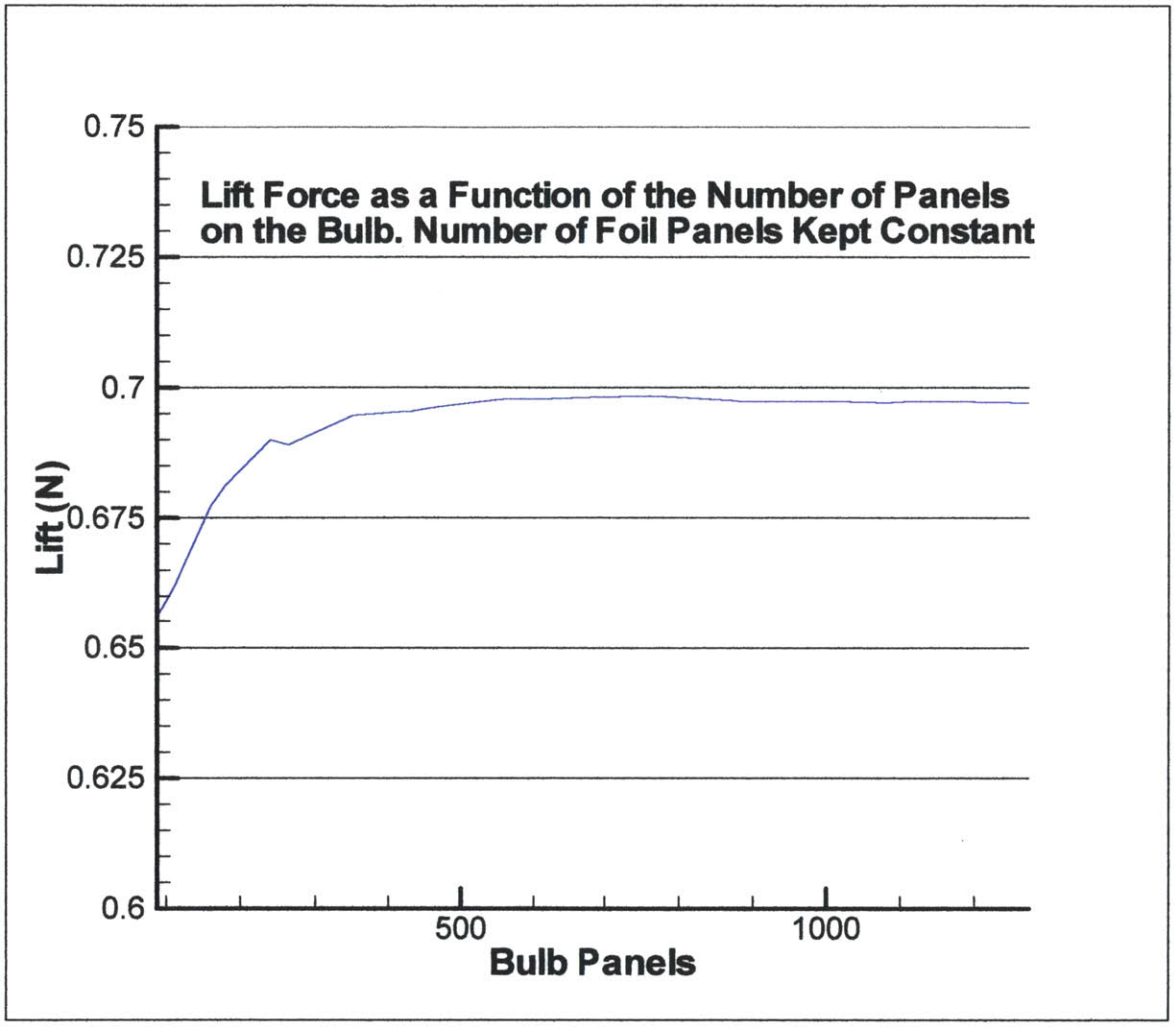

Figure 65

While it can be seen that we do have convergence in the simulations of increasing bulb panel density above, it should be noted that the value being converged upon is nearly equal to the one provided by the foil convergence test for the now constant foil panel density. Looking at the convergence tests for foil panel density variation, it can be seen that we do not have convergence in either the drag or sway forces. Drag seems to be some negative exponential function of panel quantity heading towards negative infinity at the limit, and sway seems to be a linear function of panel quantity, also headed towards negative infinity at the limit of infinite panel numbers.

While these two failures alone are enough to disqualify this scheme, a look at the lift force increases the suspicion that bad values are being produced. While the argument could be made that this lift plot will converge at some very large number of panels, the value being converged upon in this case is much larger than our baseline prediction. For this reason, the more complex geometry with foil extending within the bulb is disqualified as a viable solution scenario.

The final step of this analysis was to return to the successfully modeled simpler geometry and run this form through a range of angles of attack to ascertain the effects on the SWAN results.

The meshing scheme chosen for the following simulations implemented the dense panel meshing scheme. On the foil there were 18 panels along the both chord and span dimensions. The panels were arrayed in a cosine distribution from the leading to trailing edges, and in an exponential distribution from the foil tip to the bulb.

The bulb also employs greater panel density towards the bulb-foil juncture and has 16 panels circumferentially and 27 panels longitudinally. Additionally, a wake sheet was employed that extended to a point approximately 30 chord lengths behind the foil trailing edge. The geometry is as seen below in Figure 66.

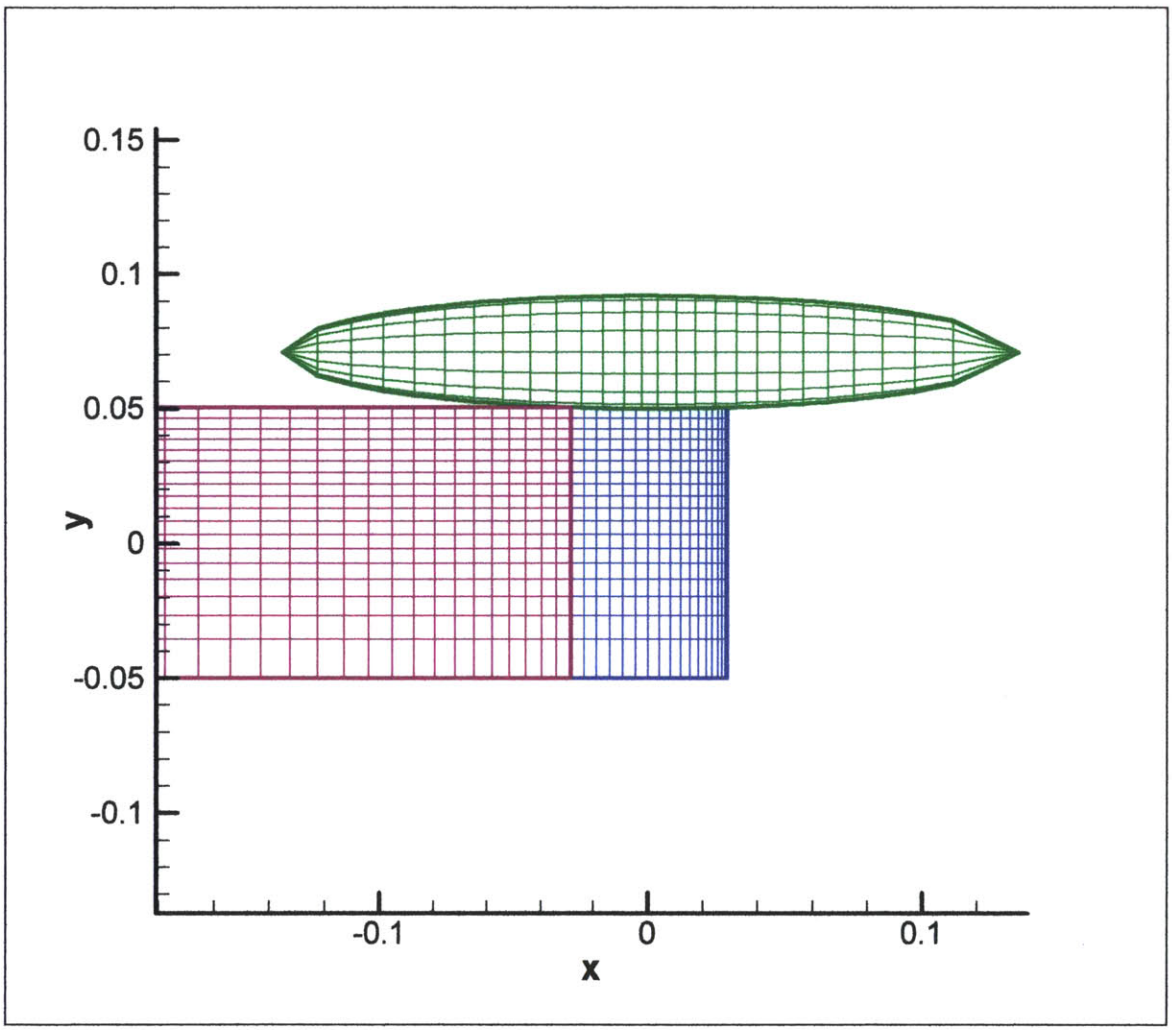

Figure 66

This form was run at 0.5 m/s at a depth of 2m and angles of attack ranging from 0 to 26 degrees.

We first note that previous simulations show that convergence cannot be attained for the sway force with the number of panels available. Therefore, this geometry was chosen with an aim towards maximizing the accuracy of the lift and drag results.

The following two figures show these lift and drag results. Three lines are present on the plots. One shows the actual SWAN results. A second shows theoretical results based on the doubled aspect ratio theory. Finally, a third begins with the SWAN results from the ten degree angle of attack. Assuming that this value is a function of the angle of attack in the lift case and of the angle of attack squared in the drag case, we then derive the SWAN indicated functions for lift and over the complete range of angles of attack. This third, adjusted theory lines then show us how well SWAN's results conform to the theoretical mathematical forms of the lift and drag formulas.

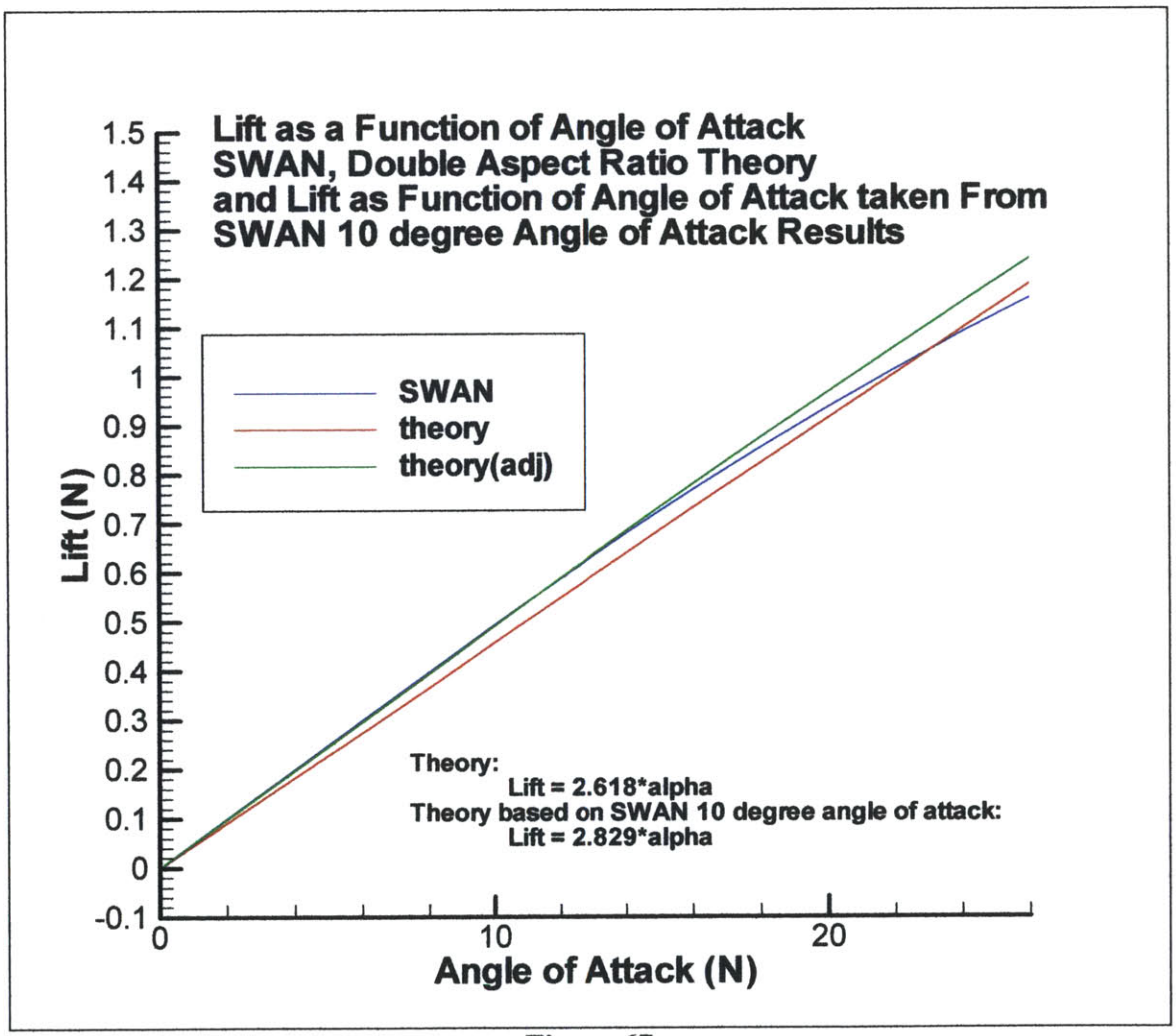

Figure 67

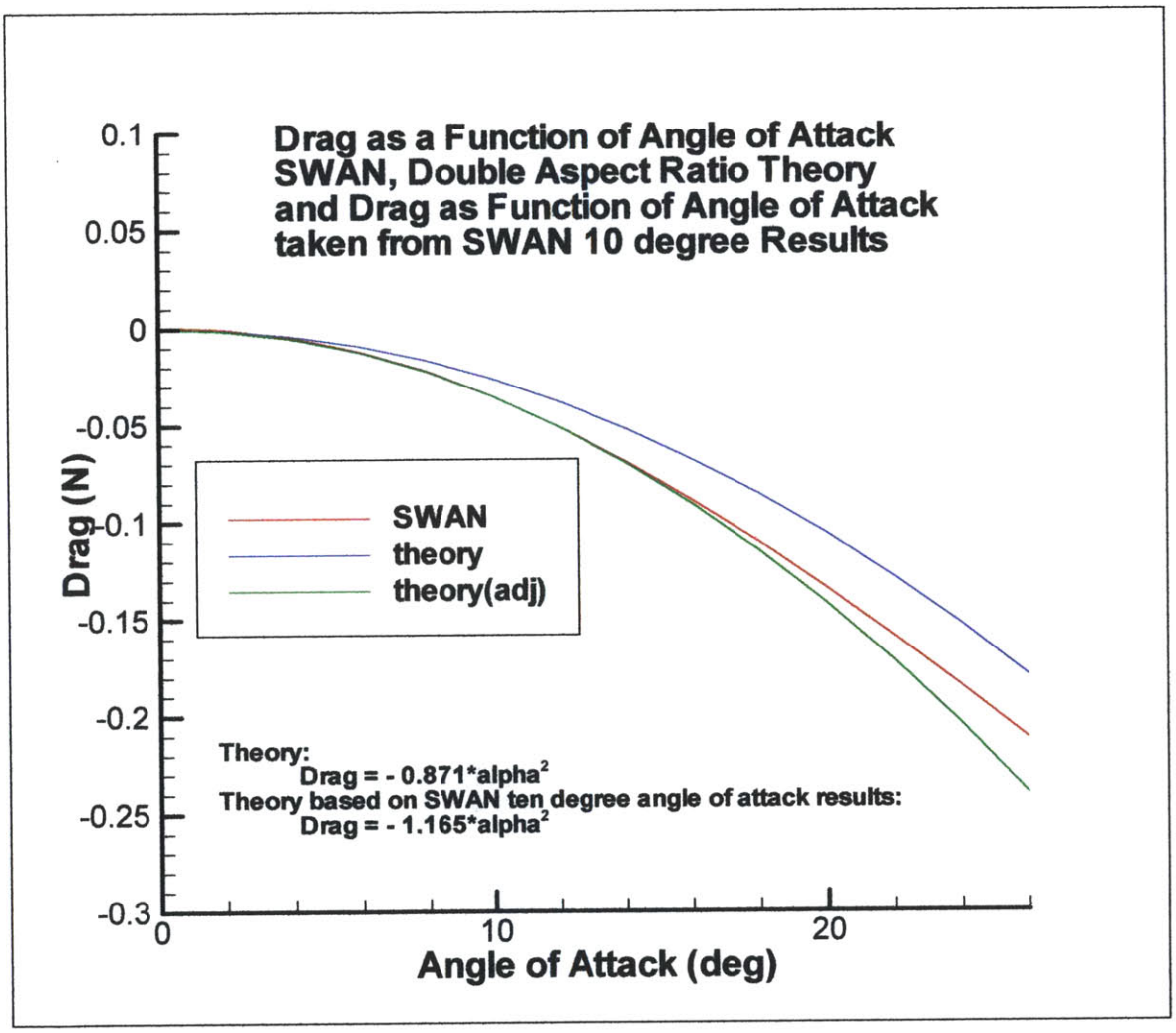

Figure 68

For the lift case, we can see that SWAN and theory agree fairly well. Additionally, we note that within the restrictions of small angle approximation, the SWAN results are greater that those predicted by theory, which supports their accuracy for reasons detailed above. Finally, we see that the SWAN results conform very well to the adjusted theory which checks how they compare with the simple function of angle of attack described above.

For the drag case, we can see that SWAN again produces results that are close to theory, Again, these results are greater in magnitude than those predicted which supports their accuracy. Finally, we again see good conformity of the SWAN results to the simple function of the angle of attack squared developed from the ten degree results.

A final, interesting aspect of these simulations is the SWAN produced sway force results. Reemphasizing the point that the above simulations were run with a meshing scheme intended to increase lift and drag accuracy at the expense of sway accuracy, I include the following plot of sway force as a function of angle of attack.

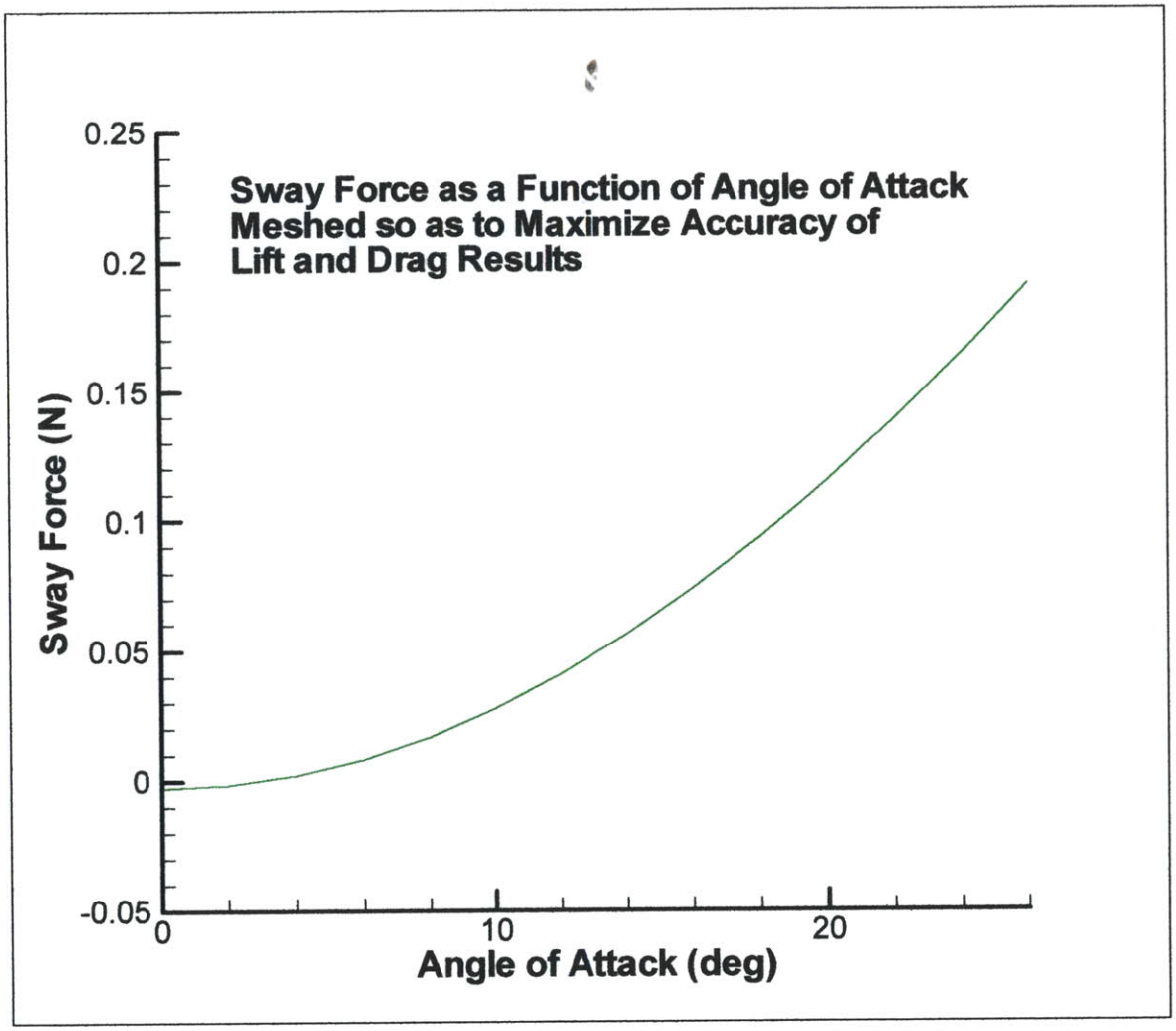

Figure 69

Clearly, this plot runs counter to the expected results. As stated above, we expect to see a slightly negative (suction) force on the order of the drag force with magnitude increasing with angle of attack. The fact that the sway force began only slightly negative at low angles of attack and then increased, raised doubt as to the validity of the preliminary reasoning that produced the expected range for the results.

In order to settle this issue, a series of simulations was done using the same geometry but with maximum panel density on the bulb in an attempt to better model the sway force. It should be noted that maximum bulb panel density resulted in what appeared to be a result

that converged on a negative value as expected. So, using this meshing should result in a better approximation. The following plot was produced.

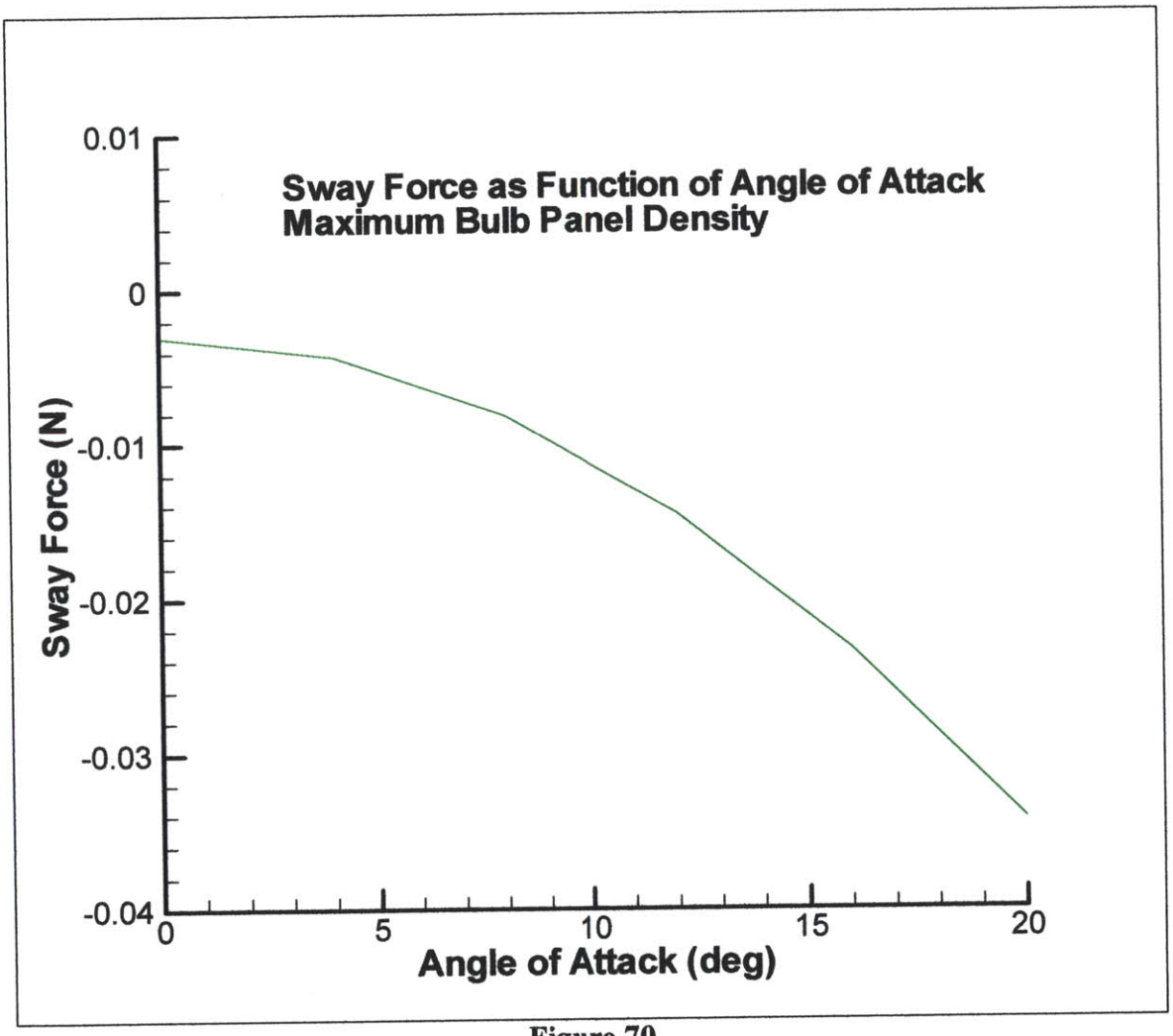

Figure 70

Clearly, this result fits better with previously described expectations. This serves as a sort of mutual confirmation of both the validity of the assumptions underlying the expected results as well as of the fact that increasing bulb panel density will eventually lead to convergence. The above results should only be taken on a qualitative level, however, due to the fact that even at maximum panel density, convergence was not fully achieved.

A final interesting study was done as to the effects of increasing the distance between the foil and the bulb. Some concern was expressed that the solution might become unstable at small distances. In response, the foil was moved incrementally, 0.5, 1, 2, 4 ,8, 16, and 32 panel widths away from the bulb. Theoretically, we should regain the results for the foil alone as the distance increases. This is due to the fact that the bulb contributes no lift or

drag of its own in the absence of the foil. Returning to the Hoerner and Glauert equations (35) through (42) above we calculate the theoretical lift and drag of the foil alone to be

$L = 0.31675N$
$D = -0.020455N$

Further, we run SWAN simulations on the foil alone and get the following results:

$L = 0.304933N$
$D = -0.020668N$

The following two plots show the results of these simulations.

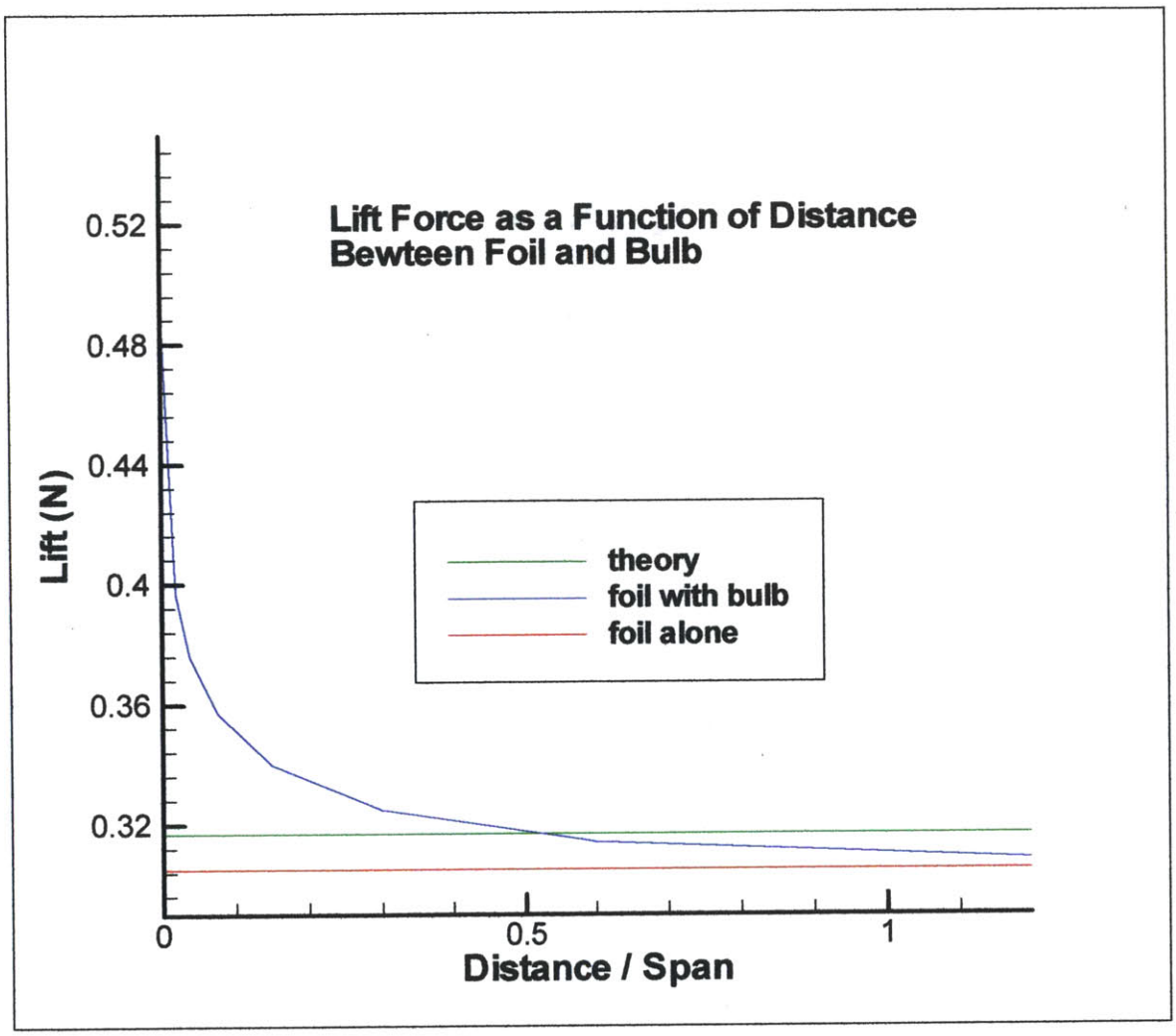

Figure 71

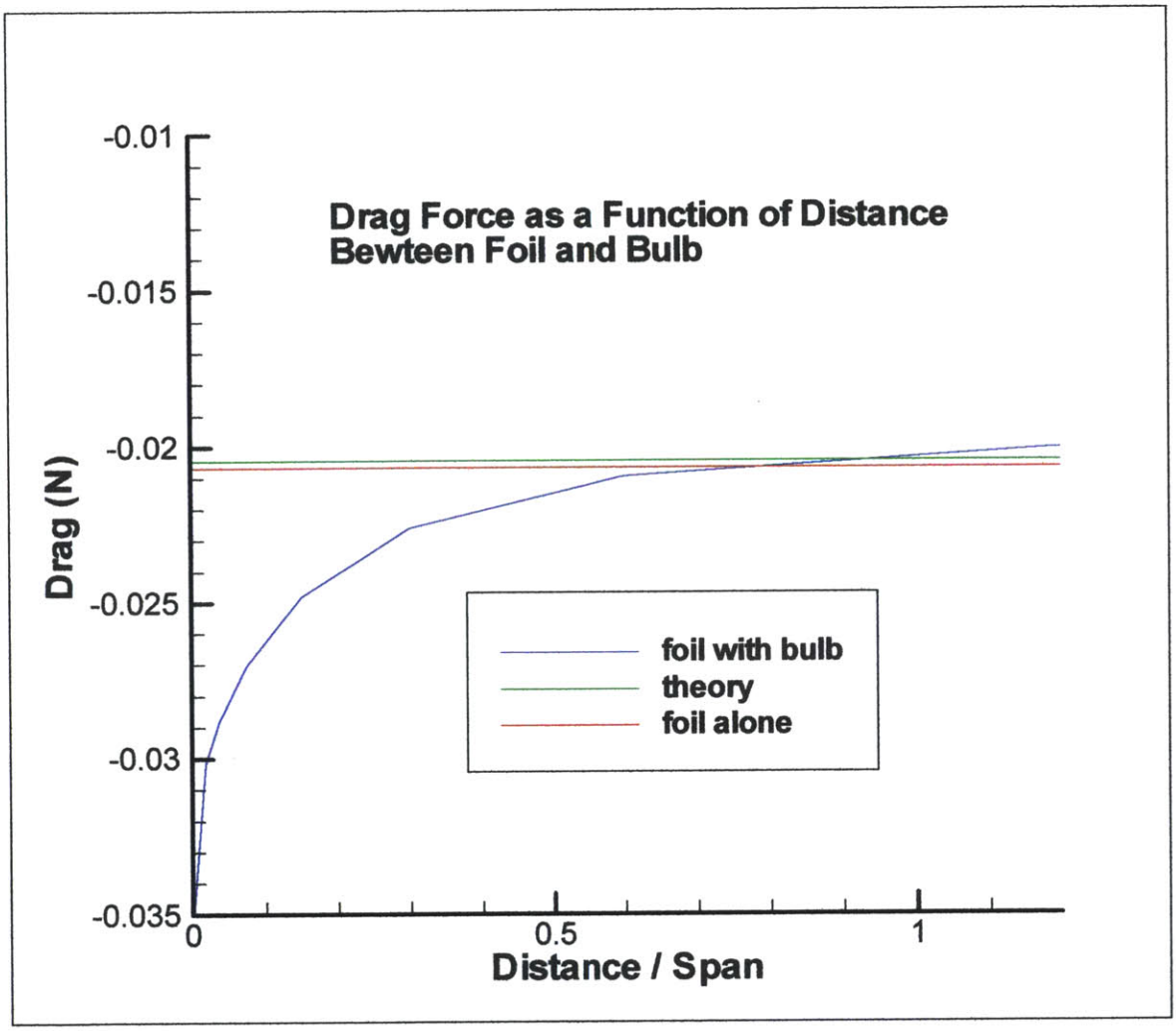

Figure 72

One can see from the above plots that both lift and drag tend toward the theoretical and foil alone results. There is overshoot in both cases, however, the reason for which is unclear.

Conclusions from this preliminary attempt to model the flow around composite forms are that gains can be made towards more rapid convergence for lift and drag by using a panel density on the foil that increases with proximity to the bulb. Additionally, it was found that extending the foil into the bulb greatly reduced the quality of the results and that merely butting the two forms against each other provided better output. Finally, it was noted that sway force convergence will only occur at very large numbers of bulb panels but that we should expect a suction force on the order of the drag force but slightly smaller in magnitude to be the eventual result.

CONCLUSIONS

The preceding study tested the three-dimensional Rankine panel method analysis routine SWAN for accuracy. Specifically, SWAN was tested on fully submerged lifting and non-lifting surfaces. Throughout the study, SWAN revealed itself to be an extremely valuable tool for the naval architect, producing several quantities of interest with a high degree of accuracy.

Convergence tests on a variety of simple forms, including a sphere, a spheroid, a symmetric foil, and an asymmetric, cambered foil showed rapid convergence to theoretically accurate values. In addition, SWAN's analysis of composite forms produced values which qualitatively, and quantitatively whenever possible, produced accurate results. The limit to the accuracy of the results, as is always the case with panel method solutions, was directly related to the number of available panels.

To conclude, in the field of naval architecture, advances in computer science will only continue to bring corresponding advances in the available accuracy and speed of routines such as SWAN. While it is clear this tool should not be used exclusively, panel method analysis can and should be used in conjunction with traditional tank testing to obtain the broadest possible understanding of the structure in question.

BIBLIOGRAPHY

[1] Glauert, H., *The Elements of Aerofoil and Airscrew Theory*, Macmillen Company, New York, 1943

[2] Hoerner, S.F., *Fluid Dynamic Drag*, Published by the author, Midland Park New Jersey, 1965

[3] Hoerner, S.F. and Boerst, H.V., *Fluid Dynamic Lift*, Published Liselotte Hoerner, Vancouver, Wa., 1985

[4] Kochin, N.E. et al, *Theoretical Hydromechanics*, Interscience Publishers, New York, 1964

[5] Kring, David C., *Time Domain Ship Motions by a Three-Dimensional Rankine Panel Method*, PhD Thesis, MIT, Cambridge, Ma., 1988

[6] Moran, J, *An Introduction to Theoretical an Computational Aerodynamics*, John Wiley and Sons, New York, 1984

[7] Nakos, D.E., *Ship Wave Patterns and Wave Patterns by a Three-Dimensional Rankine Panel Method*, PhD Thesis, MIT, Cambridge, Ma, 1990

[8] Newman, J.N., *Marine Hydrodynamics*, MIT Press, Cambridge, Ma., 1977